

INSTITUT FÜR IONENSTRAHLPHYSIK UND MATERIALFORSCHUNG
FORSCHUNGSZENTRUM DRESDEN-ROSSENDORF eV.

Growth, structure and magnetic properties of magnetron sputtered FePt thin films

Dissertation

zur Erlangung des akademischen Grades

Doctor rerum naturalium (Dr. rer. nat.)

vorgelegt der Fakultät Mathematik und Naturwissenschaften

der Technischen Universität Dresden

von

Dipl. Phys. Valentina Cantelli

geboren am 25.02.1970 in Asti, Italien

Eingereicht am 22. Februar 2010

1. Gutachter: Prof. Dr. W. Möller

2. Gutachter: Prof. Dr. D. C. Meyer

Verteidigt am 15. März 2010

Table of contents

Abstract	I
Symbols	III
Abbreviations	V
Motivation	1
1. Iron Platinum	5
1.1. The FePt <i>AI</i> and <i>LI₀</i> phases	5
1.2. The <i>AI</i> to <i>LI₀</i> phase transformation in FePt	7
1.3. Generation of the (001) preferential orientation in FePt <i>LI₀</i> layers	10
1.4. Nanoclusters formation	11
2. The deposition process	13
2.1. Basic plasma notions	13
2.2. DC glow discharges	15
2.3. Sputtering	18
2.4. Energy flux during magnetron sputtering deposition onto the substrate	20
2.5. Effects of deposition parameters on layer properties	22
3. Experimental set-up	25
3.1. The magnetron deposition chamber	25
3.2. The magnetron deposition chamber used for <i>in-situ</i> investigations at ROBL	27
3.3. Annealing processes	28
3.3.1. <i>Ex-situ</i> vacuum annealing chamber at FZD	28
3.3.2. <i>In-situ</i> vacuum annealing chamber at ROBL	28
3.3.3. Rapid thermal annealing (RTA) at FZD in Ar flow	29
4. Methods of investigation	31
4.1. X-ray scattering	31
4.2. X-ray scattering geometries	34

4.2.1.	X-ray reflectivity, absorption and diffuse scattering.....	37
4.2.2.	X-ray diffraction.....	42
4.2.3.	Grazing Incidence Small Angle X-ray Scattering (GISAXS)	44
4.2.4.	X-ray scattering: experimental set-up	46
4.3.	Additional methods of analysis	48
4.3.1.	Rutherford backscattering spectroscopy (RBS).....	48
4.3.2.	Scanning Electron Microscopy (SEM).....	50
4.3.3.	Transmission Electron Microscopy (TEM).....	51
4.3.4.	Superconductive Quantum Interference Device	52
5.	Investigation of the $A1$ - $L10$ phase transition	53
5.1.	Experimental parameters	53
5.2.	Results	54
5.3.	Discussion	57
5.4.	Summary	63
6.	Preferred c -axis orientation in thin FePt films	65
6.1.	Growths on crystalline substrate	65
6.1.1.	Experimental parameters	65
6.1.2.	Results	66
6.1.3.	Discussion.....	72
6.2.	Growths on amorphous substrate	74
6.2.1.	Experimental parameters	74
6.2.2.	Results	75
6.2.2.1.	As deposited layers	75
6.2.2.2.	RTA at 550°C in Ar flow	78
6.2.2.3.	Annealing at 700°C in vacuum	83
6.2.2.4.	Summary of the results	87
6.2.3.	Discussion.....	88
6.2.4.	Summary and conclusions	92
7.	FePt nanoclusters	93
7.1.	The effect of the sputtering gas and the deposition pressure on clusters formation ..	93
7.1.1.	Experimental parameters	93
7.1.2.	Results	94
7.1.3.	Discussion.....	98
7.2.	FePt/Ag nanocomposite layers.....	99
7.2.1.	Experimental parameters	100
7.2.2.	Results and discussion.....	101
7.2.3.	Conclusion	105
8.	Conclusions	107

Appendix A: The nuclear stopping cross section	I
Appendix B: X-ray scattering from a free electron	II
Appendix C: The equivalence between the Bragg law and the Laue condition	IV
Appendix D: The order parameter \mathcal{S}	V
Appendix E: Langmuir probe measurements	VII
Appendix F: Dependence of the disorder-order transformation on the layer thickness	XI
References	XII

Abstract

The $L1_0$ FePt phase belongs to the most promising hard ferromagnetic materials for high density recording media. The main challenges for thin FePt films are: (i) to lower the process temperature for the transition from the soft magnetic $A1$ to the hard magnetic $L1_0$ phase, (ii) to realize c -axes preferential oriented layers independently from the substrate nature and (iii) to control layer morphology supporting the formation of FePt - $L1_0$ self-organized isolated nanoislands towards an increase of the signal-to-noise ratio.

In this study, dc magnetron sputtered FePt thin films on amorphous substrates were investigated. The work is focalized on the correlation between structural and magnetic properties with respect to the influence of deposition parameters like growth mode (co-sputtering vs. layer – by - layer) and the variation of the deposition gas (Ar, Xe) or pressure (0.3 - 3 Pa). In low-pressure Ar discharges, high energetic particle impacts support vacancies formation during layer growth lowering the phase transition temperature to $(320 \pm 20)^\circ\text{C}$. By reducing the particle kinetic energy in Xe discharges, highly (001) preferential oriented $L1_0$ - FePt films were obtained on α - SiO_2 after vacuum annealing. $L1_0$ - FePt nano-island formation was supported by the introduction of an Ag matrix, or by random ballistic aggregation and atomic self shadowing realized by FePt depositions at very high pressure (3 Pa).

The high coercivity (1.5 T) of granular, magnetic isotropic FePt layers, deposited in Ar discharges, was measured with SQUID magnetometer hysteresis loops. For non-granular films with (001) preferential orientation the coercivity decreased (0.6 T) together with an enhancement of the out-of- plane anisotropy. Nanoislands show a coercive field close to the values obtained for granular layers but exhibit an in-plane easy axis due to shape anisotropy effects.

An extensive study with different synchrotron X-ray scattering techniques, mainly performed at the ESRF, BM-20 (ROBL-Beamline), pointed out the importance of *in-situ* investigations to clearly understand the kinetic mechanism of the $A1 \rightarrow L1_0$ transition and ordering and to control FePt nanoclusters evolution.

Symbols

a	acceleration
a_0	Bohr radius (5.29×10^{-3} nm)
M_A	Atomic mass number
α_c	critical angle
α_i	incident angle
α_T	refractive angle
β	imaginary part of the refractive index
χ	sputtering angle
d	target to substrate distance, lattice plane distance
d_s	sheath thickness
E	energy (eV): <ul style="list-style-type: none"> • E_0 initial energy • E_{kT} thermal energy • E_{iz} ionization energy • E_F energy Fermi level • E_ϕ work function • E_{th} threshold energy for sputtering • E_d threshold energy for displacement
E	electric field
e	elemental electron charge (1.602×10^{-19} As)
ϵ_0	permittivity in free space (8.854×10^{-12} F/m)
F	force
Φ	electric potential
\mathbf{G}	reciprocal lattice vector
$F(\mathbf{Q})$	unit cell structure factor
$f(\mathbf{Q})$	atomic scattering factor
$f^0(\mathbf{Q})$	non-resonant atomic scattering factor
f'	real part of the atomic dispersion correction
f''	imaginary part of the atomic dispersion correction
γ_{se}	secondary electron coefficient
h, k, l	Miller's indices
H	magnetic field (H_0 initial magnetic field)
ΔH	enthalpy of transformation
ΔH_s	heat of sublimation
k	Boltzmann constant (8.617×10^{-5} eV K ⁻¹)

\mathbf{k}	wave vector of X-ray
λ	X-ray wavelength
λ_p	mean free path
λ_D	Debye length
m_i	ion mass
m_e	electron mass
m_g	gas atom mass ($m_i = m_g$)
m_T	target atom mass
m_{sp}	sputtered atom mass ($m_T = m_{sp}$)
μ	linear absorption coefficient
μ_e	electron mobility
μ_0	permeability of free space ($4\pi \times 10^{-7}$ H/m)
n	particle density (m^{-3}) in the plasma (plasma density), refractive index
n_i	ion density
n_e	electron density
N_A	Avogadro number (6.022×10^{23} mol ⁻¹)
p	pressure
Q	transformation activation energy
\mathbf{Q}	scattering vector: Q_x , Q_y and Q_z scattering vector components
θ	Bragg angle, ion incidence angle
R	deposition rate
\mathbf{R}_n	lattice vector in the real space
r_{ce}	Larmor radius
r_g	gas atomic radius
r_{sp}	sputtered atom radius
ρ_e	electron density
ρ_m	mass density
σ	scattering cross section
σ_a	absorption cross section
T	temperature
kT_i	ion temperature (eV)
kT_e	electron temperature (eV)
kT_n	neutral temperature (eV)
T_T	phase transformation temperature
U_s	surface binding energy
v	velocity (m/s)
V_{dc}	applied dc potential
V_{pl}	plasma potential
ω	angular frequency
Z_i	Atomic number of ion

Abbreviations

BSE	Backscattered Electrons
DS	X-ray Diffuse Scattering
DSRO	Directional Short Range Order
FWHM	Full Width Half Maximum
GIXRD	Grazing Incidence X-ray Diffraction
GISAXS	Grazing Incidence Small Angle X-ray Scattering
LRO	Long Range Order
MBE	Molecular Beam Epitaxy
RBS	Rutherford Back Scattering
RT	Room Temperature
SE	Secondary Electrons
SEM	Scanning Electron Microscopy
SRO	Short range order
SZM	Structure Zone Model
TEM	Transmission Electron Microscopy
TTT	Time Temperature Transformation
XMCD	X-ray Magnetic Circular Dichroism
XRD	X-ray Diffraction
XRR	X-Ray Reflectivity

Motivation

In 1898 Valdemar Poulsen obtained the patent for the first telegraphone, the first device in history to apply perpendicular magnetic recording to register a sound magnetically [1]. In 1956, IBM built the first magnetic hard disk drive with the recording density of 2 kbit/in²[2]. After 110 years from Poulsen's telegraphone, on July 2008, Hitachi Global Storage Technologies announced 610 Gbit/in² [3] reached using perpendicular magnetic recording technology with continuous recording media and writing heads with an ultra narrow track pitch of 65 nm.

Market demands for low costs at higher performance had made modern hard disk smaller, lighter and faster; forcing a sharp increase of disk drives areal density that is now the main factor determining the cost per gigabyte, fundamental for the commercial viability of these technologies [4]. However, this increase of areal density, i.e. the amount of bits stored per unit area of the disk, has put in evidence the thermal instability in modern longitudinal recording media. Reducing the volume of a single switching domain, the magnetic data becomes unstable because of thermal fluctuations: this is known as superparamagnetic effect. It can be illustrated by the following simple model considering a longitudinal media as a collection of independent particles (every particle as single magnetic domain) with volume V having an energy barrier for magnetisation reversal $E_B(H, V)$ in presence of an external magnetic field H [2]:

$$E_B(H, V) = E_B^0(V) \left(1 - \frac{H}{H_0}\right)^n \quad (1)$$

where E_B^0 is the activation barrier for magnetisation reversal $E_B^0 = K_u V$ in a single domain particle and K_u is the magnetic anisotropy density. In equation (1), $H_0 = 2 K_u / M_S$ is the intrinsic switching field (M_S is the saturation magnetisation) and n is 1.5, taking into account the 2D random anisotropy axis distribution in isotropic longitudinal media [5]. It clearly rises up that to increase thermal stability of stored data it is necessary to increase the energy barrier E_B . It has been indicated [6] that for at least 5 years of stable data storage, the condition $K_u V > 55 k_B T$ must be fulfilled, indicating the minimum volume V for a magnetic material characterised by a certain K_u .

Increasing crystallinity and epitaxy quality together with reducing defects in the magnetic media can improve thermal stability. But, the introduction of high magnetic anisotropy density materials, like the tetragonal LI_0 phase of FePt ($K_u \sim 5-8 \times 10^7$ erg/cm³ [4, 5, 7]), can allow to widely decrease the single domain volume V down to ~ 30 nm³. The reduction of the domain volume will result in an increase of the Signal-to-Noise-Ratio, that is proportional to $1/D^3$, where D is the grain diameter, and to $1/\sigma^2$, with σ the grain size distribution [8]. The biggest problem related to high K_u materials and in particular to FePt

is the high processing temperature (as shown in the TTT diagrams in paragraph 1.2), which may affect grain growth.

Hitachi reintroduced perpendicular recording method in 2006 [3] considering the superparamagnetic effect an insurmountable limit, already reached by longitudinal recording.

The two techniques differ only in the direction in which the bit is stored (Figure 1):

- longitudinal: the bits are lined up end-to-end along the circular tracks in the disk plane (south-pole to south-pole);
- perpendicular: alternating bits stand with north-pole close to the next south-pole. In this way the magnetic stability is strongly increased.

The most common perpendicular recording set-up is including a soft underlayer with the function to increase the writing procedure by closing the magnetic field lines from one magnetic domain, to the next one.

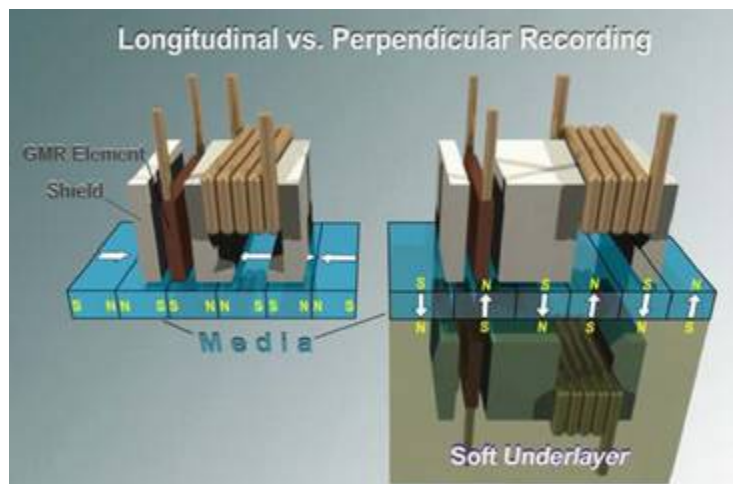


Figure 1: Difference between longitudinal (left) and perpendicular recording (right) [9]

For perpendicular magnetic recording, the magnetic moment M must be parallel with the media surface normal. In the FePt $L1_0$ phase, because of the particular *fcc* structure characterised by alternating monoatomic planes of Fe or Pt stacking along the (001) direction, M is naturally aligned parallel to the lattice c -axis: thus, the control of the crystal orientation on substrates is fundamental for industrial applications.

A different approach to increase areal density is the application of nanocomposite and nanoparticle media. This method does not necessarily imply a technology change from longitudinal to perpendicular recording but only requires monodisperse non interacting single domain grains, organized in arrays. For these applications, high K_u materials are better exploited. Nanocomposite media are realized by annealing of multilayer structures then transformed into decoupled hard magnetic FePt clusters in a diamagnetic matrix [10 - 12].

Monodisperse particles are mainly realized by chemical synthesis [13], followed by annealing. This last step often leads to particles agglomeration because of the high annealing temperature required to obtain the strong ferromagnetic phase [14].

Therefore, the general challenge for FePt as a promising candidate for high density recording media is to lower the transition temperature to obtain the strong ferromagnetic $L1_0$ phase at a temperature that prevent grain coalescence and/or to identify the most suitable matrix in which may exist dispersed and magnetically decoupled FePt nanoparticles.

The aim of this thesis is to identify solutions to these three main problems:

- A. low temperature processing: to understand and control the phase transition kinetics to obtain the strong ferromagnetic phase at processing temperature below 400°C
- B. c -axis orientation: fundamental for perpendicular recording is the control of the layer preferential orientation independently from the substrate nature
- C. nanocluster and nanocomposite layer fabrication at low processing temperature.

The FePt films and nanoclusters will be produced by DC magnetron sputtering, a physical vapour deposition method (PVD), on amorphous substrates. The choice of a -SiO₂ is related to the approach to investigate FePt phase transformation kinetic and c -axis orientation independently from the nature of the substrate making these results useful for FePt films grown by DC magnetron sputtering in general.

Magnetron sputtering deposition process has several advantages compared to other PVD technologies (e.g. evaporation, pulse laser ablation):

- suitable to deposit almost any elemental, alloy or dielectric (multi)layers using dc, rf or pulsed power sputtering with neutral or reactive gases,
- strong variability in the deposition rate (0.01 - 10 nm/s),
- grown films with good uniformity, low roughness and good substrate adhesion,
- the deposition temperature can be varied widely independent from the sputter conditions, including the possibility to keep the substrate at room temperature during layer growth,
- easy scale-up process with overall low costs.

X-ray scattering investigations will be widely applied to study FePt layer structural properties. The phase transformation kinetic and clusters formation and evolution will be studied by *in-situ* X-ray analysis carried out with a synchrotron source (ROBL-ESRF). The control of FePt thin layer c -axis orientation will be achieved by tuning growth and annealing parameters according to the results provided by the X-ray measurements.

1. Iron Platinum

1.1. The FePt $A1$ and $L1_0$ phases

Room temperature (RT) as-deposited FePt layers always exhibit the soft ferromagnetic phase $A1$, chemically disordered; a subsequent annealing is required to obtain the disorder - order transition to the hard ferromagnetic $L1_0$ phase [7, 15 - 20]. The chemically disordered $A1$ phase (Figure 1.1) is metastable (γ Fe, Pt) in which the atoms are statistically arranged in an fcc cell: every site is occupied indiscriminately by an Fe / Pt atom. Therefore, no long range order but only the short range one persists since the occupancy of one site from Fe or Pt can influence only the first neighborhood sites [21]. The $A1$ phase, whose prototype is Cu, has space group (SG) $Fm\bar{3}m$ with $a = 3.816 \text{ \AA}$ [22]: a scheme of the unit cell is represented in the following figure, associated to the calculated X-ray diffraction pattern at Cu- $K\alpha$ wavelength. The FePt $A1$ phase is characterized by a magnetization along the $[111]$ axis [23].

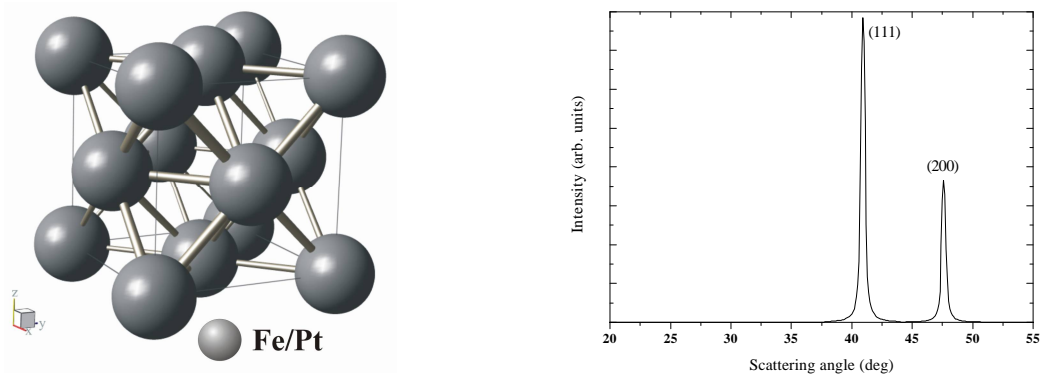


Figure 1.1: $A1$ FePt phase, the XRD pattern generated by Cu- $K\alpha$ radiation in a convenient angular range [22].

The $L1_0$ phase (figure 1.2) is strong ferromagnetic and Fe and Pt are arranged in stacked planes in an fcc structure with $a = b = 3.852 \text{ \AA}$ and $c = 3.713 \text{ \AA}$ [24].

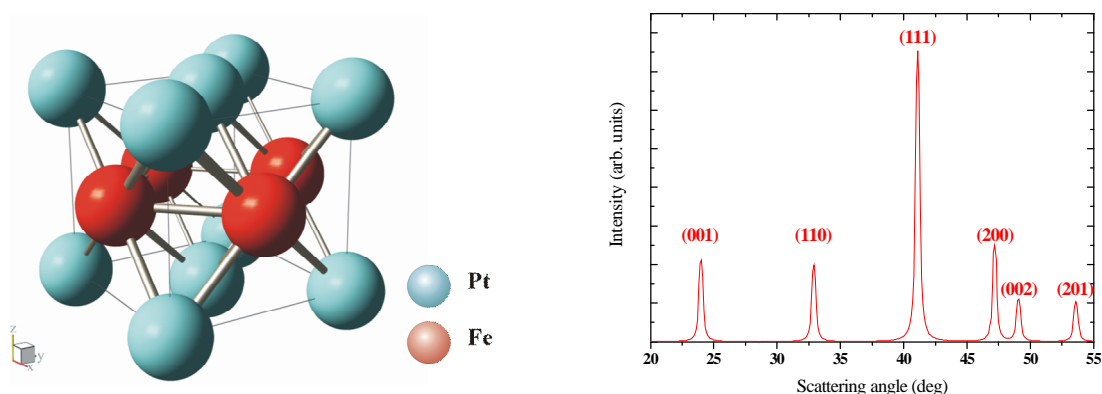


Figure 1.2: $L1_0$ FePt phase, the XRD pattern generated by Cu- $K\alpha$ radiation, in an opportune angular range [24]

The $L1_0$ is obtained from the Al phase by compression along the c axis of 2.7% and a weak dilatation along a of 0.9%: the corresponding decrease of the unit cell volume is characteristic for disorder – order transformations. The slight tetragonal distortion leads to a shift of the (111) reflection to higher scattering angles because of a shorter interplanar distance $d_{(111)}$. The $Al \rightarrow L1_0$ phase transition is clearly characterized by the appearance, in the XRD pattern, of the (001), (110) and (201) peaks and by the splitting of the (200) reflection into the (200) and (002).

The unambiguous site occupancy by Fe or Pt atom is generating a long range order (LRO) that can be quantified by considering the fraction of Fe / Pt atoms sitting in the correct site. Indicating with:

- $x_{Fe/Pt}$ the alloy stoichiometry, $x_{Fe} + x_{Pt} = 1$
- $y_{Fe/Pt}$ the fractions of Fe-sites and Pt-sites,
- $r_{Fe/Pt}$ the fraction of Fe / Pt sites occupied by the right atom,
- $w_{Fe/Pt}$ the fraction of Fe / Pt sites occupied by the wrong atom

and considering that:

1. $r_{Fe/Pt} + w_{Fe/Pt} = 1$,
2. $y_{Fe/Pt} r_{Fe/Pt} + y_{Pt/Fe} w_{Pt/Fe} = x_{Fe/Pt}$: the fraction of sites occupied by the Fe / Pt atoms must be equal to the amount of Fe / Pt atoms,

it is possible to define a LRO parameter S [21]:

$$S = r_{Fe} - w_{Pt} = r_{Pt} - w_{Fe} = \frac{r_{Fe} - x_{Fe}}{y_{Pt}} = \frac{r_{Pt} - x_{Pt}}{y_{Fe}} \quad (1.1)$$

obtaining a criterion to judge the quality of the $L1_0$ phase. The S parameter reveals which fraction of atoms had occupied the right site: $S = 1$ is only possible for an equiatomic composition having the ideal atom distribution, while $S < 1$ for non-stoichiometric compounds, even in a perfect order arrangement. S will be equal to 0 in a random distribution. Experimentally, by XRD, the intensities of the superstructure reflections (peaks vanishing when the order vanishes) are proportional to the square of the S parameter. Therefore, the LRO along the c -axis can be evaluated comparing the integral intensity of the (001) and the (002) reflections (see appendix D).

When the disorder – order transformation occurs, there is a spontaneous re-alignment of the magnetisation parallel to the cell c -axis. This effect occurs because of the sequential Fe or Pt layer stacking: the FePt strong perpendicular magnetic anisotropy is connected to the anisotropy of the tetragonal structure of the $L1_0$ phase [25, 26]. This is due to spin-orbit interactions: the spin magnetic moment for Fe was calculated at $2.9 \mu_B$ while for Pt it decreased to $0.3 \mu_B$. The magneto-crystalline anisotropy is defined as the difference in the total energy between the in-plane axis [100] and [110] and the easy axis [001]. By XMCD measurements and ab-initio calculations [25, 26] it was found that the energy difference between the [100] and the [110] direction is negligible as compared with that one in the

[001] axis. The easy magnetisation axis was found to be the [001] with a magneto-crystalline anisotropy of about 4 meV in FePt.

1.2. The $A1$ to $L1_0$ phase transformation in FePt

The FePt phase diagram is reported in Figure 1.3. The thermodynamically stable $L1_0$ phase can be obtained, for a wide range of stoichiometry ratio between 33% and 55%, from the metastable $A1$ structure by gradual cooling.

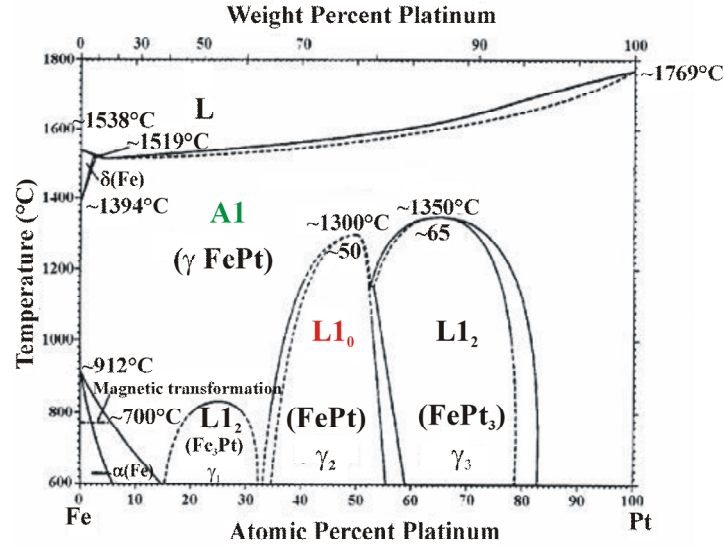


Figure 1.3: Fe-Pt phase diagram [27].

When deposited onto substrates at RT, the alloy films arrange in the $A1$ phase, thus requiring post-deposition annealing to form the chemically ordered $L1_0$ phase [7, 15 - 20]. For media manufacturability, it is of interest that the ordering takes place at the lowest possible annealing temperature, preferably $< 400^\circ\text{C}$ [4, 5].

To understand the kinetics of the FePt phase transformation, an exhaustive study has been proposed by D. C. Berry *et al.* [16, 28] based on Differential Scanning Calorimetry (DSC) investigations of a freestanding $1\ \mu\text{m}$ thick FePt layer. Correction factors to apply the model also to 10 nm films and nanoparticles were derived. According to these experiments, the phase transformation is of the first order (with an Avrami exponent $n = 1.89$ [16]), and occurs by nucleation and growth of ordered $L1_0$ domains in the $A1$ matrix. The model proposed is an application of the Johnson and Mehl, Avrami and Kolmogorov (*JMAK*). The volume fraction transformed X_v can be expressed as:

$$X_v = 1 - \exp\left[-v^n \exp\left(-\frac{nQ}{k_B T}\right) t^n\right] \quad (1.2)$$

supposing the $L1_0$ nuclei growth velocity v given by:

$$v = k_2(T) \exp\left(-\frac{Q}{k_B T}\right) \quad (1.3)$$

where Q is the transformation activation energy, T is the temperature in Kelvin. $k_2(T)$ is the rate constant allowed to be temperature dependent and takes into account the growth of a constant number of pre-existing $L1_0$ nuclei which density is not temperature dependent. The formation of $L1_0$ nuclei, in the as-grown layer, is supposed to be athermal and occurs only by statistical arrangement of the Fe and Pt atoms during deposition.

In Figure 1.4 the Time Temperature Transformation (TTT) diagrams are reported. The calculations are performed applying the *JMAK* model.

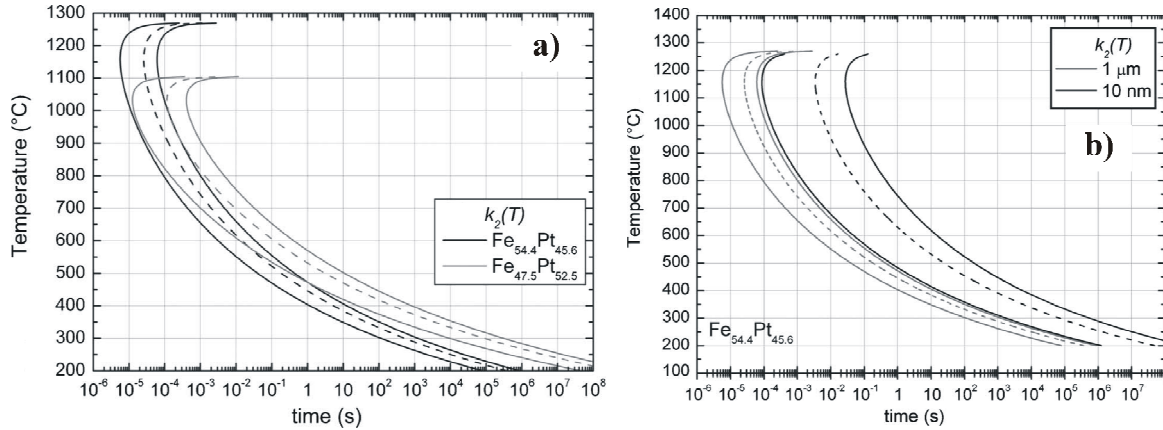


Figure 1.4: TTT diagrams are comparing the transformation kinetics vs. FePt stoichiometry (a) and thickness (b) [16]. The leftmost solid line represents a fraction transformed of 0.05, while the dashed line and the following solid line are 0.50 and 0.95, respectively.

The TTT diagrams give the relation between annealing time and temperature to achieve a certain $L1_0$ fraction in the layer. The FePt alloy composition affects the phase transformation kinetics. Figure 1.4-a shows that for Fe-rich layers the phase transformation, at a given temperature, starts earlier than for the Pt-rich samples. The “nose” position is shifted, for higher Fe concentration, to temperatures close to the steady-state transformation temperature shown in the binary alloy phase diagram (Figure 1.3) indicating lower $L1_0$ nuclei density. At 300°C the time required to have 95% volume fraction transformed is $\sim 10^3$ s for Fe rich specimen and increases to $\sim 10^5$ s for Pt rich.

The model transfer to thin films is done by introducing surface constraints. The medium is not anymore infinitely large and the surface causes a reduction of the growth dimensionally forcing the $L1_0$ domain growth in the direction parallel to the film surface. Thus, the phase transformation is much slower than in the bulk case (see Figure 1.4-b): at 300°C the time required for 95% transformed fraction increases to ~ 167 h and to $\sim 10^8$ s (~ 3 years and 2 months) for Fe rich and Pt rich layers, respectively. A similar approach is applied to calculate the TTT diagrams for FePt nanoparticles. Supposing the nanoparticles isolated, the disorder-order transformation will occur only in nanoparticles having a $L1_0$ nucleus, resulting in a partial magnetic media transformation.

The long time required for annealing conditions close to industrial manufacturing temperatures can be explained considering the value for the activation energy $Q = 1.7$ eV [17, 29] for the ordering transformation, expressing the diffusivity $D(T)$ by:

$$D(T) = D_0 \exp\left(-\frac{Q}{k_B T}\right) \quad (1.4)$$

where D_0 is a characteristic of the material. Rennhofer *et al.* [29] measured a value of $(3.45 \pm 0.44) \times 10^{-13} \text{ m}^2/\text{s}$ for D_0 for Fe diffusion along the c -axis. It is possible to estimate an annealing temperature of 630°C (for an annealing time $t_A = 600 \text{ s}$) to obtain a diffusion length $l_{diff} = \sqrt{D(T)t_A}$ for Fe of 3.7 \AA , close to the unit cell dimension

The annealing conditions before described are clearly not applicable to a real industry production. Thus, intensive studies were performed to lower the transition temperature without losing the peculiar magnetic properties of the LI_0 FePt phase.

Copper doping is one of the most investigated methods to decrease the ordering temperature [16, 28, 30 - 33]. Cu is supposed to form a solid solution with FePt. Maeda *et al.* [32] claimed that the addition of 15 % of Cu, during deposition at RT, caused a strong decrease of the transformation activation energy giving highly ordered layers after annealing at 300°C for 1h with coercive field $H_C = 0.5 \text{ T}$. Cu doping revealed to have the same effect as Fe in reducing the transformation temperature in equiatomic FePt layers [16, 30]. In particular, Wierman *et al.* [30, 33] attributed the decrease of the ordering temperature and rate to the formation of in-plane residual stress caused by Cu/Fe doping. A similar approach is investigated by Lai *et al.* [31] with the addition of a Cu underlayer (100 nm), forming Cu_3Si during annealing that is introducing in-plane tensile stress in the FePt layer supporting the formation of the hard ferromagnetic phase at 300°C .

As another approach, ion irradiation [34 - 39] was performed in order to create vacancies in as-deposited layers. He ions were implanted at energies between 30 and 130 keV and fluences of 1 to $4 \times 10^{16} \text{ ions/cm}^2$, during irradiation the sample was heated at 280°C . The irradiation parameters were chosen in order to minimize displacement cascades, limiting recoils formation to 1 – 3 interatomic distances and ensuring that all He ions will stop into the substrate. The formation of the LI_0 phase in MBE grown FePt layers is obtained at the irradiation temperature and justified with an increase of atom mobility because of vacancies creation during irradiation.

In order to reduce the atomic rearrangement path, during annealing, to an atomistic scale sequential depositions of multiple Fe/Pt stacks [10, 35, 40 - 42] were investigated. It is fundamental to notice the crucial importance of the growing process based on the increasing of the probability to realize a structure that emulates the desiderate LI_0 phase already during layer growth. The annealing temperature to achieve the LI_0 phase was, in most cases, around 550°C .

Our study related to the AI to LI_0 phase transformation phase is described in chapter 5.

1.3. Generation of the (001) preferential orientation in FePt $L1_0$ layers

Because the magnetic moment is naturally aligned along the c -axis, it is necessary to force a (001) preferential orientation to the $L1_0$ layer on a substrate to fulfill the request of perpendicular recording media. One of the most commonly used methods is heteroepitaxy growth of FePt films on suitable crystalline substrates or buffer layers. A schematic explanation of this method is shown in figure 1.5.

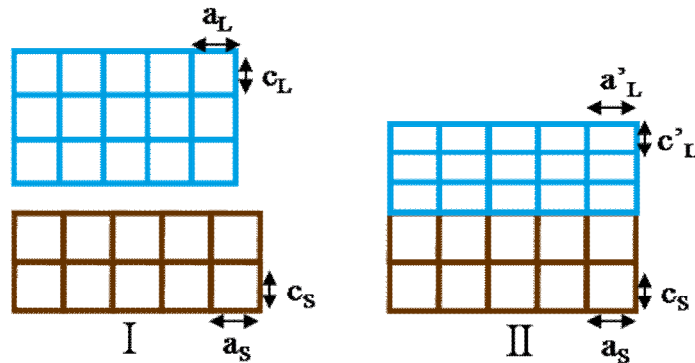


Figure 1.5: Heteroepitaxy growth: I) before $a_s = c_s > a_L = c_L$ and II) after deposition: $a'_L > a_L$; $c'_L < c_L$.

When the FePt layer is deposited on a crystalline substrate with a certain lattice misfit $\varepsilon = (a_s - a_L)/a_s$, the lattice constants of the film will expand or contract to merge the lattice constants of the substrate. When the misfit is negative, $a_L < a_s$, the layer lattice constants will be expanded in the in-plane direction and shrunk along the film normal, as the tetragonal distortion that occurs in the $A1$ to $L1_0$ phase transformation. Therefore, stress induced by lattice misfit is supporting the reduction of the disorder – order transformation temperature.

Several combinations have been investigated: from (001) MgO single crystal (misfit $\sim 8.86\%$) [an extensive study in references 40, 43, 44] to buffer layers as Ag [45 - 47], Cu [47 - 50] and Pt [51]. A complete study was carried out on Cr [20] and its alloys [52 - 56]. The Cr (002) plane has atomic arrangement close to the FePt (001), an epitaxial relationship $\text{Cr}(002)[110]||\text{FePt}(001)[100]$ supports the (001) FePt preferential orientation. The lattice misfit between Cr (002) and FePt (001) is 5.8% [54] and can be further optimized by the use of the opportune Cr alloy. At this purpose, different elements have been investigated: Mo, W, Ti, but the best results were found with $\text{Cr}_{90}\text{Ru}_{10}$ alloy having a misfit of 6.5%: in this condition it was observed the $L1_0$ phase after depositions at 300°C [54].

It is also possible to force the (001) FePt preferential orientation without the use of a crystalline substrate or buffer layer: if, already during deposition, a structure close to the (001) $L1_0$ phase is created by sequential deposition of Fe and Pt thin films [10, 35, 40 - 42]. This methodology is suitable for layers deposited by MBE [35]. The final (001) preferential orientation depends on the creation of directional short range order (DSRO)

area that will grow during annealing [35]. The preferential orientation appears to be related to the configuration of nearly monoatomic layers controlled by the annealing time [40].

In this thesis it will be described the effect of the deposition technique, comparing co-sputtering and layer – by – layer growing methodology, in relation with the growing conditions such as sputtering gas and pressure (Chapter 6).

1.4. Nanoclusters formation

Nanoclusters with diameters from 1 to 10 nm have been of increasing interest, especially in the last years, because of an enhancement of their magnetic properties at decreasing size. For example, at temperatures below 120 K, small nanoclusters of Fe (between 25 and 130 atoms) showed magnetic moment of about 3 μ_B , considerably higher than the bulk Fe (2.2 μ_B) [57]. The developed of high density magnetic recording media to 1 Tbit/cm² imposes grain size to about 8 nm [57], therefore nanoclusters of high K_u materials are indicated as ideal candidate for this application. Sun *et al.* [13, 14, 58] prepared FePt nanoparticles with a very uniform particle size and narrow size distribution via chemical synthesis, but this procedure does not prevent clusters coalescence during annealing. A more suitable technique is to realize FePt nanocomposite films consisting in FePt grains dispersed in a paramagnetic matrix, acting as magnetic barrier. The most common way is to realize a multilayer structure consists in subsequent stacking films of the paramagnetic material and FePt: during annealing the additive will diffuse at the FePt grain boundaries forcing the FePt cluster formation. This effect is related to different surface energies between the “matrix” and FePt that ensure that the additive is not included in the FePt clusters. Carbon was investigated [59, 60] because of its properties as solid lubricant in decreasing the friction between the recording media and the writing head. The use of an insulating matrix, such as MgO, Al₂O₃, BN or SiO₂ [10, 61 - 69] provide well separated nanoislands with an average size between 20 and 100 nm, according to the fraction of insulating matrix, after annealing between 400 and 700°C. A very suitable matrix material has been identified in Ag [11, 12, 70 - 73], having surface energy of $\sim 7.11 \times 10^{14}$ eV/cm² [74] smaller than FePt ($\sim 1.31 \times 10^{15}$ eV/cm² [75]). From a multilayer such as FePt (2-12 nm) / Ag (0.25-4 nm) deposited on MgO, FePt L1₀ nanoislands were obtained after annealing at temperatures above 400°C.

In this work, the role of the Ag thickness in FePt formation and growth at 400°C will be investigated by GIXSAS investigations (chapter 7.2).

A more exotic route is to enhance the deposition gas pressure in order to increase the oblique component of the atom stream, enhancing atomic shadowing and, as a consequence, clustering during growth. Y. Itoh *et al.* [76, 77] investigated different FePt multilayer stacking sequences deposited at 1.2 Pa, for a total layer thickness below 3 nm. They obtained partially isolated FePt L1₀ grains, with average size of ~ 17 nm, after RTA at 500°C. This methodology will be investigated in this thesis (paragraph 7.1) as well.

2. The deposition process

In the following paragraphs, a brief description of the magnetron sputtering technique will be given, accompanied by few basic notions of plasma properties and particle transport into plasma needed to understand the influence of different deposition parameters on film morphology and physical properties.

2.1. Basic plasma notions

“A plasma is a quasi neutral gas of charged and neutral particles which exhibits collective behaviour” [78]. The *quasineutrality* rises up from the plasma ability to shield electric potentials with the creation of sheaths, a positive charged layer (see Figure 2.1).

The sheath thickness d_s is measured by the *Debye length*

$$\lambda_D = \sqrt{\frac{\epsilon_0 k T_e}{n_e e^2}}, \quad d_s = n \cdot \lambda_D \quad \text{with } n \geq 2 \quad (2.1)$$

Only the electron contributions, T_e and n_e , are used to calculate λ_D , being electrons more mobile than ions and hence responsible of sheath formation. For example: for $kT_e = 1$ eV and $n_e = 10^9$ cm⁻³ $\rightarrow \lambda_D = 0.25$ mm. The condition that the system dimension d is much larger than d_s ensures that the bulk plasma is unperturbed from local charge concentrations and external electric potentials. The amount of particles in the *Debye sphere*, the interaction volume of every charge with all other charged particles, is the *plasma parameter* $N_D = \frac{4}{3} \pi \cdot n \cdot \lambda_D^3$, depending on n , the plasma density, it expresses the collective plasma behaviour for $N_D \gg 1$.

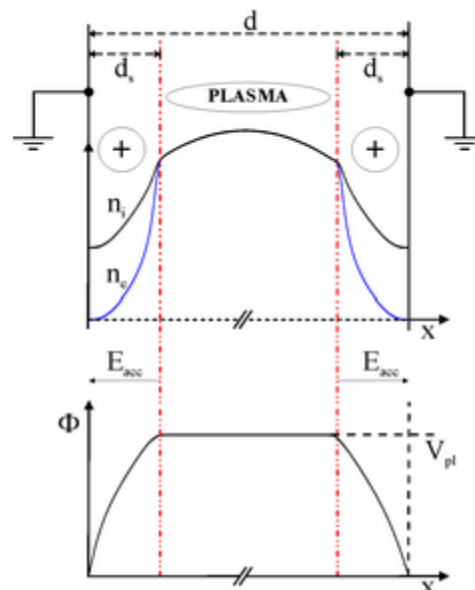


Figure 2.1: A plasma sheath: the behaviours of the densities n_i and n_e , the potential Φ and electric field E_{acc} are shown [79].

Conservation laws can be described by the Boltzmann equation of motion for each particle [78 - 80]:

$$\frac{\partial f}{\partial t} + \mathbf{v} \cdot \nabla_{\mathbf{r}} f + \frac{\mathbf{F}}{m_{e,i}} \cdot \nabla_{\mathbf{v}} f = \left. \frac{\partial f}{\partial t} \right|_{coll} \quad (2.2)$$

where $f(\mathbf{r}, \mathbf{v}, t)$ is the distribution function in the six-dimensional phase space (\mathbf{r}, \mathbf{v}) of particle positions and velocities and the right side term takes into account particle collisions.

Because of the complicated plasma behaviour, sustained in steady conditions by a continuous ionization of gas atoms by electrons, compensating the charge loss at the plasma boundaries or by recombination ($n \approx n_e \approx n_i$), it is necessary to apply some simplified models to derive main plasma parameters from equation (2.2). In particular, macroscopic quantities must be defined by making an average over the particle velocity coordinates, reducing the dependency to three spatial coordinates and the time. For the mean velocity and the mean kinetic energy this will be:

$$\langle v \rangle = \int \mathbf{v} \cdot f(\mathbf{r}, \mathbf{v}, t) d\mathbf{v} \quad , \quad \langle E \rangle = \frac{1}{2} m \int \mathbf{v}^2 f(\mathbf{r}, \mathbf{v}, t) d\mathbf{v} \quad (2.3)$$

These equations must be solved for each particle species to obtain plasma parameters. This can be done assuming a Maxwellian distribution for the function $f(\mathbf{r}, \mathbf{v}, t)$:

$$f(\mathbf{v}) = \left(\frac{m}{2\pi kT} \right)^{3/2} \exp\left(-\frac{mv^2}{2kT} \right) \quad (2.4)$$

This condition implies that the considered particle ensemble must be in thermal equilibrium at the temperature T with itself.

In plasmas generated by low pressure discharges, particles are almost never in thermal equilibrium between each other. Applied potentials will mainly affect electron motions while ions will exchange energy with the background gas atoms. The number of particle collisions will not be large enough to ensure thermalization between ions, electrons and neutrals, leading to $T_e \gg T_i \sim T_g$.

Under the Maxwellian distribution hypothesis the macroscopic quantities become:

$$\langle v \rangle = \sqrt{\frac{8kT}{\pi m}} \quad , \quad \langle E \rangle = \frac{3}{2} kT \quad (2.5)$$

The Maxwellian distribution can be expressed in term of energy:

$$g(E) dE = f(v) v^2 dv \quad , \quad g(E) = \frac{2}{\sqrt{\pi}} \sqrt{E} (kT)^{-3/2} \exp\left(-\frac{E}{kT} \right) \quad (2.6)$$

and the electron density n_e and the average electron energy will be:

$$n_e = \int_0^\infty g(E) dE \quad \text{and} \quad \langle E \rangle = \frac{1}{n_e} \int_0^\infty E \cdot g(E) dE . \quad (2.7)$$

The main characteristics of low pressure plasma are the electron and ion temperatures, the electron and ion densities and the plasma potential. These quantities can be derived from Langmuir probe measurements (Appendix E) as a function of the experimental conditions.

2.2. DC glow discharges

A glow discharge can be generated in a vacuum chamber containing an opportune gas by applying a dc potential V_{dc} between two electrodes at a distance d . If peculiar conditions of pressure p , distance d and voltage V_{dc} are realized, the gas will be ionized by free electrons that, accelerated away from the cathode, will acquire enough energy to overcome gas ionization barriers E_{iz} (Ar: 15.8 eV and Xe: 12.1 eV) [81] and ignite a plasma.

The *breakdown voltage* V_b as a function of the product pd – known as *Paschen curve* - is a characteristic parameter of the dc discharge process to ignite the plasma:

$$V_b = \frac{B \cdot pd}{\ln(A \cdot pd) - \ln\left[\ln\left(1 + \frac{1}{\gamma_{se}}\right)\right]} \quad (2.8)$$

V_b strongly depends from the gas pressure but only slightly from the electrodes material through the secondary electron coefficient γ_{se} ; for Ar and Xe gases the *Paschen curves* are plotted in Figure. 2.2. There is a limit value for $pd = A^{-1} \cdot \ln\left[1 + (1/\gamma_{se})\right]$ below which the plasma cannot be ignited.

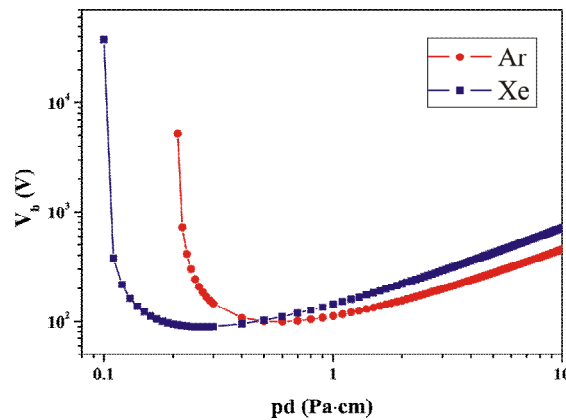


Figure 2.2: An example for Paschen curves: Ar and Xe are compared. ($A_{Ar} = 0.087 \text{ cm}^{-1} \text{ Pa}^{-1}$, $B_{Ar} = 1.323 \text{ cm}^{-1} \text{ Pa}^{-1}$; $A_{Xe} = 0.180 \text{ cm}^{-1} \text{ Pa}^{-1}$, $B_{Xe} = 2.481 \text{ cm}^{-1} \text{ Pa}^{-1}$) [79].

Ions will be accelerated across the sheath towards the cathode (target) and hit that with an energy $E_0 = C \cdot e \cdot V_{dc}$, where C is a constant, depending from the pressure. For collisionless sheaths, C is close to unity, i.e. the energy of the incident ions corresponds directly to the

target voltage, which is valid for all working pressures here considered (sheath thickness ≤ 1 mm) [82]. Keller *et al.* [83] indicated a value of 7.3 Pa·cm at which it was observed a mean ion energy of about 0.75 time the target applied voltage V_{dc} .

Electrons will be repulsed from the cathode causing a lack of electrons close to the target: a positive charged area, the *cathode fall* or *Crookes dark space*, is created, where most of the voltage drops. To sustain the plasma, it is fundamental to provide charge carriers for current continuity across the sheath. Secondary electrons, emitted after ion impacts with target surface, are fundamental to sustain the current through the *dark space*.

Considering that the electron current density $j(z)$ can be expressed by:

$$j(z) = e \cdot n_e(z) \cdot \mu_e \cdot E_{acc} \quad (2.9)$$

where $n_e(z)$ is the electron density and E_{acc} is the accelerating electric field along z .

For current continuity, $j(z)$ must be equal to the ion current at the sheath edge:

$$j_i(d_s) = e \cdot n_s \cdot u_B \quad (2.10)$$

where u_B is the *Bohm velocity* $u_B = \sqrt{kT_e/m_i}$ (the minimum ion velocity for sheath formation $\sim 10^5$ cm/s [79]), depending on the electron temperature T_e . n_s represents the charge density at the sheath edge, where $n_e(d_s) = n_i(d_s) = n_s$ is assumed. Under these conditions, the ion velocity at the sheath edge u_B results to be, for Ar discharges, one order of magnitude lower than the electron drift velocity $v_e = \mu_e \cdot E_{acc} \sim 10^6$ cm/s [79].

In common magnetron sputtering deposition processes characterised by ion energies below 1 keV, secondary electron emission is caused by *Auger neutralization process* of impacting ions followed by *Auger emission* of an electron from near surface target atoms [79]. It is possible to calculate the secondary emission coefficient γ_{se} , for clean surfaces and with an accuracy of 50%, by an empirical expression [84]:

$$\gamma_{se} \approx 0.016(E_{iz} - 2E_\phi) \quad (2.11)$$

valid in the case of $(E_{iz} - 2E_\phi) > 0$, where E_ϕ is the *work function* of the target material.

The secondary emission coefficient can be approximated to 0.1 in Ar discharges for both elements and is decreasing to 0.02 and 0.06 for Pt and Fe in a Xe discharge, respectively. These values are independent from the incident ion energies below 1 keV [84].

Secondary electrons emitted from the cathode are accelerated towards the anode ionizing the gas atoms and producing gas neutral atoms that, returning into the ground state by emitting photons, will be responsible for the glowing of the plasma. At the cathode sheath edge, electrons had enough energy to carry the current through the dark space but they must be retarded to create plasma like conditions. This occurs in an area of high ionization and excitation, where electrons will lose their energy by collisions. This negative charged area is called *negative glow*.

The ions are accelerated at the sheath edge at the *Bohm* velocity by the plasma potential V_{pl} that has the following expression:

$$V_{pl} = \frac{kT_e}{2e} \quad (2.12)$$

The usual set-up for dc glow discharges, used for magnetron sputter depositions, is the parallel plate configuration (Figure 2.3).

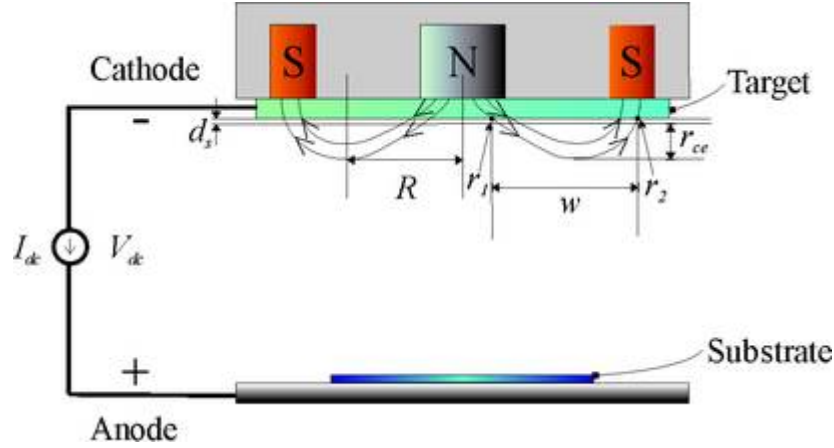


Figure 2.3: Dc discharge: planar magnetron discharge [79]

To increase the sputtering efficiency at low voltage and low gas pressure, a magnetic field is used to trap secondary electrons close to the cathode, enhancing the ionization process. For this purpose, permanent magnets are posed behind the target. When V_{dc} is applied, the high amount of trapped electrons generates a region of enhanced ionization and excitation causing a bright circular glow with radius R and width w (Figure 2.3). Ions will not be trapped by the magnetic field because of the higher mass. The target will not be completely sputtered but a ring will be eroded proportional to the magnetic field line curvature and to the electron *Larmor* radius r_{ce} , which is independent from the target material.

In a low pressure plasma, and therefore in collisionless sheaths in steady state conditions, the ion current density can be estimated from the Child law for a space-charged-limited current [79]:

$$\langle j_i \rangle = \frac{4}{9} \epsilon_0 \sqrt{\frac{2e}{m_i}} \frac{\sqrt{V_{dc}^3}}{d_s^2} = \frac{I_{dc}}{2\pi R w} \quad (2.13)$$

A special challenge for magnetron sputtering is to deposit highly coercive magnetic materials such iron, nickel etc. This metal invariably absorbs a portion of the magnetic field which controls the process and inhibits maximum performances. An empirical solution has been to decrease the thickness of Fe target to 0.4 mm, in agreement with reference [85].

2.3. Sputtering

Dc glow discharges are used for deposition of metals or doped semiconductors via the sputtering process. Thereby, the target is integrated into the cathode which is negatively biased at a potential of typical several hundred volts. Energetic gas ions (Ar^+ , Xe^+), hitting the target surface, transfer their energy to target atoms via electronic and nuclear interactions which includes a collision cascade of knock-on target atoms. A general schema of possible effects during ion impact is shown in Figure 2.4-a.

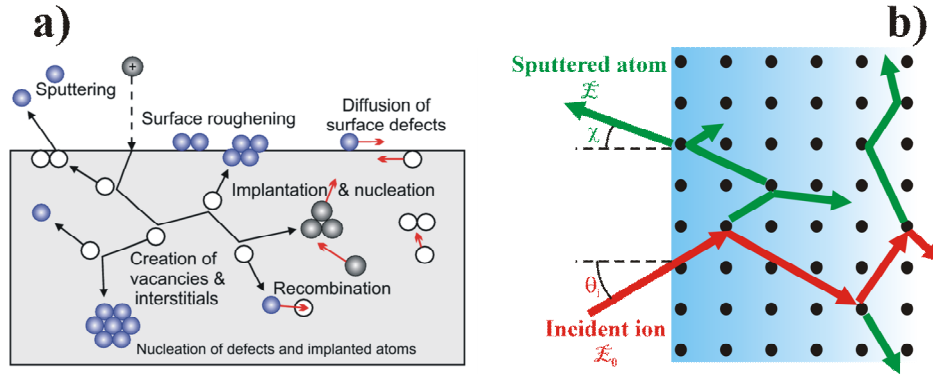


Figure 2.4: a) Interaction due to ion bombardment [86]; b) a sputtering event [87]

An ion will remove atoms from the target (sputtering) if the energy transferred to a surface atom within a collision cascade exceeds the surface binding energy [87]. A schematic presentation of sputtering in the linear cascade regime is given in Figure 2.4-b. The amount of sputtered atoms per incident ion is defined as sputtering yield y_{sp} , which mainly depends on nuclear stopping cross section $S_n(E_0)$, the target surface binding energy U_s and the ion incidence angle θ_i , with respect to the target surface normal. Following the sputtering theory developed by Sigmund [88] and Yamamura [89], the sputtering yield can be described within a wide energy range by:

$$y_{sp} = \frac{j_{sp}}{j_i} = 0.042 \cdot \frac{\alpha(m_T/m_i) \cdot S_n(E_0)}{U_s} \cdot \frac{\beta(E_{th}/E_0)}{\cos^n(\theta_i)} \quad (2.14)$$

j_{sp} and j_i denote the fluxes of the sputtered atoms and incident ions, respectively. E_{th} is the threshold energy for sputtering (E_{th} is equal to 22.6 eV and 32.2 eV for Fe; 23.4 eV and 34.1 eV for Pt impacted by Ar and Xe, respectively [90]). For polycrystalline materials, the heat of sublimation is usually substituted to U_s [91]. The nuclear stopping cross section $S_n(E_0)$ of the incoming ion in the target determines the ion energy dependence of the sputtering yield and its complete expression is reported in Appendix A, together with the correction factors $\alpha(m_T/m_i)$ and $\beta(E_{th}/E_0)$.

The energy distribution of the sputtered atoms follows a modified Thompson distribution [92], where the exponent m takes into account the influence of the collision cascade characteristics [91, 93]:

$$f(E, U_s, \chi) \propto \frac{E}{(U_s + E)^{3+2m}} \cdot \cos \chi. \quad (2.15)$$

A good agreement between simulation and experimental data for $E_o < 1 \text{ keV}$ is obtained with $m \approx 0.17$ [93] which describes something in between a *linear* cascade and a *single knocking* cascade [90]. $f(E, U_s)$ has a maximum for $E_M = U_s / (2 + 2m)$ and scales like $E^{-(2+2m)}$ for $E \gg U_s$, its mean value can be calculated for $\chi = 0$ and $E_o \gg E_{th}$ [94]:

$$\langle E \rangle = 2U_s \cdot [\ln(E_o/E_{th}) - 1.5]. \quad (2.16)$$

The angular distribution of the sputtered particles $f(\chi)$ depends from the incident ion energy E_o , the angle θ_i and the ion/target mass ratio. A realistic description for the incident ions angular distribution is quite complicated, as the sputtering setup, the target surface quality and also its erosion during sputtering are of significant influence. The cosine dependence given in equation (2.15), valid for normal incidence, is a consequence of the assumption of an isotropic cascade, but, for low incident energies and light elements, it has been found a deviation towards a $\sin 2\chi$ behaviour [95].

A gas ion, impacting the target surface, could be immediately neutralized and, if $m_i < m_T$, could be backscattered. This effect is particularly important for sputtering of heavy element targets with light ions (e.g. $\text{Ar}^+ \rightarrow \text{Pt}$) and the probability that this occurs is proportional to the ratio m_T/m_i . The energy carried by reflected gas neutrals usually achieve high values in comparison to the kinetic energies of other particles involved in the sputtering process. For Ar^+ sputtering, the energy reflection coefficient R_E and the fraction of reflected particles R_N has been determined by Drüsedau *et al.* [96] as function of the incident ion and target masses to

$$R_N = \left(\frac{m_T - m_i}{m_N} \right)^\eta, \quad R_E = \left(\frac{m_T - m_i}{m_E} \right)^\gamma \quad (2.17)$$

where the parameters m_N , m_E , η , γ were determined from experimental data for Ar discharges to: $m_N = 806 \text{ amu}$, $m_E = 775 \text{ amu}$, $\eta = 0.59$ and $\gamma = 1.26$ [96].

The mean energy of the reflected neutrals can be calculated by [96]:

$$\langle E_{refl} \rangle_T = r \cdot E_o \quad \text{with} \quad r = R_E / R_N. \quad (2.18)$$

The formulas described in this chapter enable to estimate main sputtering values valid for the conditions used in this work. It shows that for a typical sputter yield $\approx 0.5 - 1.5$ the mean energy of sputtered atoms is between 5-10 eV, whereas reflected gas neutrals can exhibit energies even more than 100 eV for the case of Pt sputtered by Ar ions. In detail, yields for sputtering and neutral reflection as well as the corresponding energy distributions were simulated by the computer program TRIDYN [97, 98] and the results will be discussed in chapters 6-8.

2.4. Energy flux during magnetron sputtering deposition onto the substrate

The morphology and the physical properties of magnetron sputtered films strongly depend on the energy distribution of atoms and ions impacting the substrate. To model the energy transfer the following processes have to be considered [83]:

- sputtering
- transport of sputtered atoms and backscattered gas atoms from the target
- re-emission of deposited material from the substrate by energetic particle impact

The total energy, per deposited atom, is the sum of different contributions [96]:

$$\langle E_{tot} \rangle = U_s + \langle E_{at} \rangle + \langle E_{refl} \rangle + \langle E_{pl} \rangle \quad (2.19)$$

valid under the assumption of an equal angular distribution of the sputtered atom and backscattered gas neutral. The first and the second terms are the FePt surface binding energy and the average kinetic energy of the sputtered atoms at the substrate, respectively. The third represents the contribution of the reflected neutrals (per sputtered atom) and the last one is the contribution of the plasma irradiation, estimated by Thornton [99] to $\langle E_{pl} \rangle = 5.33/y_{sp}$ in eV and y_{sp} in atom/ion, for each sputtered atom.

From the target to the substrate the sputtered and the reflected gas atoms will suffer collisions decreasing their kinetic energy. There are two main particles transport categories: streaming (ballistic transport) and diffusing (thermalized particles). In the first case the main momentum component is perpendicular to the substrate and remains unchanged during scattering, while for diffuse transport the final momentum of particles arriving at the substrate is randomly distributed [100]. On the other side, considering just thermalized particles means that all the sputtered atoms had suffered at least one large angle scattering collision. Petrov *et al.* [82] identified a gas pressure range for the crossover between ballistic and diffusion transport. These results, for a Vanadium target at $d = 10$ cm from the substrate, underline as the thermal diffusion fraction becomes predominant already at pressures greater than 0.2 Pa for Xe and 0.7 Pa for Ar.

The mean free path λ_p is proportional to the gas working pressure p and the collision cross section σ :

$$\lambda_p = \frac{kT}{p\sigma}. \quad (2.20)$$

The collision cross section is energy dependent and it can be approximated by [100]:

$$\sigma(E) = \sigma(E_{kT}) \left(\frac{E}{E_{kT}} \right)^{-0.29} \quad (2.21)$$

with E_{kT} , considered to be equal to 1 eV. The decrease of $\sigma(E)$ with energy is due to the fact that the repulsive part of the pair potential of atoms is of finite slope rather than infinite, like in the classical *hard sphere model* [101].

For $E < E_{kT}$ the particle is supposed to be thermalized and σ can be calculated by [100, 102]:

$$\sigma(E_{kT}) = \pi (r_{sp} + r_g)^2 \sqrt{1 + \frac{1}{M}} \quad (2.22)$$

with $M = m_g/m_{sp}$, where m_{sp} is the sputtered atom mass equal to m_T . r_{sp} and r_g are the atomic radii of the sputtered and thermalized deposition gas, respectively.

The average ratio of the final energy E_f to the initial one E_i after one single collision, assuming an average value between all the minimum approach parameters, can be expressed as [102, 103]:

$$\left\langle \frac{E_f}{E_i} \right\rangle = \exp(-\gamma), \text{ where } \gamma = \begin{cases} 1 - \left[\frac{(1-M)^2}{2M} \right] \ln \left(\frac{1+M}{1-M} \right) & \text{for } M < 1 \\ 1 - \left[\frac{(M-1)^2}{2M} \right] \ln \left(\frac{M+1}{M-1} \right) & \text{for } M > 1 \end{cases} \quad (2.23)$$

Considering a sputtered atom travelling through a distance d , the average lost energy fraction will be:

$$\left\langle \frac{E_{at}}{E_0} \right\rangle = \exp \left(-\frac{d}{\lambda_p} \gamma \right). \quad (2.24)$$

The third component that must be analysed in equation (2.19) is the scattering of fast reflected gas atoms at background gas atoms. Due to the same mass a significant amount of energy and forward momentum loss can be expected.

To evaluate the reflected neural energy impacting the substrate, the relation introduced by Robinson [101] and Somekh [104] can be applied, as suggested by Drüsedau *et al.* [105]:

$$\left\langle E_{refl} \right\rangle = \left\langle E_{refl} \right\rangle_T \exp(-c \cdot pd) \quad (2.25)$$

where $\left\langle E_{refl} \right\rangle_T$ is the mean energy after reflection at the target. Somekh [104] calculated values for the constant c to $0.12 \text{ (Pa cm)}^{-1}$ [105] and $0.28 \text{ (Pa cm)}^{-1}$ for Ar – Ar and Xe – Xe collisions, respectively. The influence of different contributions to the total energy depends on the ratio between the mass of the sputtering gas and the target element: for heavy target materials sputtered with light gases the total energy is mainly due to the reflected gas neutrals.

The fourth point, from the model to describe magnetron sputtering deposition process, concerns the re-emission of material from the substrate because of energetic particle

impacts. At low pressures ($p \cdot d \approx 4 \text{ Pa} \cdot \text{cm}$), this effect is mainly dominated by the temperature dependent sticking coefficient of the sputtered material on the substrate [83].

2.5. Effects of deposition parameters on layer properties

An intensive study about the influence of the adatom mobility, during deposition, was conducted first by Movchan and Demchishin [106] and then by Thornton *et al.* [107, 108, 109], developing a *Structure Zone Model* (SZM) to predict layer morphology and structure as a function of the *reduced deposition temperature* T/T_m , where T is the deposition temperature and T_m is the melting temperature of the target material.

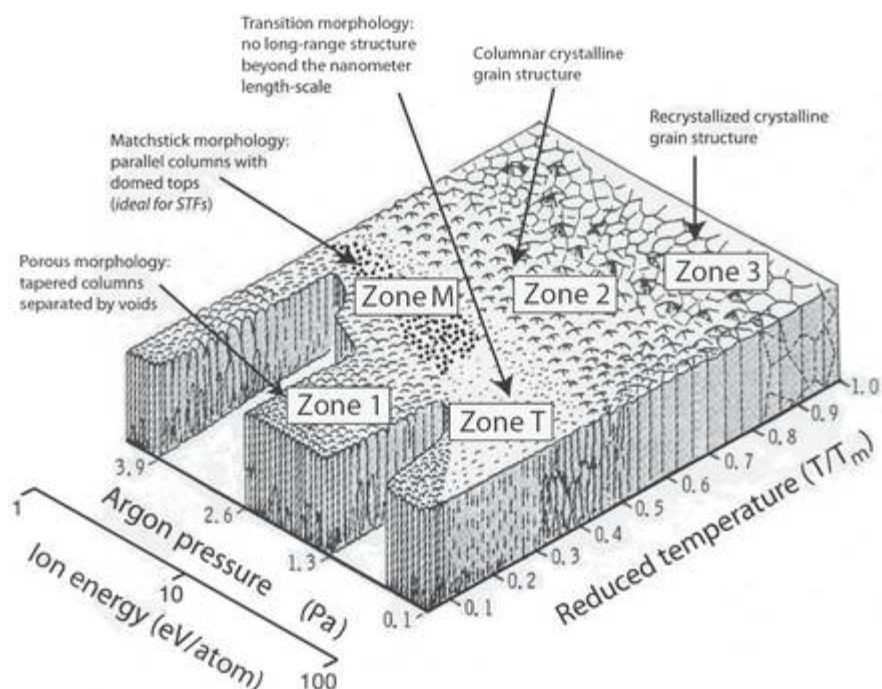


Figure 2.5: Messier's SZM [112]. The investigated parameters are: reduced temperature, pressure during deposition and particle energy impacting the substrate.

The Thornton's SZM takes into account only the thermal activated adatom mobility, while the dependence from the gas pressure and the energy bombardment was introduced by Messier *et al.* [110, 111, 112] together with an additional transition Zone, M, ideal for sculptured thin film growing. This model is reported in Figure 2.5. If considering only the thermally activated adatom mobility, for $T/T_m \leq 0.3$, layers belong to Zone 1. Films are characterized by tapered crystallites forming columns shape grains separated by voids. The film top surface looks like a "cauliflower" as the result of the random ballistic aggregation and atomic self shadowing that leads to clustering. The layer density is strongly reduced with respect to the bulk one due to voids up to 30% of the total film volume [109].

With decreasing gas pressure, the growing layer is bombarded by more energetic particles that stimulate adatom mobility. It is possible to move from Zone 1 (negligible energetic bombardment) to zone M (with low energy bombardment) and to zone T (high energy

bombardment). If the energy impacting the surface is between 4 and 10 eV the layer will have a dome-shaped surface belonging to the Zone M. The growth under intermediate energy bombardment conditions can lead to 1 – 10 nm clusters that evolve in columns of 20 – 200 nm. When ions from the plasma or fast neutrals have sufficient energy to break atomic bonds (Fe, Pt heat of sublimation ≈ 5 eV), the bombardment induced adatom mobility takes place. Energetic bombardment will generate compressive stress in the layer and material redistribution during deposition which leads to hard and chemically inert layers with very smooth surfaces.

Moreover, high energetic particles (ions or neutrals) can generate vacancies in the growing film. Considering that the average displacement energy E_d is ≈ 17 eV for Fe and ≈ 33 eV for Pt [91], a stable Frenkel pair will be generated if $T_M > E_d$, where T_M is the maximum energy transferable in one elastic collision (the suffix *inc* indicates the incident particle):

$$T_M = \frac{4m_T m_{inc}}{(m_{inc} + m_T)} E_{inc} \quad (2.26)$$

The term $\left[\frac{4m_T m_{inc}}{(m_{inc} + m_T)} \right]$ is called the energy transfer factor, which has a maximum of unity when $m_{inc} = m_T$.

From calorimetric studies, Barmak *et al.* [17] identified that the disorder - order transformation in the 50 – 50 FePt system is exothermic, characterized by an enthalpy of transformation of $\Delta H = (-10.2 \pm 1.2)$ kJ/g-atom, with an activation energy of $Q = (1.7 \pm 0.1)$ eV, which is considerably larger than the activation energy for grain growth $\Delta H = -0.22$ kJ/g-atom [43]. Therefore, during annealing, grain growth will be favourite to layer phase transformation.

This situation can be changed by increasing the atom mobility in the layer. Bernas *et al.* [35], with a comparative study on He^+ irradiation of FePt layers and Molecular Dynamics (MD) simulations, pointed out that the disorder – order transformation is strongly supported by vacancies motion (vacancies become mobile in metals at temperatures $\geq 250^\circ\text{C}$). To support the layer growth with high energetic projectile particles can introduce point defects, in the as-deposited films, increasing Fe and Pt diffusivity and reducing the disorder – order transformation temperature.

3. Experimental set-up

In this work FePt was grown by dc magnetron sputtering. In this chapter are described the set-ups used for *ex-situ* and *in-situ* (under X-ray scattering investigations) depositions. RT deposited layers are annealed to obtain the strong ferromagnetic $L1_0$ phase. The thermal treatments are accomplished in different furnaces described in paragraph 3.3.

3.1. The magnetron deposition chamber

A sketch of the vacuum chamber for magnetron sputter deposition is shown in Figure 3.1. The particular geometry of this set-up derives from the need of testing the growing parameters in the same conditions as during *in-situ* X-ray scattering investigations at the synchrotron (paragraphs 3.2, 4.2.4). Therefore the chamber is designed to fit in the six-circle goniometer of the ROBL beam line (paragraph 4.2.4).

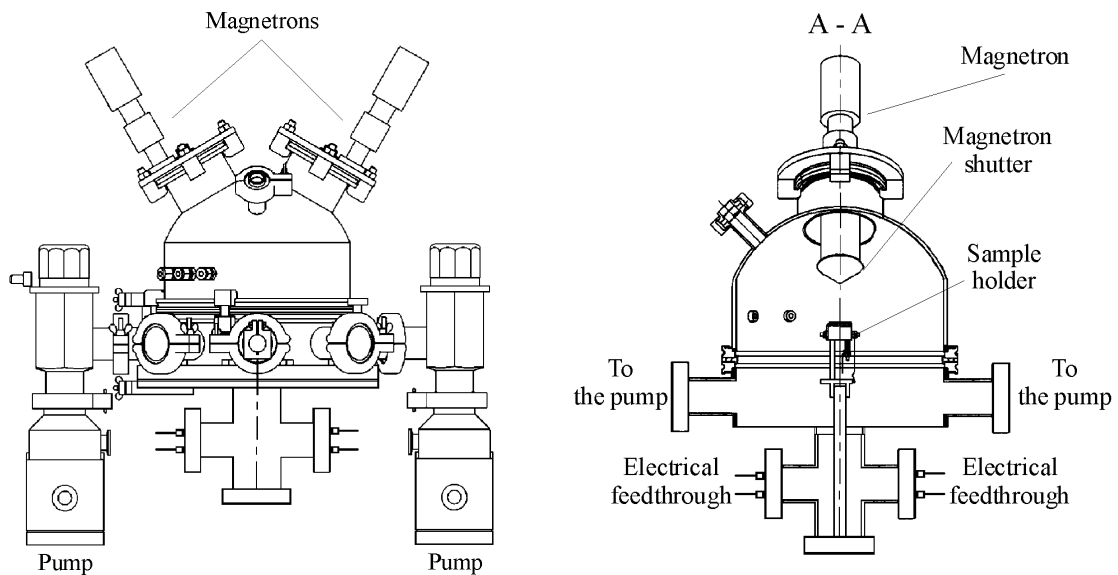


Figure 3.1: Overview of the deposition chamber: left side) front view, right side) section A-A.

The chamber is equipped with two commercial magnetron sources for 1” diameter targets (see Figure 3.2) tilted 30° away from the substrate surface normal at a target-to-substrate distance of 100 mm. The sputtering gas inlets are located close to the targets, separately for each magnetron. Air-pressure-controlled shutters are placed in front of the magnetron chimneys. Below the target a crown of NdB permanent magnets assure a magnetic field H_0 in the order of 20 mT measured at 5 mm along the normal at the target surface.

According to the different targets (Fe, Pt, Ag) sputter yields and discharge pressures, the magnetrons were run with various dc powers in order to obtain FePt films of (50 ± 5) at. % in composition, at low deposition rates ($\leq 0.5 \text{ \AA/s}$). As pointed out in paragraph 2.2, Fe targets only (0.4 ± 0.1) mm thick must be used for the present magnetron

configuration. Thus, the magnetron power of the Fe target had to be re-adjusted from time to time, at least for each new Fe target, to obtain the desired FePt stoichiometry.

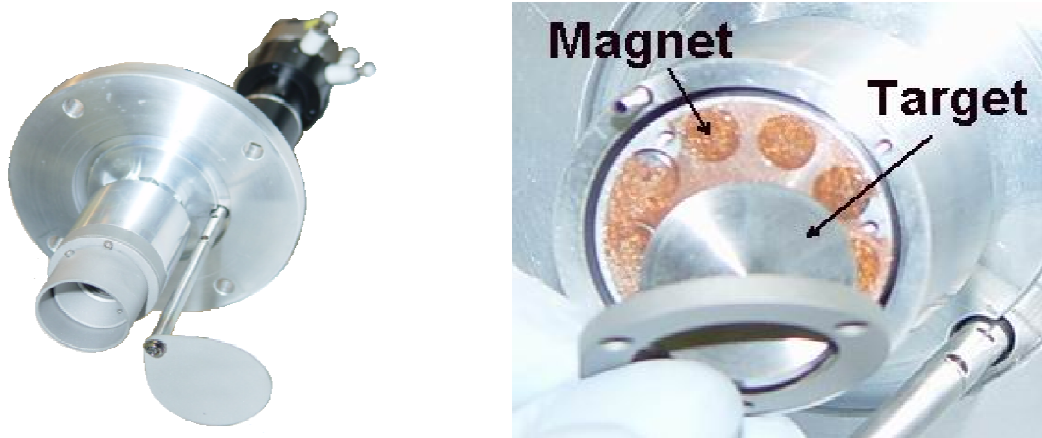


Figure 3.2: Picture of Stiletto ST-10 magnetron source (left), commercially available from AJA International [114] and a detail of the target mounting (right).

The chamber vacuum with a base pressure below 5×10^{-4} Pa is realized by two turbo molecular pumps Leybold TMP-50, connected to the chamber by throttle valves. The sputter gases Ar (5N) or Xe (6N) is introduced via a mass flow controller and kept constant during the whole deposition time. To investigate the effect of the working pressure on the layer morphology and physical properties, Ar or Xe gas discharges at 0.3 Pa and 3.0 Pa has been compared. The pressure was measured with a PFEIFFER compact capacitance gauge CMR 274 that ensure pressure measurements independent from gas type.

Layers were grown at room temperature (RT) or at the temperatures between 300 and 450°C controlled by a *K*-type thermocouple firmly touching the substrate surface.

All films were deposited on $15 \times 15 \text{ mm}^2$ *a*-SiO₂ (1.5 μm or 500 nm) / Si (100) substrates. The lower thickness of *a*-SiO₂ was used to decrease the intensity of the *a*-SiO₂ near-order signal in the X-ray diffraction pattern in order to improve the detection and analysis of the FePt *L10* phase by superstructure peaks (see Appendix D).

<i>Film type</i>	<i>Deposition technique</i>	<i>Magnetron 1</i>	<i>Magnetron 2</i>	<i>Gas</i>	<i>Pressure (Pa)</i>
FePt	Co-sputtering	Fe (3.5N)	Pt (5N)	Ar, Xe	0.3, 3
FePt	Multilayer deposition	Fe (3.5N)	Pt (5N)	Ar, Xe	0.3, 3
FePt / Ag	Multilayer deposition	Ag (5N)	Fe ₅₀ Pt ₅₀ (5N)	Ar	0.3

Table 3-1: Deposition schemes and magnetron configurations. The target purity is indicated in brackets.

In Table 3-1 the main deposition schemes are summarized. Detailed deposition parameters will be specified later, according to the different experiments.

3.2. The magnetron deposition chamber used for *in-situ* investigations at ROBL

In-situ X-ray investigations have been performed at ROBL (BM20), the FZD beamline, situated at one of the bending magnets of the European Synchrotron Research Facility (ESRF) in France [115]. The possibility to tune the X-ray energy, to reduce air scattering and absorption and the high brilliance of the synchrotron source enabled *in-situ* studies of FePt phase transformation and films growth by different X-ray scattering techniques. For that reason a deposition chamber has been designed [116] (Figure 3.3-a), providing X-ray access through Be windows of 71° in the in-plane and 52° in the out-of-plane direction (see Figure 3.3-b).

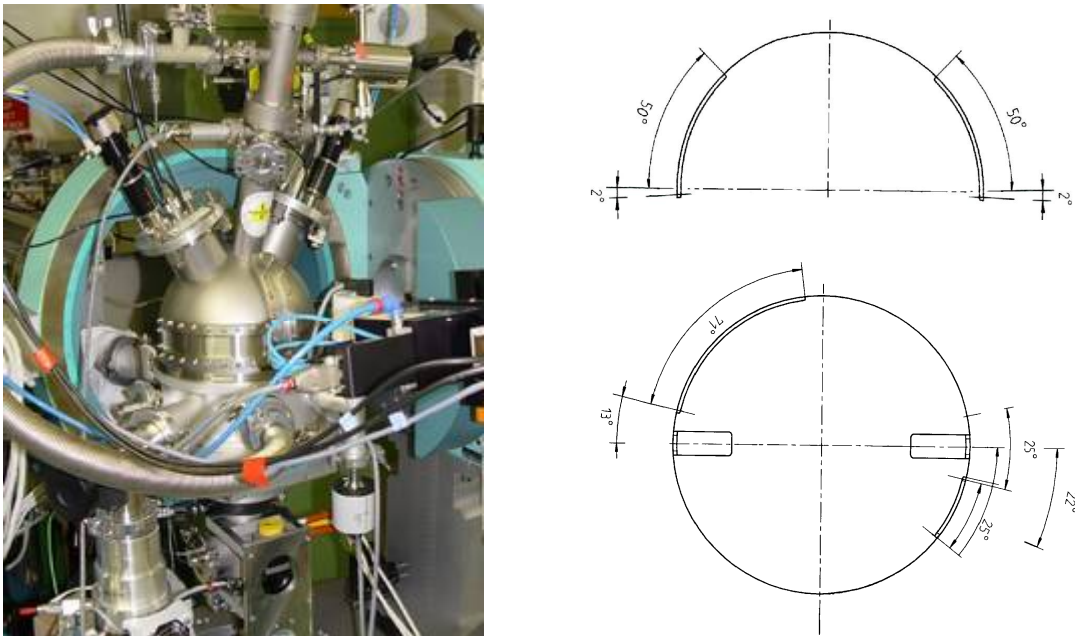


Figure 3.3: Deposition chamber mounted into the six-circle diffractometer of ROBL (front view-detector side), left. Scheme of the accessible angles in the coplanar scattering geometry (top right) and in the non-coplanar one (bottom right).

The magnetron sputtering setup is identical to that described in the previous chapter. The deposition equipment is held by the θ goniometer arm (see Figure 3.3-a) of the Huber six-circle goniometer of the materials research station. The weight of the whole setup is limited to 20 kg in order to keep the high precision of the goniometer settings of 0.001° . Sample alignment is achieved by ± 7 mm vertical movement of substrate holder driven by an external stepper motor connected with a precision slide. Substrate heating was realized by a BORALECTRIC[®] heater [117], integrated into the sample stage, the temperature is measured by a *K*-type thermocouple connected with an EUROTHERM controller. Sample surface temperature is monitored during processing by another *K*-type thermocouple firmly touching the substrate surface.

3.3. Annealing processes

FePt films deposited at room temperature usually exhibit the soft magnetic $A1$ phase (see chapter 1). Subsequent annealing is required to obtain the strong ferromagnetic $L1_0$ phase. Three different annealing equipments have been used in this work which will be briefly described in the following sections.

3.3.1. *Ex-situ* vacuum annealing chamber at FZD

Ex-situ annealing was carried out at FZD in an ultra-high vacuum (UHV) chamber. The sample holder is equipped with a tungsten wire resistance heater and two thermocouples: an S -type controlling the heater temperature and a K -type monitoring the sample surface temperature (see Figure 3.4 inset). The combination of a scroll pump and a turbo molecular pump ensures a base pressure $\leq 1 \times 10^{-5}$ Pa, during annealing at temperatures $\leq 700^\circ\text{C}$ the pressure kept below 5×10^{-5} Pa.



Figure 3.4: UHV annealing chamber at FZD with a view on the sample holder (inset).

3.3.2. *In-situ* vacuum annealing chamber at ROBL

The UHV annealing chamber at ROBL is equipped with a hemispherical Be dome that allows X-ray diffraction analysis in any suitable scattering geometry during thermal treatments. On top of the sample holder, a BORAELECTRIC[®] heater is installed. The heater temperature is controlled by a Eurotherm device via a K -type thermocouple ensuring constant temperature for the time required for X-ray investigations. Another K -type thermocouple is monitoring the sample surface temperature. This value is permanently

measured and saved together with the X-ray analysis data. Annealing was performed at pressures around 1×10^{-5} Pa.

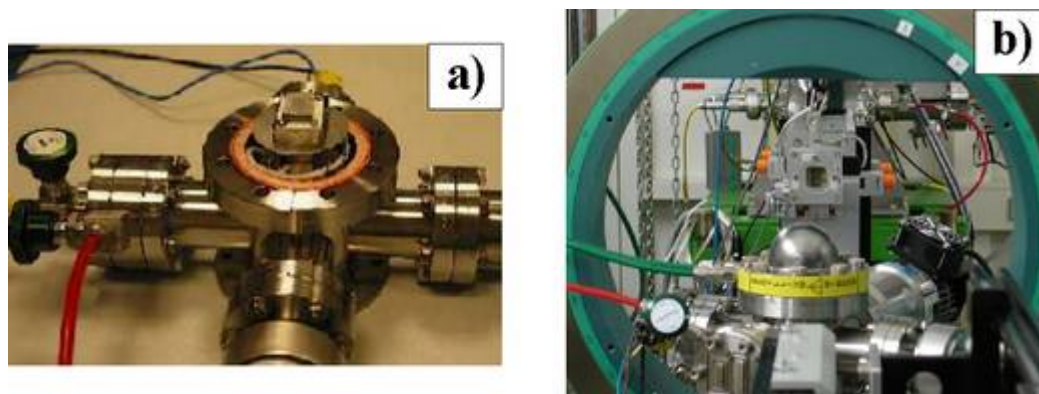


Figure 3.5: Annealing chamber at ROBL: a) view on the sample holder; b) mounted into the six-circle diffractometer (front view-detector side).

3.3.3. Rapid thermal annealing (RTA) at FZD in Ar flow

The RTA facility XM-A4 (ADDAX) is located in the clean room at FZD. The furnace is equipped with two halogen lamp fields above and below the quartz sample holder, allowing high heating rates. The halogen lamps heating power is controlled by a pyrometer located below a 4" diameter Si / *a*-SiO₂ (500 nm) wafer acting as sample holder for small specimens (Figure 3.6-a). A careful temperature calibration was performed to ensure a correct and reproducible annealing process (Figure 3.6-b). For this purpose, test specimens were measured as a function of the heating power by a *K*-type thermocouple touching the sample surface. Annealing is performed under Ar flow (5N, 5 sccm) at temperatures of 550°C or 750°C for 600 s. The temperature ramp of 100°C/s was kept constant for all annealing treatments. The cooling rate, depending on the annealing conditions, remained $\leq 15^\circ\text{C/s}$.

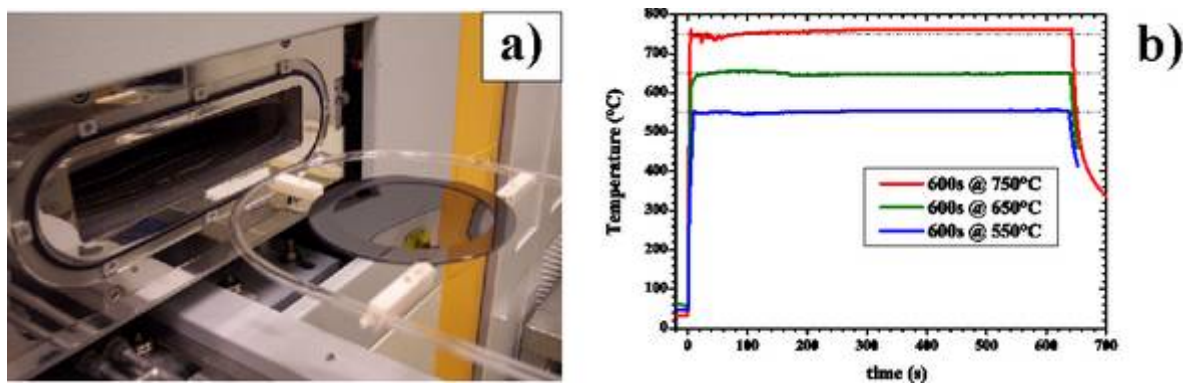


Figure 3.6: RTA set-up: a) view on the sample holder and annealing chamber entrance; b) temperature calibration curves at 550, 650 and 750°C for 600 s.

4. Methods of investigation

4.1. X-ray scattering

The deposited FePt layers are polycrystalline. A crystal is a lattice of points in which every atom is associated to a specific lattice site (Figure 4.1).

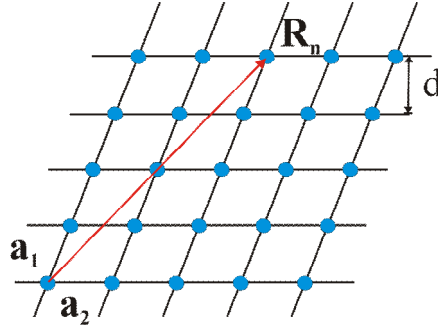


Figure 4.1: A crystal: molecules are organized on a lattice, with spacing d . \mathbf{a}_1 and \mathbf{a}_2 are the basis vectors describing the unit cell [118].

If \mathbf{r}_j is the position of the j 'th atom in the molecule, the position of each atom in the crystal will be identified by the vector $\mathbf{R}_n + \mathbf{r}_j$, where \mathbf{R}_n is the position vector of each molecule in the crystal defined as:

$$\mathbf{R}_n = u\mathbf{a}_1 + v\mathbf{a}_2 + w\mathbf{a}_3 \quad (4.1)$$

where u , v and w are integers. \mathbf{a}_1 , \mathbf{a}_2 and \mathbf{a}_3 are the basis vectors describing the unit cell: they identify the minimum volume of the unit cell, known as *primitive unit cell*. To describe a family of planes the *Miller indices* (h, k, l) were introduced, defined in the way that the plane closest to the origin (but not including the origin) has intercept $(a_1/h, a_2/k, a_3/l)$ on the axes $(\mathbf{a}_1, \mathbf{a}_2, \mathbf{a}_3)$. The planes identified by Miller indices have a constant lattice point density and for a given family of plane they are equally spaced. It is possible to define the lattice spacing d_{hkl} , given for example for a cubic lattice by:

$$d_{hkl} = \frac{a}{\sqrt{h^2 + k^2 + l^2}} \quad (4.2)$$

To measure such structures, having usually dimension of few Å, an opportune probe is required: X-rays, electromagnetic waves with wavelength in the Å range, discovered in 1859 by W. C. Röntgen, are an invaluable tool to investigate the structure of matter.

The classical model to describe X-ray is a linearly polarized plane wave [118]:

$$\mathbf{E}(\mathbf{r}, t) = \boldsymbol{\epsilon} \cdot E_0 \cdot e^{-i(\omega t - \mathbf{k} \cdot \mathbf{r})} \quad (4.3)$$

where $\boldsymbol{\epsilon}$ is the unit polarisation vector and \mathbf{k} is the wavevector along the direction of propagation ($\boldsymbol{\epsilon} \cdot \mathbf{k} = 0$ and $\mathbf{k} \cdot \mathbf{E} = \mathbf{k} \cdot \mathbf{H} = 0$). From the quantum mechanical point of view, a X-ray beam is quantized into photons having energy $\hbar\omega$ and momentum $\hbar\mathbf{k}$: the beam

intensity, expressed in terms of number of photons crossing a certain area in a unit time, is given by the square of the electric field component, the magnitude of the field is therefore quantized. A numerical relation exists between the wavelength λ and the photon energy in keV:

$$\lambda [\text{\AA}] = \frac{hc}{E} = \frac{12.398}{E [\text{keV}]} \quad (4.4)$$

During inelastic scattering, there is an energy transfer from the incident X-ray photon to the electrons causing a reduction of the scattered photon energy (Compton shift). When only elastic scattering is considered, the energy transfer is neglected (Thompson scattering, Appendix B) and the scattering event can be described by a vector equation. Here, only elastic scattering is considered, therefore, it is possible to define the momentum transfer vector, the *scattering vector* \mathbf{Q} [\AA^{-1}], as:

$$\hbar\mathbf{Q} = \hbar\mathbf{k}' - \hbar\mathbf{k} \quad (4.5)$$

as the difference between the final momentum $\hbar\mathbf{k}'$ and the initial $\hbar\mathbf{k}$ (Figure 4.2).

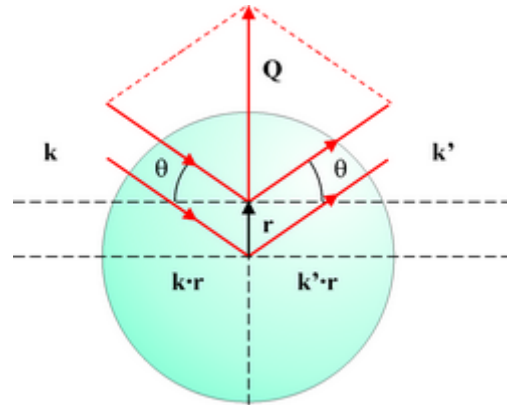


Figure 4.2: X-rays elastic scattering from an atom: classical description [118] The angles are considered with respect to the specimen surface.

In elastic scattering the length of the scattering vectors is given by $|\mathbf{k}| = |\mathbf{k}'| = 2\pi/\lambda$, and the difference in the phase of the scattered and incident wave is contained in the $\text{Im}(i\mathbf{Q} \cdot \mathbf{r})$ (Figure 4.2). Comparing the scattering amplitude of a free electron with the scattering amplitude from an atom, it follows that the amplitude of the wave scattered by an atom is the superposition of the amplitude of the scattered wave from an electron and the Fourier transform of the atom electron density $\rho(\mathbf{r})$, called the atomic scattering factor $f^0(\mathbf{Q})$. The strength of the scattered field will be the integral over the all contributions $-r_0\rho(\mathbf{r})d\mathbf{r}$ from the single volume $d\mathbf{r}$ at \mathbf{r} , with the phase $e^{i(\mathbf{Q} \cdot \mathbf{r})}$:

$$-r_0 \int \rho(\mathbf{r}) \cdot e^{i(\mathbf{Q} \cdot \mathbf{r})} d\mathbf{r} = -r_0 f^0(\mathbf{Q}) \quad \text{with} \quad \begin{array}{ll} \mathbf{Q} \rightarrow 0 & f^0(\mathbf{Q}=0) = Z \\ \mathbf{Q} \rightarrow \infty & f^0(\mathbf{Q} \rightarrow \infty) = 0 \end{array} \quad (4.6)$$

where r_0 is the *Thompson scattering length* equal to $2.82 \times 10^{-5} \text{\AA}$ representing X-rays interaction with a free electron in vacuum (see Appendix B). It will be $\mathbf{Q} \rightarrow 0$ when all the

atom electrons radiate in phase and $\mathbf{Q} \rightarrow \infty$ when the different volumes $d\mathbf{r}$ are scattering out of phase, destructive interference.

Atom electrons occupy different orbitals; there will be a different response from the different electron binding energy levels. Corrections to the atomic form factor must be introduced taking into account these effects that reduce the atomic scattering length: f' and f'' are known as dispersion corrections to f^0 . The importance of f' and f'' is directly proportional to the incident photon energy, reaching a maximum at the atom absorption edge energy.

Referring to Figure 4.1 and to equation (4.1), the scattering field will be described by:

$$F(\mathbf{Q}) = \sum_{\mathbf{R}_n} e^{i\mathbf{Q}\cdot\mathbf{R}_n} \sum_j f_j(\mathbf{Q}) e^{i\mathbf{Q}\cdot\mathbf{r}_j} \quad (4.7)$$

where the first term is the lattice sum $S_N(\mathbf{Q})$ and the last one represents the unit cell structure factor (neglecting the multiplicative factor $-r_0$).

The first term of equation (4.7) will be different from zero (contributions from the lattice to the scattered intensity) only in the case:

$$\mathbf{Q} \cdot \mathbf{R}_n = 2\pi \times N \quad (4.8)$$

with N an integer, the number of unit cells.

In the reciprocal space, a crystal is described in terms of its interplanar distance and its symmetry. It can be construct a reciprocal lattice as a set of imaginary points, arranged in a way that the direction of a vector from one point to another coincides with the normal of the corresponding real lattice planes. The length of a vector in the reciprocal space is proportional to the inverse of distance of the corresponding lattice planes d_{hkl} .

$$\mathbf{G} = \mathbf{d}_{hkl}^* = h\mathbf{a}_1^* + k\mathbf{a}_2^* + l\mathbf{a}_3^* \quad \text{where } d_{hkl} = \frac{1}{|\mathbf{d}_{hkl}^*|} \quad \text{and } V = (\mathbf{a}_1 \times \mathbf{a}_2) \cdot \mathbf{a}_3$$

$$\text{with } \left\{ \begin{array}{l} \mathbf{a}_1^* = (2\pi/V)(\mathbf{a}_2 \times \mathbf{a}_3) \\ \mathbf{a}_2^* = (2\pi/V)(\mathbf{a}_3 \times \mathbf{a}_1) \\ \mathbf{a}_3^* = (2\pi/V)(\mathbf{a}_1 \times \mathbf{a}_2) \end{array} \right\} \quad \text{and } \mathbf{a}_i \cdot \mathbf{a}_j^* = 2\pi \delta_{ij} \quad (4.9)$$

Any lattice position in the reciprocal space is defined by \mathbf{G} (4.9) and in the real space by \mathbf{R}_n (4.1), therefore it must be:

$$\mathbf{G} \cdot \mathbf{R}_n = 2\pi \times N \quad (4.10)$$

that is true only if $\mathbf{Q} = \mathbf{G}$: $F(\mathbf{Q})$ will not vanish only under the condition that \mathbf{Q} (the scattering vector) coincides with \mathbf{G} the reciprocal lattice vector. This is known as the *Laue condition* that underlines that strong scattering intensities I_{SC} from a crystal are points in the reciprocal space. The scattered intensity is given by:

$$I_{SC} \propto |S_N(\mathbf{Q})|^2 \propto N \cdot V_{SC}^* \cdot \delta(\mathbf{Q} - \mathbf{G}_{hkl}) \quad (4.11)$$

where $V_{SC}^* = (\mathbf{a}_1^* \times \mathbf{a}_2^*) \cdot \mathbf{a}_3^* = 1/V_{SC}$ is the scattering volume in the reciprocal space. X-ray detectors are collecting photons, are sensitive to intensity that is proportional to the square of the scattered energy and as a consequence to $|f(\mathbf{Q})|^2$. Therefore, the phase information is lost and it is not possible a direct reconstruction of the electron density function.

The *Bragg's law* is giving the condition for constructive interference of waves scattering with a lattice in the real space:

$$\lambda = 2d_{hkl} \sin \theta_B \quad (4.12)$$

where θ is the Bragg angle and d is the interplanar distance. The equivalence between the Bragg law and Laue condition (Appendix C) establishes a relation between the points in the reciprocal space and the planes in the real one: for each point in the reciprocal space corresponds a unique set of planes in the direct lattice fulfilling the conditions:

- \mathbf{G}_{hkl} is perpendicular to the plane (h,k,l)
- $|\mathbf{G}_{hkl}| = 2\pi/d_{hkl}$

4.2. X-ray scattering geometries

A very convenient way to represent X-ray scattering geometries makes use of the *Ewald sphere*, or *Ewald circle* in 2D, (Figure 4.3).

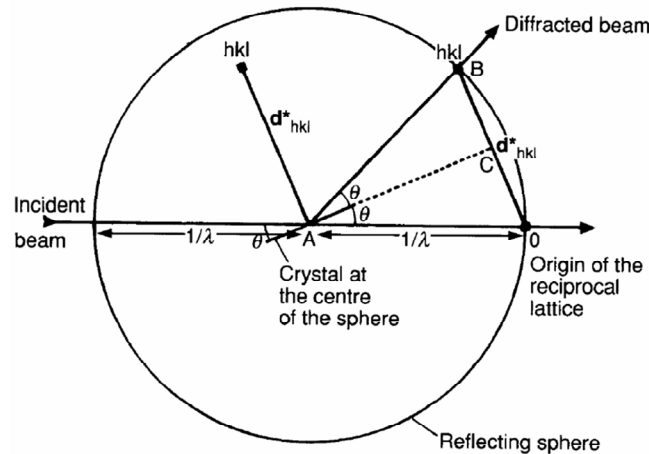


Figure 4.3: The Ewald circle where $\frac{1}{2} \mathbf{OB} = (1/\lambda) \sin \theta = \frac{1}{2} d_{hkl}^* = \frac{1}{2} (1/d_{hkl})$ [119].

This geometrical construction is build in a way that if one of the reciprocal lattice points lie on the circle then the Laue condition or the Bragg law are satisfied and a significant intensity is collected in the direction \mathbf{k}' (\mathbf{AB} in Figure 4.3).

In this study, co-planar (the incident and the diffracted vectors lie in the same plane perpendicular to the surface) X-ray scattering geometries are applied to investigate FePt layers. The non-coplanar geometry has been used for the *in-situ* GISAXS experiment for nanoclusters evolution during deposition, it will be described in paragraph 4.2.3. The coplanar geometry set-up is sketched in Figure 4.4.

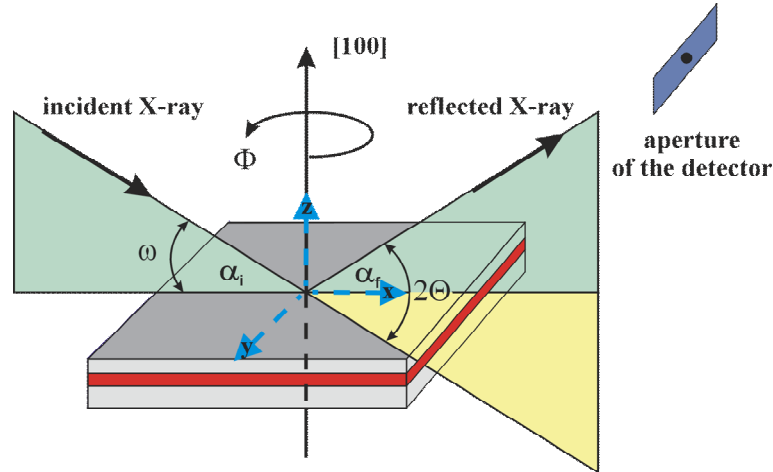


Figure 4.4: Co-planar X-ray scattering: the X-ray beam incidents the crystal planes with an angle ω and it is diffracted at 2θ [120].

It is useful to decompose the scattering vector components along x , y and z , putting the centre of the reference system in the scattering point (Figure 4.7):

$$\begin{aligned} Q_x &= \frac{2\pi}{\lambda} (\cos(2\theta - \omega) - \cos \omega) \\ Q_y &= 0, \text{ coplanar geometry} \\ Q_z &= \frac{2\pi}{\lambda} (\sin(2\theta - \omega) + \sin \omega) \end{aligned} \quad (4.13)$$

Combining the representation on the Ewald sphere and the reciprocal space lattice, X-ray scattering geometries can be simply represented. Symmetrical scans will be those in which the scattering vector \mathbf{Q} lies on the z axis ($Q_x = 0$), perpendicular to the sample surface with $\omega = 1/2(2\theta)$. Depending on the $|\mathbf{Q}|$ value, the X-ray analysis will be sensitive to different length scales in the change of the electron density.

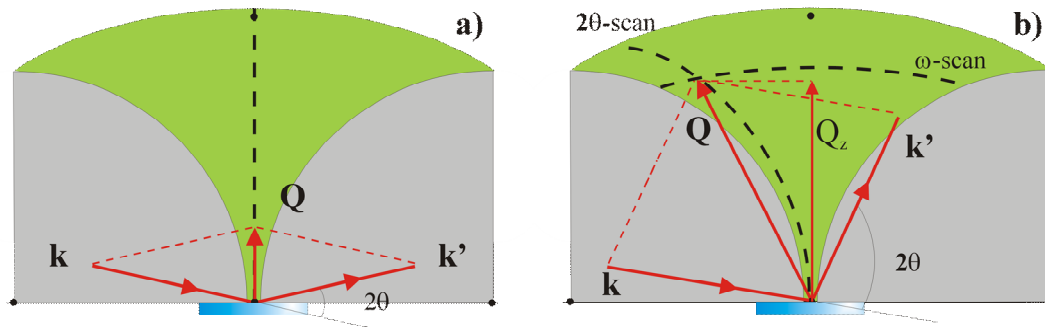


Figure 4.5: Scattering geometry representation in the reciprocal space, for small $|\mathbf{Q}|$ values [120]: a) symmetrical and b) asymmetrical scans. the grey area indicates zone not accessible in which the incident or the scattered beam is below the specimen.

At small $|\mathbf{Q}|$, only a global electron density change can be detected without any sensitivity to a modulation due to the atoms in the lattice, thus there is no possibility to distinguish between amorphous and crystalline materials (Figure 4.5). At large $|\mathbf{Q}|$, the reciprocal lattice points can be completely identified (Figure 4.6).

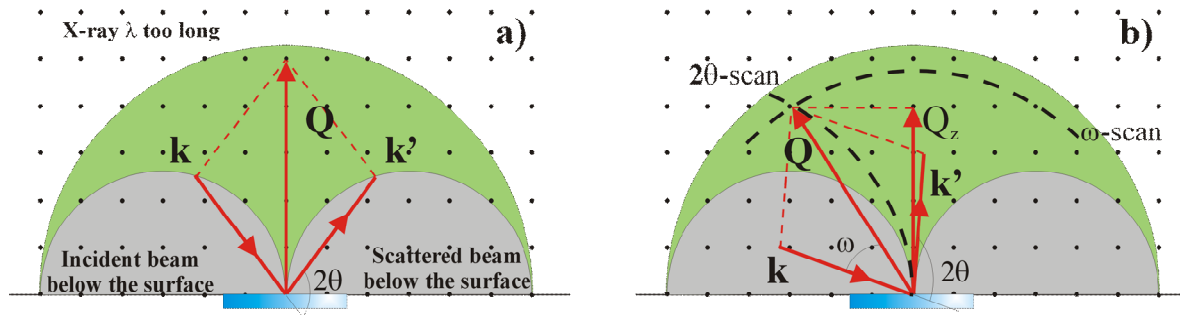


Figure 4.6: Scattering geometry representation in the reciprocal space, for large $|\mathbf{Q}|$ values [120]: a) symmetrical and b) asymmetrical scans.

Small $|\mathbf{Q}|$ values are characterizing the following scattering geometries (Figure 4.5):

- reflectivity measurements (XRR): symmetrical scans along Q_z (Figure 4.5-a), measuring the electron density distribution of the layer, suitable to measure film thickness and surface and interface layer roughness
- X-ray Diffuse Scattering (DS) (Figure 4.5-b): ω scans at a fixed exit angle, suitable to get information about the lateral interface structure of a thin film, but here we restrict our investigations of diffuse scattering patterns for the determination of the position of the critical angle for total external reflection α_c (paragraph 4.2.1)

With large $|\mathbf{Q}|$ values the X-ray scattering investigations are usually indicated with the term XRD (Figure 4.6):

- $\omega - 2\theta$ scans (Figure 4.6-a): a symmetrical scan, to detect crystallographic planes parallel to the layer surface
- Grazing Incidence X-ray diffraction (GIXRD) (Figure 4.6-b): 2θ scans at a fixed incident angle, with high sensitivity to the atomic arrangement of a surface, suitable for phase transition detection
- ω rocking curve (Figure 4.6-b): pattern collected at a fixed 2θ angle, varying the X-ray incident angle: in this way it can be evaluated, for instance, the angular dispersion of the planes in respect to the Bragg condition.

In this study X-ray investigations will be applied to characterise the structural properties of FePt layers.

4.2.1. X-ray reflectivity, absorption and diffuse scattering

In a pure kinematical approximation there is no absorption or refraction of X-rays, therefore some corrections must be considered in the treatment of XRR and DS data.

The refraction of an electromagnetic wave is following the Snell's law:

$$n_1 \cos \alpha_1 = n_2 \cos \alpha_2 \quad (4.14)$$

where n_1 and n_2 are the refractive indices of the air / vacuum (equal to the unit) and of the media, respectively; α_1 and α_2 the incident and refractive angle.

The X-ray refractive index is given by:

$$n = 1 + \frac{\chi_0}{2} = 1 - \delta + i\beta \quad (4.15)$$

$\delta \gg \beta$ and δ is of order of 10^{-5} . χ_0 is the first term of the Fourier transform of the polarizability (dielectric susceptibility) [121]:

$$\chi(\mathbf{r}) = \varepsilon_{rel} - 1 = -\frac{\lambda^2}{\pi} \cdot r_0 \cdot P \cdot \rho(\mathbf{r}) \quad (4.16)$$

ε_{rel} is the relative permittivity. $P = \sin \xi$ is the linear polarization coefficient (ξ is the angle between the polarisation vector and the position vector \mathbf{r} : $P = 1$ for S polarisation, where the polarisation vector of the incident and scattered beam are perpendicular to the scattering plane, for P polarisation $P = \sin(2\theta)$, with 2θ the scattering angle).

For whatever material $\delta = -\frac{1}{2}\text{Re}(\chi_0) < 1$ therefore $n < 1$. For incident angles minor than the critical one α_c , X-rays will be totally *externally* reflected by the media, with $n_1 = 1$, $\alpha_1 = \alpha_c$ and $\alpha_2 = 0$:

$$\alpha_c \approx \sqrt{2\delta} = \text{Re}(\sqrt{-\chi_0}) = \lambda \sqrt{\frac{r_0}{\pi} \langle \rho(\mathbf{r}) \rangle} \in \mathbf{R} \quad (4.17)$$

with $\beta = 0$, α_c is in the order of milliradians. The critical angle is not sensitive to the electron arrangement and crystal structure but depends only from the mean media electron density.

X-ray waves are absorbed by a media: the intensity of the wave will decrease of a factor $e^{-\mu r}$ while traversing a thickness r , where μ is the linear absorption coefficient.

The absorption coefficient is directly related to the material characteristics:

$$\mu = \frac{\rho_m N_A}{M_A} \sigma_a \quad (4.18)$$

where ρ_m is the mass density and σ_a is the X-ray energy dependent absorption cross section. An absorbed energy can generate fluorescence or electron emission (spectroscopy investigations). The absorption dependence is included in the imaginary part of the refractive index: $\beta k = \mu/2$. Considering the atomic scattering factor, including dispersion $f(\mathbf{Q}) = f^0(\mathbf{Q}) + f' + if''$ and because of a e^{inkr} X-ray absorption dependency in the media (where nk is the modulus of the wavevector in a media), it can be obtained:

$$n \equiv 1 - \frac{2\pi \cdot \rho_a \cdot r_0}{k^2} \{f^0(0) + f' + if''\} \quad (4.19)$$

An expression of the real and imaginary part of the refractive index n is, in a dynamical theory approach using the matrix formalism [122]:

$$\delta = \frac{N_A}{2\pi} r_0 \lambda^2 \sum_k \frac{\rho_k}{A_k} (f_k^0 + f'_k) \quad \text{and} \quad \beta = \frac{N_A}{2\pi} r_0 \lambda^2 \sum_k \frac{\rho_k}{A_k} f''_k \quad (4.20)$$

From the Snell's law (4.14) and considering an infinite free surface irradiated by a plane wave:

$$A_i \exp(i\mathbf{k}_i \cdot \mathbf{r}) \quad (4.21)$$

the continuity at the interface between the media and vacuum requires that the x component of the transmitted wave vector be equal to the x component of the incident one. The expressions for the Fresnel's *amplitude reflectivity* r and *transmittivity* t can be derived:

$$r \equiv \frac{A_R}{A_I} = \frac{k_{i,z} - k_{T,z}}{k_{i,z} + k_{T,z}} \quad \text{and} \quad t \equiv \frac{A_T}{A_I} = \frac{2k_{i,z}}{k_{i,z} + k_{T,z}} \quad (4.22)$$

The relations for the *intensity* R and T are the modulus square of r and t .

In a material the scattering vector \mathbf{Q} is a complex number, therefore α_c will be a complex number $\alpha_c^* = \sqrt{-\chi_0}$ whose real part is given in equation (4.17). The transmitted wave decreases its amplitude with depth $A_T e^{iQ_z^* z} = A_T e^{i\text{Re}(Q_z^*)z} e^{-\text{Im}(Q_z^*)z}$ where $Q_z^* = (2\pi/\lambda) \left[\sqrt{\sin^2 \alpha_i - \sin^2 \alpha_c^*} + \sqrt{\sin^2 \alpha_f - \sin^2 \alpha_c^*} \right]$. The penetration depth Λ is defined by the thickness at which the intensity drops of $1/e$ and the given by:

$$\Lambda = \frac{1}{|\text{Im}(Q_z^*)|} \quad (4.23)$$

In Figure 4.7 an example of reflectivity measurements of FePt layers deposited on a -SiO₂/Si(100) is reported at incident angles $\alpha_i \leq 4^\circ$, recorded from a synchrotron source at ROBL [115] at 8 keV.

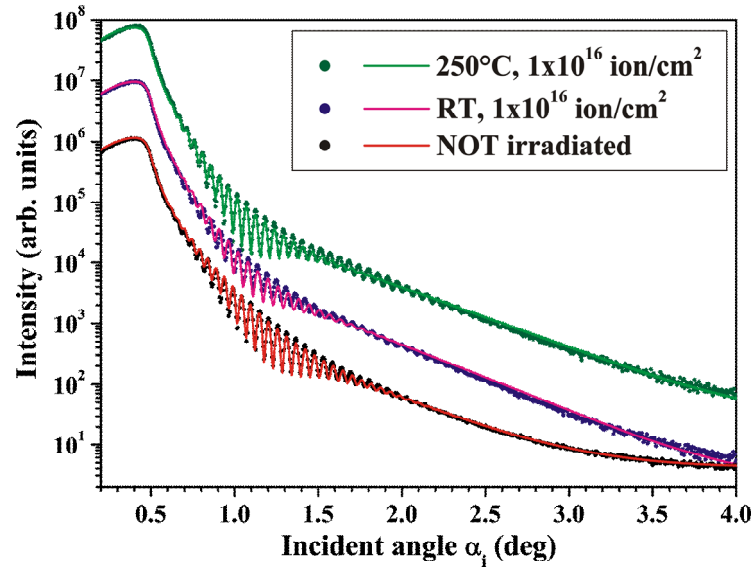


Figure 4.7: XRR measurement of FePt layer on $a\text{-SiO}_2 / \text{Si}(100)$, before and after He^+ irradiation.

In the reflectivity curve it is possible to observe the presence of interference maxima, as a consequence of the interference between the beam reflected from the upper and from the lower part of the layer.

From equation (4.22) it is possible to derive the expression for the reflectivity R for a single layer, of thickness Δ , deposited on an infinite substrate (Figure 4.8):

$$R = \left| \frac{r_1 + r_2 e^{-2ik_{Tz}\Delta}}{1 + r_1 r_2 e^{-2ik_{Tz}\Delta}} \right|^2 \quad (4.24)$$

where $r_{1,2}$ are the Fresnel reflectivity coefficients of the free surface and the substrate interface, respectively. k_{Tz} is the z component of the wave vector in the layer 1 equal to nk_{iz} .

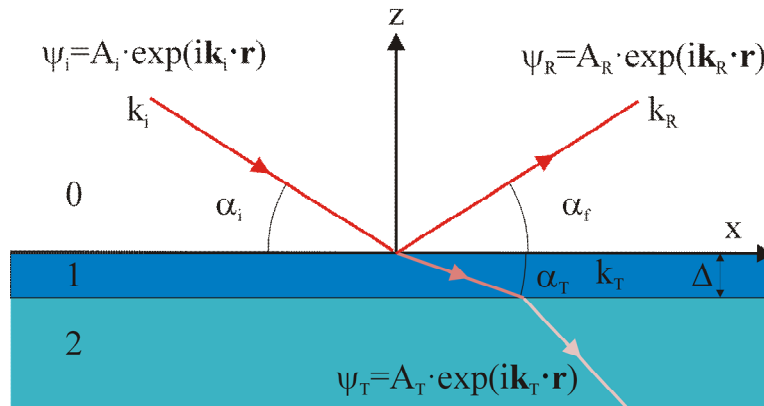


Figure 4.8: Refraction from a single layer of finite thickness Δ : side view [118].

Therefore, there will be a maxima every time $e^{-2ik_{Tz}\Delta} = 1$, obtained for the incident angle position α_{iM} :

$$\Delta = \frac{m\lambda}{2\sqrt{\sin^2 \alpha_{iM} - \sin^2 \alpha_c}} \sim \frac{m\lambda}{2\sqrt{\alpha_{iM}^2 - \alpha_c^2}} \quad \text{for small angles} \quad (4.25)$$

that gives an easy tools to measure the layer thickness, with a relation that is the Bragg law taking into account refraction. The thickness oscillations are called *Kiessing* fringes.

For $\alpha_i \leq \alpha_c$, there is an intensity increase due to set-up characteristics and sample finite size, the *illumination correction*: for very small incident angles the beam projection A_{beam} can be larger than the sample size A_{sample} , therefore the measured intensity I_{meas} will be proportional to the incident angle and has to be corrected:

$$I = I_{meas} \sin(\alpha_i) \quad \text{for} \quad \frac{A_{sample}}{A_{beam}} < 1$$

$$I = I_{meas} \quad \text{for} \quad \frac{A_{sample}}{A_{beam}} \geq 1$$
(4.26)

The finite size of the sample is also affecting the determination of the critical angle and, as a consequence, of the layer density, as:

$$\frac{\Delta\rho_{el}}{\rho_{el}} = 2 \frac{d\alpha_i}{\alpha_c}$$
(4.27)

where $d\alpha_i$ is the measurement goniometer step width.

For $\alpha_i > \alpha_c$ the intensity is decreasing $\propto \alpha_i^{-4}$ (or $\propto Q_z^{-4}$), oscillating because of the beam reflected from the lower and upper part of the layer. In Figure 4.7 it is shown how the XRR investigations can be applied to analyze layers structure before and after irradiation. From the evident similarity of the three curves it comes clear that there was no damage of the film structure because of irradiation. It is possible to recognize oscillation fringes with high frequency due to the layer thickness of 70 nm associated with low frequency beats caused by a top layer with reduced density ($\sim 60\%$ of the bulk value) and thickness between 1 and 3 nm in the case of the irradiation at 250°C.

The accuracy on thickness measurements depends on the measurement step width:

$$\frac{d\Delta}{\Delta} = \frac{d\alpha_i}{\alpha_i} \approx \frac{\alpha_i}{m}$$
(4.28)

where m is the number of detectable maxima inside the measurement range.

In this study, the experimental data have been simulated by the program RC_REF_SIM_Win [122], where the values of δ and β are defined by the user and then elaborated on the basis of the dynamical theory, taking into account multiple reflections, to solve equation (4.24) using the matrix approach.

The Fresnel equations describe a specular reflectivity, in which roughness is not taken into account. Surface (or interface) roughness will scatter the X-ray wave locally into different directions producing the so called *diffuse scattering* that leads to a dump for $\alpha_i \gg \alpha_c$

different than $(Q_z)^{-4}$. Névot and Croce [123, 124] had suggested a modification of the reflection and transmission coefficients, for roughness with low correlation length:

$$r = r_{Fresnel} \cdot e^{-2k_z k'_z \sigma^2} \quad \text{and} \quad t = t_{Fresnel} \cdot e^{(k_z - k'_z)^2 \sigma^2 / 2} \quad (4.29)$$

and for a random one, a Debye-Weller-like factor can be used:

$$r = r_{Fresnel} \cdot e^{-2k_z^2 \sigma^2} \quad (4.30)$$

where σ is the surface roughness in rms. The Névot and Croce approximation is the model implemented in the analysis program RC_REF_SIM_Win [122] to simulate surface and interface roughness.

These methodologies describe the vertical roughness component but give no information about the lateral one. At this purpose X-ray analysis at small $|\mathbf{Q}|$ value, around the specular beam, are suitable (Figure 4.9). The roughness can be described by a statistical model, with r in the plane parallel to the surface:

$$g(r) = 2\sigma^2 \left[1 - e^{-(r/\xi)^2} \right] \quad (4.31)$$

h is the *fractal exponent* ($0 < h < 1$). The cutoff length ξ (usually called *correlation length*) has been introduced to define the boundary conditions of the self-affine behavior described by $g(r)$: at an atomistic scale, for $r \rightarrow 0$, $g(r) \propto r^{2h}$; for $r \rightarrow \infty$, $g(r) \approx 2\sigma^2$ giving the average rms roughness. $C(r) = \sigma^2 e^{-(r/\xi)^2}$ is the *height-height* correlation function:

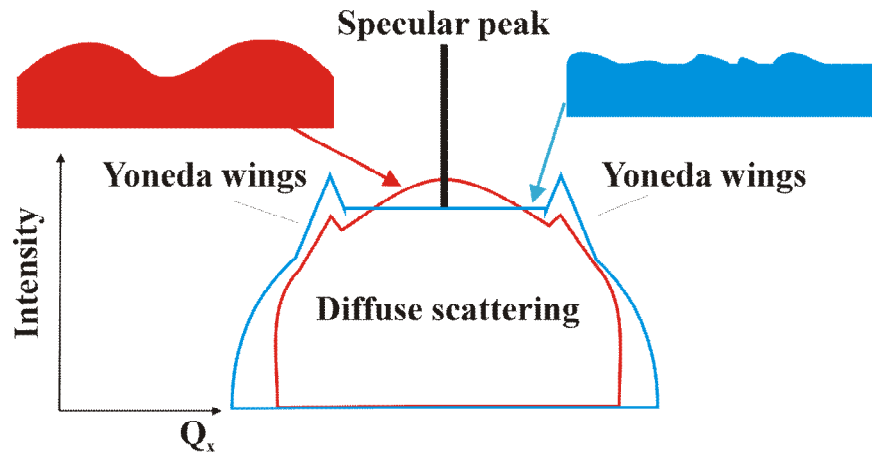


Figure 4.9: Sketch of the diffuse scattering: high correlation length (red lines), random roughness (blue lines) [124].

The correlation length ξ determines the shape of the diffuse scattering: smaller is ξ larger is the Gaussian component superimposed at the Lorentzian from the specular beam (Figure 4.9).

For $\alpha_i = \alpha_c$, the transmittivity will take the value of 2 in amplitude, equation (4.22), and cause a strong enhancement of the diffuse intensity (for the incident and exit angles) leading to the *Yoneda Wings* [125]. The position of the Yoneda wings will be used to determine the α_c position in this thesis.

4.2.2. X-ray diffraction

Here are described those experiment in which the $|\mathbf{Q}|$ value is large enough to be sensitive to electron density modulation and to the atom arrangement inside the unit cell (Figure 4.6). During an X-ray diffraction experiment the integrated intensity from a Bragg peak will be collected by a detector, equation (4.11). It is possible to calculate, more precisely, the differential cross section, the number of scattered photons in 1 s, normalized over the incident flux, in $d\Omega$:

$$\left(\frac{d\sigma}{d\Omega}\right) = r_0^2 P |F(\mathbf{Q})|^2 N \cdot V_{sc}^* \cdot \delta(\mathbf{Q} - \mathbf{G}) \quad (4.32)$$

where P is the polarization factor (appendix B). $(d\sigma/d\Omega)$ results to be direct proportional to the number of scattering centres but to the inverse of the scattering volume. Therefore, the intensity at the detector will be anyhow intense and sharp also in the case in which the Laue conditions are only closely satisfied, generating a peak of finite width. To have the full information about the peak shape, is necessary to perform an integration along \mathbf{k}' and ω . This will lead to the introduction of correction terms (the Lorentz factor) to the final form of I_{SC} , where Φ_0 is the incident photons flux on the unit area [118]:

$$I_{SC} = \Phi_0 \cdot r_0^2 \cdot P \cdot |F(\mathbf{Q})|^2 \cdot N \cdot \frac{\lambda^3}{V_{sc}} \cdot \frac{1}{\sin 2\theta} \quad (4.33)$$

N represents the number of scattering centres, connecting the scattering intensity I_{SC} with the specimen degree of crystallinity. This form of the scattered intensity (equation 4.33) is valid for almost perfect crystals with perfectly aligned lattice planes. In a real case, a crystal could be composed by small perfect blocks with an orientation distribution around some average value to form a mosaic structure (figure 4.10). This will cause a spread of the signal collected in a ω -scan along Q_x around the Laue conditions $\mathbf{Q} = \mathbf{G}$. It is, therefore, possible to evaluate the crystal mosaicity by analysing the shape of a reflection collected around $\mathbf{Q} = \mathbf{G}$ over an angular range large enough to capture the entire mosaic fan.

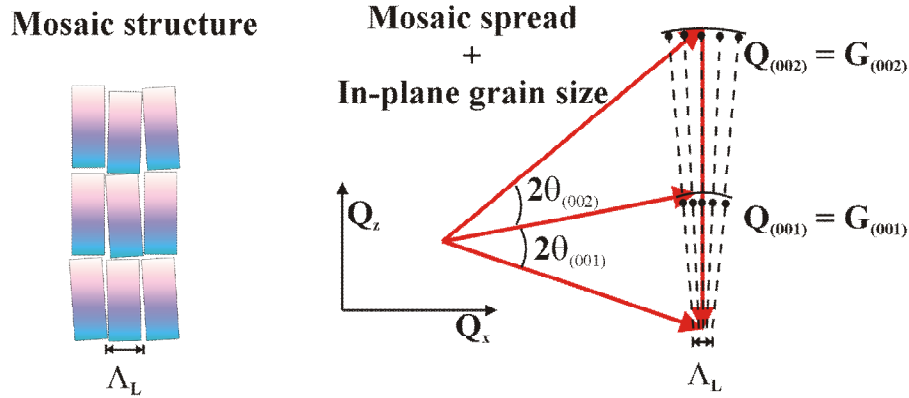


Figure 4.10: Sketch of a mosaic structure and of the in-plane grain size. Their effect on the FWHM of the (001) and (002) reflection is shown on the left side [118].

Considering equation (4.33), when the crystals are very small, N becomes small causing a broadening of the peak width: the peak breadth can be expressed in term of crystallite size. The first treatment of peak broadening due to crystallite size is due to Scherrer [126, 21, 127]. The crystals are assumed to be free from faulting or strains, so that the peak FWHM is due only to crystallite size $\Lambda = N \cdot a$ (a is the unit cell size, figure 4.1):

$$FWHM(2\theta) = \frac{0.94 \cdot \lambda}{\Lambda \cos \theta} \quad (4.34)$$

The numerical factor 0.94 is connected to the Gaussian approximation done in considering the peak shape [21]. The Scherrer formula was derived for cubic systems but it can be generalized as an approximation of the average crystal size, perpendicular to the reflecting planes, also for not cubic lattices. Unfortunately, several are the effects that cause a wider broadening of the peak FWHM, such as slit widths, sample size, X-ray penetration, imperfect focusing, unresolved α_1 and α_2 peaks. All these source of broadening are usually called “instrumental broadening”. To correct the instrumental broadening is necessary to analyse a standard in the exactly identical conditions applied to investigate the unknown sample. The standard must be of the same “nature” of the specimen but having grains large enough to eliminate the particle-size contribution to the peak shape. Indicating with $h(x)$ the experimental curve from the sample under investigation, $f(y)$ the curve obtained considering only the particle-size contribution and $g(z)$ the instrumental contribution, $h(x)$ can be obtained by solving the convolution integral [21]:

$$h(x) = \frac{1}{A} \int g(z) f(x-z) dz \quad (4.35)$$

where A is the area underneath the $f(y)$ curve. The procedure to solve the integral of equation (4.36) imply the choice of a model to describe the three curves involved, such as Gaussian or Cauchy shape, but this is hardly applicable to real cases in which the curves are never “pure Gaussian” and vary with the sample. Moreover, the identification and production of a reliable standard is quite difficult. For all these reasons, this procedure for

error correction to the grain size determination, via Scherrer formula, was not applied in this study, preferring to consider the particle size, here calculate, not as an absolute value but as a useful comparing scale of the layer structure.

Most of the X-ray scattering investigations applied in this study are performed with the same diffractometer (paragraph 4.2.4) and under the same resolution set-up; therefore, it will not be taken into account the instrumental resolution function considering the integral area of the diffraction peak as a direct indicator of the degree of crystallinity of the layer.

In real X-ray diffraction experiments, the effect of mosaicity and the in-plane grain size dimensions will both contribute to the shape of the reflection collected by ω -scans along Q_x (Figure 4.10). To solve this problem it is necessary to evaluate the FWHM of at least two peaks, for example the (001) and the (002), to obtain a reliable information about degree of mosaicity of the layers.

In this work all X-ray diffraction patterns were analysed with the help of the commercial software PeakFit™ [128] using a Voigt function [129] to model the reflections.

4.2.3. Grazing Incidence Small Angle X-ray Scattering

In the last decade Grazing Incidence Small Angle X-ray Scattering (GISAXS) has become an important tool to investigate surface and near surface morphology [130]. One of the major applications is the analysis of nanocluster shape and size. In this work the experiment is performed to investigate *in-situ* the morphological evolution of the Ag/FePt agglomerates on *a*-SiO₂ (paragraph 7.2). A drawing of the set-up is shown in figure 4.11.

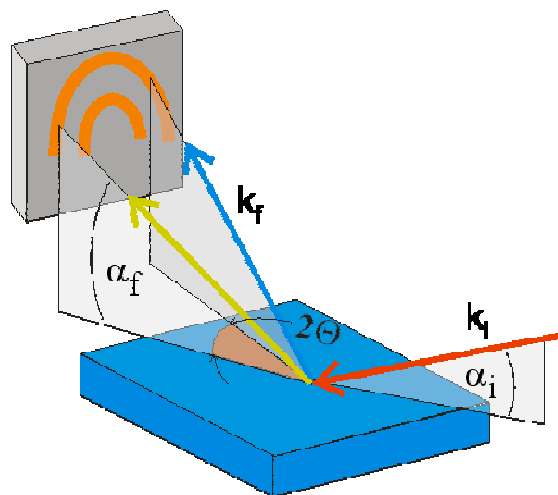


Figure 4.11: GISAXS set-up [120].

GISAXS measurements are done in non coplanar geometry: the components of the scattering vector along x , y and z must be computed.

$$\begin{aligned}
Q_x &= \frac{2\pi}{\lambda} (\cos \alpha_f \cos \theta_f - \cos \alpha_i \cos \theta_i) \\
Q_y &= \frac{2\pi}{\lambda} (\cos \alpha_f \sin \theta_f + \cos \alpha_i \sin \theta_i) \\
Q_z &= \frac{2\pi}{\lambda} (\sin \alpha_f + \sin \alpha_i)
\end{aligned} \tag{4.36}$$

The investigations must be carried out at incidence angle close to the critical one [131] in a way that the evanescent beam is confined on top of the layer enhancing the surface sensitivity. In this case, the substrate is acting as a mirror and multiple scattering must be taken into account. To do that the scattering process must be described by the Distorted-Wave Born Approximation (DWBA) in which a perturbation is introduced in term of roughness caused by the sample surface/near surface morphology. The incident wave scattering inside the sample is described by the dynamical theory, the subsequent diffuse scattering, caused by the perturbation, is treated in a kinematical approximation. The last step, the wave travel towards the surface, is again described dynamically [124]. Therefore, the solutions will be 5 different waves:

- the incident X-ray vacuum plane wave
- the specularly reflected vacuum plane wave
- the diffracted vacuum plane wave
- the transmitted wave inside the crystal
- the diffracted wave inside the crystal

The complexity of the approximation depends on how many scattering channels are taken into account [124].

In many cases the position of the GISAXS intensity maxima can be taken as an average measurement of the interisland distance D :

$$D = \frac{2\pi}{Q_{Max}}. \tag{4.37}$$

The angle formed between the Q_z axes and the line linking the GISAXS maxima with the origin of the (Q_y, Q_z) system, gives the facet angle respect the substrate surface [132].

4.2.4. X-ray scattering: experimental set-up

All *ex-situ* X-ray scattering investigations were performed on the Siemens/Bruker AXS D5005 diffractometer, equipped with the software SPEC [133] for data acquisition and diffractometer motor control. A sketch of the set-up is shown in figure 4.12.

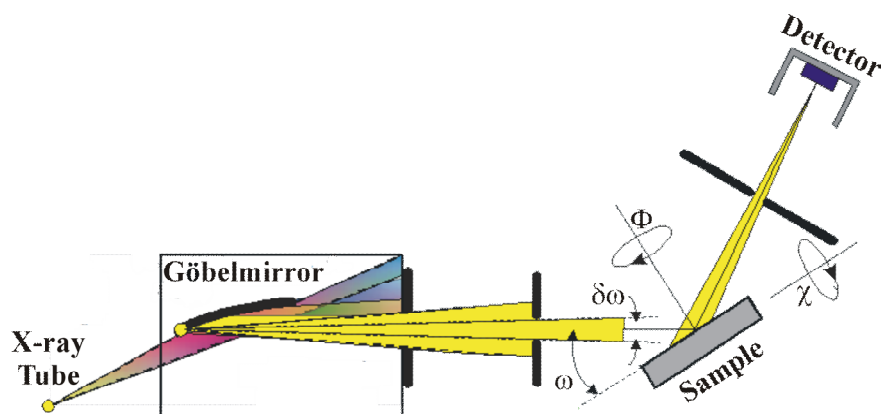


Figure 4.12: Sketch of the set-up of the diffractometer D5005 [120].

The X-rays are generated by a sealed, water cooled, X-ray tube with a Cu anode operating at an electric input at 40 V and 40 mA. This is a fine-focus tube delivering a line focus of about $0.05 \times 10 \text{ mm}^2$. Subsequently the beam is reflected by a Göbel mirror [134], a parabolic bent multilayer mirror, suppressing the $K\beta$ line and transforming the divergent beam from the X-ray tube to a rather parallel one. The beam angular divergence at the sample is below 0.01° . The X-ray tube and the Göbel mirror delivers an X-ray intensity up to $\sim 10^8$ cps on the primary beam with a $(\Delta\lambda/\lambda) \approx 10^{-2}$, but still $K\alpha_1$ and $K\alpha_2$ are present in the spectrum. The diffractometer is equipped with a four-circle goniometer allowing sample movements in ω , Φ the azimuth angle and χ (by the $\frac{1}{2}$ circle Eulerian cradle [135]). The diffracted beam is collected by a point detector. The final angular resolution was achieved by a set of slits in front of the detector aperture. For XRR or DS the angular resolution was $(\Delta 2\theta) \approx 0.06^\circ$, for GIXRD geometry $(\Delta 2\theta) \approx 0.12^\circ$ and for the $\omega - 2\theta$ $(\Delta 2\theta) \approx 0.09^\circ$.

All *in-situ* X-ray scattering investigations were performed in the Material Research Hutch (MRH) at the The Rossendorf Collaborating Research Group beamline (ROBL-CRG) at bending magnet BM20 at the ESRF. It uses horizontally a fan of 2.8 mrad of synchrotron radiation from a bending magnet hard edge and has been designed for performing experiments on two different alternatively running experimental stations [136]. The layout of the optics is shown in Figure 4.13. The basic elements are a fixed-exit double crystal Si(111) monochromator located between two mirrors with Si and Pt surface coatings, respectively. The double-crystal monochromator (DCM), from Oxford Instruments, ATG, provides a fixed-exit beam with a vertical offset of 18 mm, allowing energy up to 25 keV

with an energy resolution $\sim 2 \times 10^{-4}$. The lower energy limit is given essentially by the Be-windows. The integrated flux is 6×10^{11} phot/s at 20 keV/200 mA.

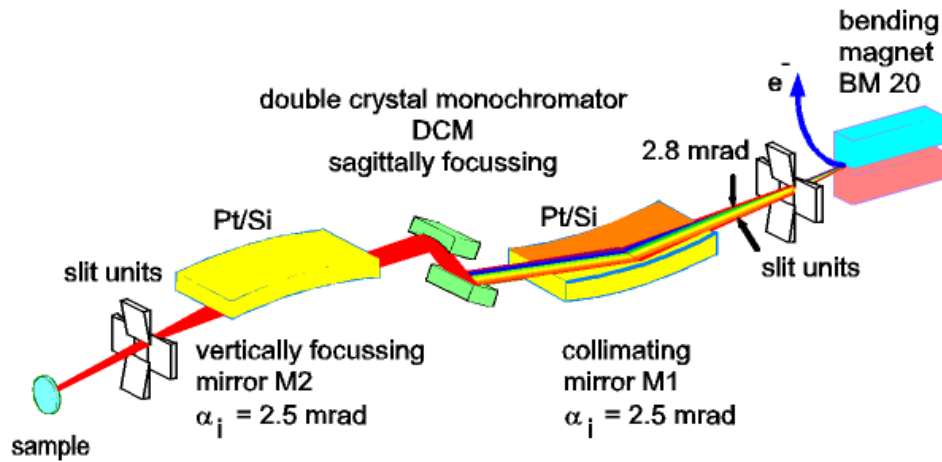


Figure 4.13: Schematic layout of the ROBL optics [137]

The two mirrors suppress the higher-order harmonics in the monochromatic beam, reduce the heat load on the monochromator and provide a parallel or vertically focused beam at the experimental stations. The final vertical divergence of the X-ray beam is below 0.5 mrad. The slit units have independently moveable blades (tungsten carbide), with accuracy better than $10 \mu\text{m}$. The motions of nearly all optical components are controlled by a UNIX workstation-based system.

The six-circle diffractometer is the main equipment of the MRH, built from modular components (Huber) (Figure 4.14) [138].

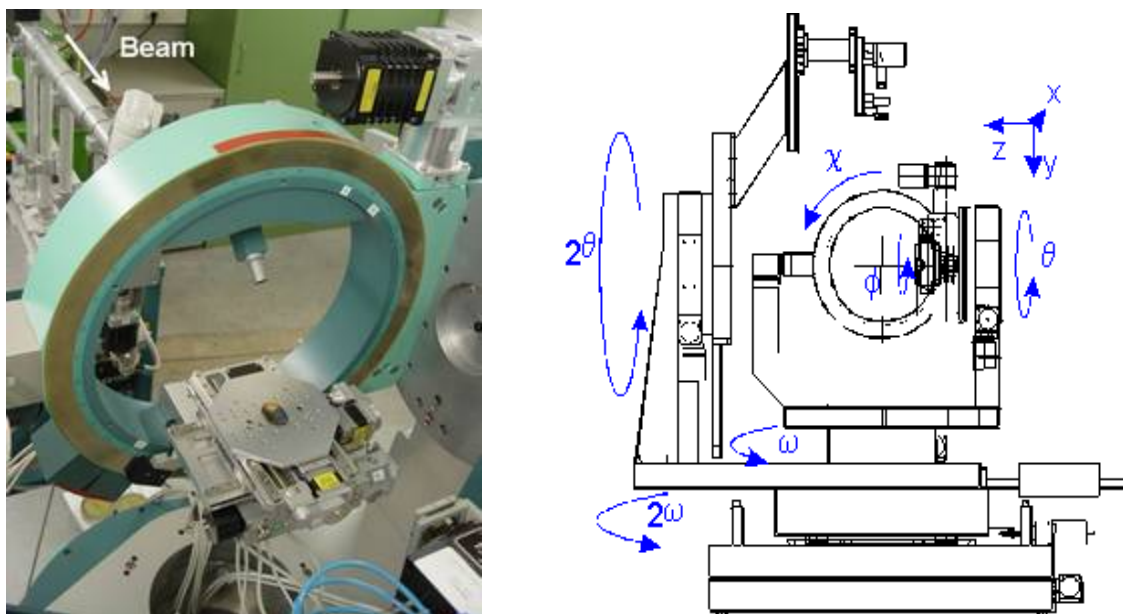


Figure 4.14: Six-circle diffractometer in the MRH of ROBL; (left side) view of the χ -circle (Eulerian cradle with inner diameter of 400 mm) with the x - y - z slide mounted directly on the azimuth ϕ -circle (front view: detector side), (right side) scheme of the diffractometer with identification of the axes (view from back: beam direction).

The sample position can be equipped with an x - y - z slide or, alternatively, with special sample environment chambers which are mounted directly on the Φ -circle (inner diameter 80 mm). The layout is designed for a load up to 15 kg at the sample position and the χ -circle has an inner diameter of 400 mm so that relatively big chambers (e.g. a high-temperature chamber, sputtering chamber) can be used. All axes have an angular resolution of 0.001° . The goniometer control and data acquisition is performed with SPEC [133]. The detector used in these experiments is a high-load high-linearity scintillation detector (Bede ERD). The intensity of the incident beam for each acquisition point is monitored by a similar detector. In the experiments, here described, the incident beam size was kept at $(0.2\text{-}0.4 \times 4\text{-}6) \text{ mm}^2$ (H \times V). In front of the detector (at 57 cm from the goniometer rotation centre), interchangeable fixed single or Soller slits, to reduce axial divergence of the diffracted X-ray beam, can be mounted to achieve different angular resolutions according to the investigation performed. In this study a horizontal slit of 0.2 mm (angular resolution 0.02°) was mounted for XRR and DS measurements, for GIXRD a Soller slit with horizontal aperture of 0.4 mm and for $\omega - 2\theta$ geometry a 0.4 mm slit giving an angular resolution of 0.04° was used.

4.3. Additional methods of analysis

4.3.1. Rutherford backscattering spectroscopy (RBS)

Layer thickness and composition can be obtained by the evaluation of the RBS data. The film is irradiated with 1.7 MeV $^4\text{He}^+$, produced by a Van der Graaff accelerator. The backscattered ions are collected by an energy sensitive Si detector, positioned at the backscattering angle of 170° . Incidence angles, measured from the surface normal, up to 70° can be used to increase surface sensitivity for thin layers. All the spectra were collected in random mode. A sketch of the set-up is shown in Figure 4.15.

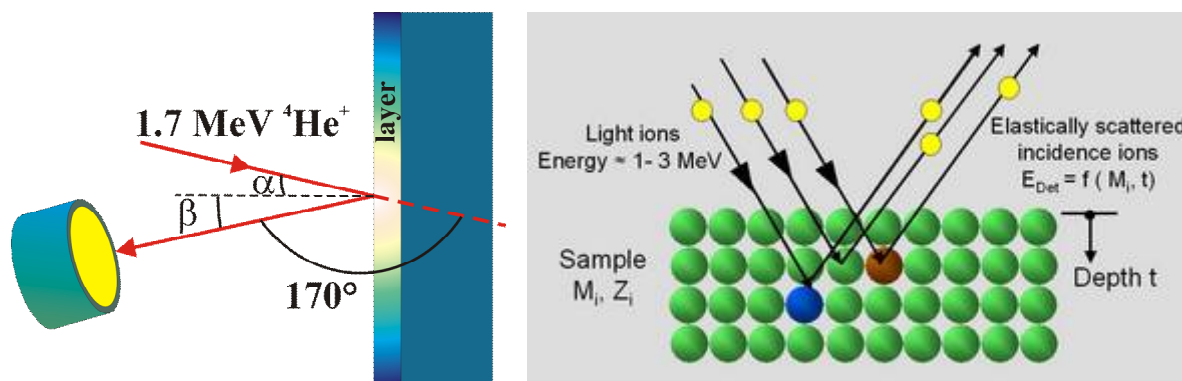


Figure 4.15: RBS set-up (left). Schema of the ion beam interaction with the layer (right) [87].

The main features of RBS analysis are related to the facts that the energy of the elastically backscattered particles is proportional to the target atom mass (kinematic factor) and to the

depth at which the scattering takes place. The element analysis is performed evaluating the kinematic factor k [139]:

$$k = \frac{E_{B,0}}{E_{i,0}} = \left(\frac{\sqrt{m_T^2 - m_i^2 \sin^2 \theta} + m_i \cos \theta}{(m_i + m_T)} \right)^2 \quad (4.38)$$

where $E_{i,0}$ is energy of the incident ion just before collision, $E_{B,0}$ the backscattered energy just after collision in the specimen and θ the scattering angle in the laboratory system.

The elemental depth profiles derived from RBS data are a consequence of the electronic stopping. This determines an additional energy loss of the incident and scattered ion because of passing through the film. The ion energy collected by the detector will be the sum of different energy losses:

$$E_{Det} = E_i - \Delta E_{in} - \Delta E_{coll} - \Delta E_{out} \quad (4.39)$$

where E_i is the incident ion energy. The second and the fourth term of equation (4.39) are the energy losses by the ion travelling Δz inside the layer, before and after collision, by (inelastic) electronic stopping and it can be estimated by [140]:

$$\Delta E_{in} = E_i - E_{i,0} = S_e^{in} \cdot (\Delta z / \cos \alpha), \quad \Delta E_{out} = S_e^{out} \cdot (\Delta z / \cos \beta) \quad (4.40)$$

The energy loss for elastic collision with a target atom is:

$$\Delta E_{coll} = (1 - k) \cdot E_{i,0} \quad (4.41)$$

Therefore the backscattered ion energy will be:

$$E_{Det} = k E_i - \left[k \cdot \frac{S_e^{in}}{\cos \alpha} + \frac{S_e^{out}}{\cos \beta} \right] \cdot \Delta z \quad (4.42)$$

S_e^{in} and S_e^{out} are the electronic stopping powers, supposed to be constant along z in thin layers. Thus, as pointed out in equation (4.42), a quasi linear relationship exists between the measured energy E_{Det} and the depth z at which the scattering takes place.

The integrated backscattering yield Y will be [141]:

$$Y = \frac{N_i}{\cos \alpha} \frac{d\sigma}{d\Omega} \Delta\Omega N_{AD} \quad (4.43)$$

where N_i is the number of incident ions, $\Delta\Omega$ is the detector solid angle and N_{AD} is the layer areal density. The differential Rutherford scattering cross section is [139]:

$$\frac{d\sigma}{d\Omega} = \left(\frac{Z_i Z_T e^2}{8\pi\epsilon_0 E_{i,0}} \right)^2 \frac{\left[\sqrt{m_T^2 - m_i^2 \sin^2 \theta} + m_T \cos \theta \right]^2}{m_T \sin^4 \theta \sqrt{m_T^2 - m_i^2 \sin^2 \theta}} \quad (4.44)$$

which approximates, for $\theta \rightarrow \pi$, to:

$$\frac{d\sigma}{d\Omega} \approx \left(\frac{Z_i Z_T e^2}{8\pi\epsilon_0} \right)^2 \frac{1}{E_{i,0}^2} \frac{1}{\sin^4(\theta/2)}. \quad (4.45)$$

Because $d\sigma/d\Omega$ is proportional to Z_T^2 , the RBS technique is sensitive to the detection of heavy elements on light substrate (accuracy < 5%). By using the integrated backscattering yield of the corresponding peak in the RBS spectrum, it is possible to determine the film thickness Δ , supposing an appropriate value for the layer atomic concentration:

$$\Delta = \frac{N_{AD}}{n} = \frac{Y \cdot \cos \alpha}{(d\sigma/d\Omega) \cdot Ni \cdot \Delta\Omega} \cdot \frac{1}{n}. \quad (4.46)$$

The RBS experimental data were analysed with the program RUMP [142] to obtain the deposition rate (in $\text{at}/\text{cm}^2 \text{ s}$) and the layer stoichiometry. RBS thickness results were evaluated considering a Fe density of $8.48 \times 10^{22} \text{ at}/\text{cm}^3$ and Pt $6.62 \times 10^{22} \text{ at}/\text{cm}^3$ [142] (bulk densities). Comparing the RBS thickness values with those obtained from the XRR investigations it is possible to compute density variations with respect to the bulk.

4.3.2. Scanning Electron Microscopy (SEM)

FePt film surface morphology was investigated by the ultra-high resolution Hitachi Field-Emission-SEM S-4800. A sketch of the microscope is shown in Figure 4.16.

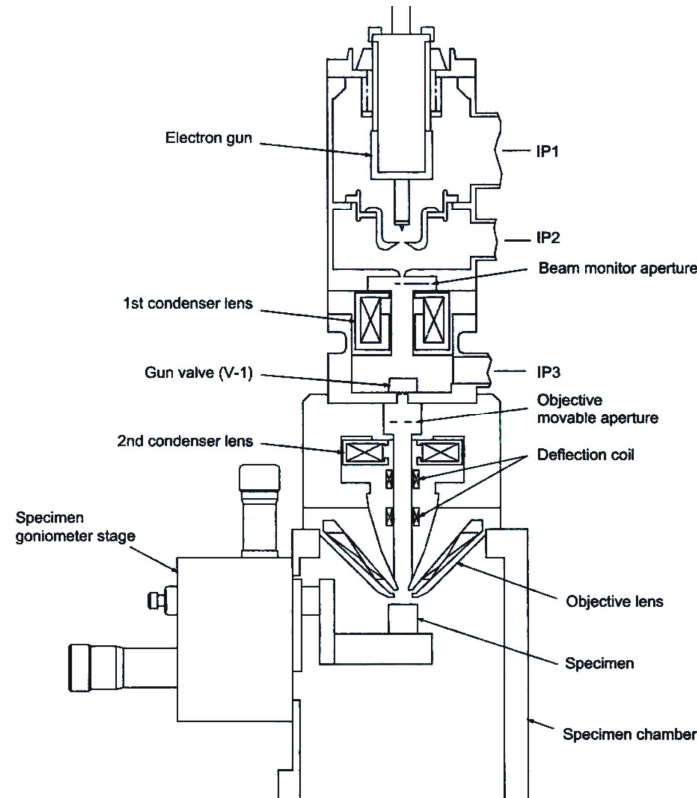


Figure 4.16: Scheme of SEM Hitachi S-4800 [143].

The electron beam ($E = 0.5 \div 30$ keV) is produced by an electron gun equipped with a cold cathode emitter. Subsequently, a set of magnetic lenses focalise the beam spot. Near the bottom, a set of deflection coils moves the focused beam. The final objective lens, focus the electrons beam to the sample surface with a typical spot size of 1 – 5 nm, depending on magnification, energy and current. As the electron beam hits the sample, signals are emitted because of the interactions of the electron beam with atoms at or near the surface of the specimen. The types of signals produced by an SEM include secondary electrons (SE), back-scattered electrons (BSE) and characteristic X-rays. SE are mainly used to build up topographical images with a well-defined, three-dimensional appearance of the specimen surface. The BSE yield strongly depends on the atomic number and provide image contrast according to the elemental distribution at the sample surface. The S-4800 is equipped with an SE and BSE detector and a microanalysis system INCA (Oxford Instruments) for energy dispersive X-ray spectroscopy (EDX) sensitive to all elements with $Z > 5$.

4.3.3. Transmission Electron Microscopy (TEM)

FePt layer structure as a function of the depth was analysed by TEM cross section investigations. A Philips CM300 microscope, equipped with a Schottky field emission gun (FEG) and operated at 300 kV, has been used. 5×5 mm² sample pieces, buried in glue, are mechanically thinned and subsequently ion milled (1 keV Ar ions with an incident angle of 2°). This procedure is significantly invasive and damaging layers deposited at high working pressure. The cross sections observation of FePt nanoislands was not successful because of a weak adhesion between the clusters and substrate. Therefore, only thick FePt layers were studied. Because of the high coercivity of the material, high resolution investigations had been very difficult. Using the electron diffraction it was possible, anyhow, to identify the FePt (110) indicating the existence of the FePt $L1_0$ phase.

4.3.4. Superconductive Quantum Interference Device

The Superconductive Quantum Interference Device (SQUID) magnetometer is a well-established equipment to characterise magnetic properties of specimens (Figure 4.17).

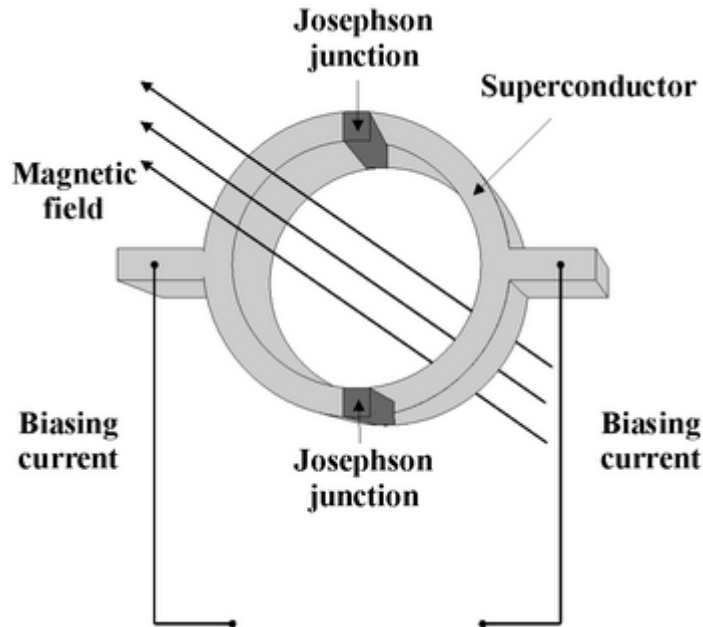


Figure 4.17: Scheme of a SQUID.

It consists of two superconductors separated by thin insulating layers in order to form parallel Josephson junctions [144]. It has a very high resolution and can measure magnetic moment up to 10^{-8} emu. The magnetisation M of the FePt layers was measured in a conventional SQUID magnetometer from Quantum Design Magnetic Property Measurement System (XXL - MPMS). It provides magnetic field of $-7 \text{ T} \leq H \leq +7 \text{ T}$ with temperature range of $1.9 \text{ K} \leq T \leq 400 \text{ K}$ at the sample. FePt measurements were performed in the Reciprocating Sample Option (RSO) mode at 300 K with the maximum slope technique [145]. In this work, the layer magnetic properties will be discussed in term of coercive field H_C and *squareness* S_q of the hysteresis loop. The coercive field measures the resistance of a ferromagnetic material to be demagnetized. Materials with high coercivity are called hard ferromagnetic, low coercivity indicates a soft ferromagnet. S_q is defined as the ratio between the remanence magnetization [$M_R = M(H = 0)$] and the saturation value M_S [146]: $S_q = 1$ for $M_S = M_R$. The (001) layer preferential orientation will provide an alignment of the hard magnetisation axis along the surface parallel, therefore the decrease of the in-plane S_q can be used as indicator of the degree of orientation of film.

In-plane geometry is realized when the magnetic lines are parallel to the specimen surface; on the contrary, the out-of-plane set-up when the magnetic field is applied perpendicular to the layer surface.

5. Investigation of the $A1$ - $L1_0$ phase transition

FePt films deposited at room temperature exhibit only the *fcc* soft magnetic $A1$ phase and a subsequent heat treatment at $T > 400$ °C is required to achieve the $A1 \rightarrow L1_0$ transition [17, 146]. But, with respect to a feasible fabrication technology, it is necessary to reduce significantly the processing temperature ($T \leq 400$ °C). Different methods have been explored to lower the transition temperature. In most cases, the decrease of the transition temperature T_T is based on an increase of the Fe/Pt atoms mobility which supports the atomic rearrangement towards the chemically ordered $L1_0$ phase [15]. Here it is described the effect of the deposition parameters towards a decrease of the transition temperature. In particular it will be discussed the role of the energetic budget impacting the substrate during magnetron sputtering deposition of ~ 70 nm FePt layers on a -SiO₂/Si(001) substrates. The preferential orientation of the layer will not be investigated at this stage.

The results here described were partially published in: *Nuclear Instruments and Methods in Physics Research B* 257, 1-2, 406 (2007).

5.1. Experimental parameters

FePt layers were deposited, by co-sputtering, at RT on Si(001) substrates of 15×15 mm² size covered with 1.5 μ m amorphous, thermally grown SiO₂. The base pressure was below 5×10^{-4} Pa and the operating Ar pressure at 0.3 Pa or 3 Pa, corresponding to the I_{dc} and V_{dc} characteristics reported in Table 5-1.

p (Pa)	t (s)	Target material	W_{dc} (W)	V_{dc} (V)	I_{dc} (mA)
0.3	1200	Fe	20	393	52
		Pt	5	396	12
3	2220	Fe	42	278	152
		Pt	3	298	12

Table 5-1: Deposition parameters.

Post-deposition annealing treatments at $T_A \leq 350$ °C for 20 min were carried out in vacuum ($< 10^{-5}$ Pa) in the annealing chamber at ROBL (paragraph 3.3.2) to perform *in-situ* X-ray scattering investigations at 8 keV. High pressure deposited layers were annealed *ex-situ* in the set-up described in paragraph 3.3.1, always for 30 min. *Ex-situ* X-ray investigations were performed by using the Siemens D5005 diffractometer at CuK α radiation (paragraph 4.2.4)

Low pressure (0.3 Pa) deposited FePt films were irradiated at RT or 250°C by He ions at 50 keV with fluences between $0.1 - 3 \times 10^{16}$ ion/cm². The displacement-per-atom (dpa) rate linearly scales with the fluence and amounts to 0.03 - 1 dpa, nearly constant throughout the whole film, as calculated by SRIM code [148]. The projected range of implanted He ions is about 320 nm: ions come to rest into the SiO₂ substrate.

5.2. Results

In Figure 5.1-a, the RBS data are shown, comparing between Fe_xPt_(100-x) layers deposited at 0.3 Pa and 3 Pa. In both cases the layer stoichiometry was calculated at $x = (50 \pm 1)$.

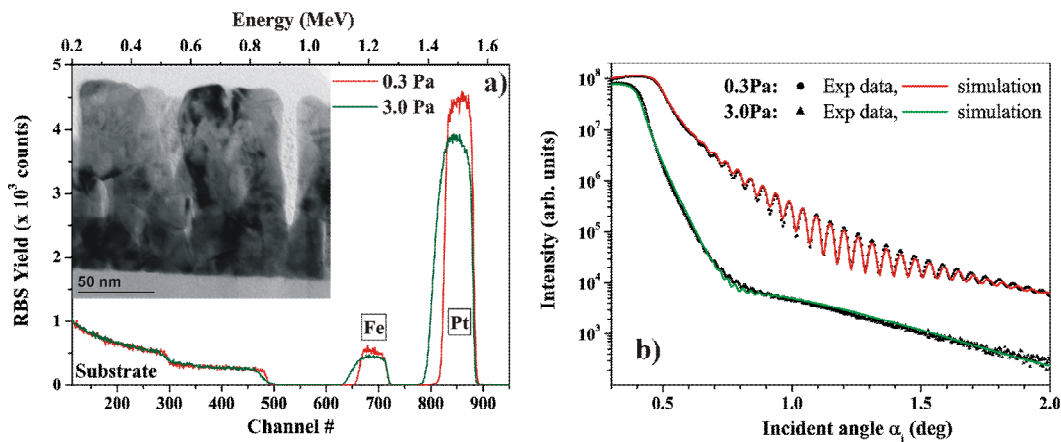


Figure 5.1: Comparison between a) RBS data and b) XRR analysis from as deposited films Fe₅₀Pt₅₀ deposited at 0.3 Pa and at 3 Pa. Inset: TEM cross section of the film grown at 3 Pa

The specimen deposited at 3 Pa showed a RBS signal with a smooth slope of the Fe, Pt and Si edges, indicating a high roughness. The Fe and Pt peak intensities difference, between the low and high pressure deposited layers, can be attributed to a lower density of the film grown at 3 Pa. At 0.3 Pa, the FePt atomic flux was calculated at 4.20×10^{14} at/cm²s, for 3 Pa, the atomic flux decreased to 2.56×10^{14} at/cm²s.

The layers were investigated with XRR (Figure 5.1-b) to have a clear indication of the layer thickness. Immediately it comes clear a shift in the critical angle position to lower values for the high pressure grown film: from 0.50° to 0.42°. From the simulation of the XRR data, the layer deposited at 0.3 Pa has thickness of 73 nm and surface roughness of 0.9 nm and is characterised by a thin (~ 1.4 nm) top-layer having a slightly lower density (~ 80%). These results are in good agreement with the RBS calculations that give a total thickness of 68 nm. Comparing RBS thickness value, evaluated supposing bulk density, and XRR result, it was calculated a density reduction of about 8 %, with respect to bulk values and a deposition rate at (0.60 ± 0.02) Å/s. From the XRR curve, the thickness of the layer grown at 3 Pa was calculated at 124 nm, with a very high surface roughness of 2.5 nm. On the contrary, from the RBS data, analysed with bulk density values, the layer thickness was estimated at 76 nm. From a direct comparison between the RBS thickness

and the XRR one, it was calculated a layer density decrease of 40%, respect to the bulk value [24]. These results are confirmed by the TEM cross section (Figure 5.1-a inset) indicating a structure composed by crystalline column shape grains divided by voids.

Figure 5.2 shows GIXRD patterns for the 0.3 Pa FePt film recorded during vacuum annealing. The layer was kept at each temperature for 20 minutes, during the GIXRD data collection, and subsequently heated at the next temperature.

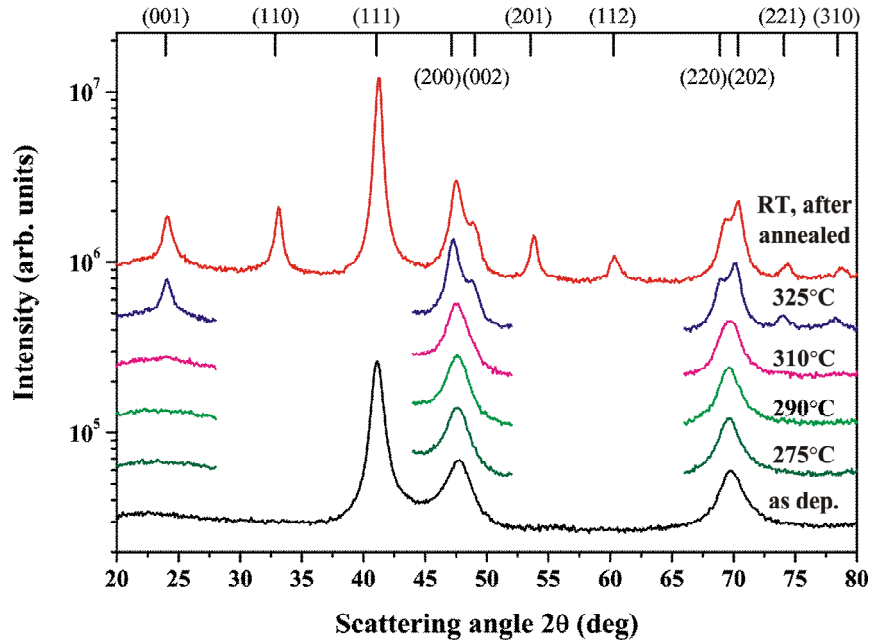


Figure 5.2: GIXRD patterns ($\alpha_i = 1^\circ$) recorded during vacuum annealing of the $\text{Fe}_{50}\text{Pt}_{50}$ layer deposited at 0.3 Pa. The tabulated peak positions [24] for the $L1_0$ reflections are indexed.

The as-deposited film clearly exhibits the *fcc* Al phase. The $\text{Al} \rightarrow L1_0$ transition starts at a temperature of 310°C and is almost completed at 325°C . The very narrow temperature range, in which the disorder - order transition occurs, makes *in-situ* X-ray investigations extremely suitable for this kind of studies. The $L1_0$ phase is easily detected by the presence of the (001) and (110) superstructure peaks and by the peak splitting [(200)/(002) or (220)/(202)] due to the tetragonal lattice distortion. The lattice parameters, calculated from the GIXRD data at RT after annealing [149], are $a = (3.85 \pm 0.01) \text{ \AA}$ and $c = (3.71 \pm 0.01) \text{ \AA}$, equal to the theoretical values for the $L1_0$ phase [24], within the error. The mean grain size, evaluated with the Scherrer's formula (paragraph 4.2.2, [127]), continuously increased with the temperature, from 6 nm of the as-deposited film, to 11 nm after annealing.

In Figure 5.3 the GIXRD data from the sample deposited at 3 Pa are reported, collected after vacuum annealing for 30 minutes. The as deposited layer is in the *fcc* Al phase, the disorder – order transition appeared firstly after thermal treatment at 350°C , but it was clearly detected after annealing at 400°C , with the appearance of the (001) and (110) superstructure peaks. On the contrary, it was not possible to detect a clear splitting of the

(200)/(002) and (220)/(202) reflections but only a shape deformation of the (200) and (220) peaks, indicating a lower degree of order in the film.

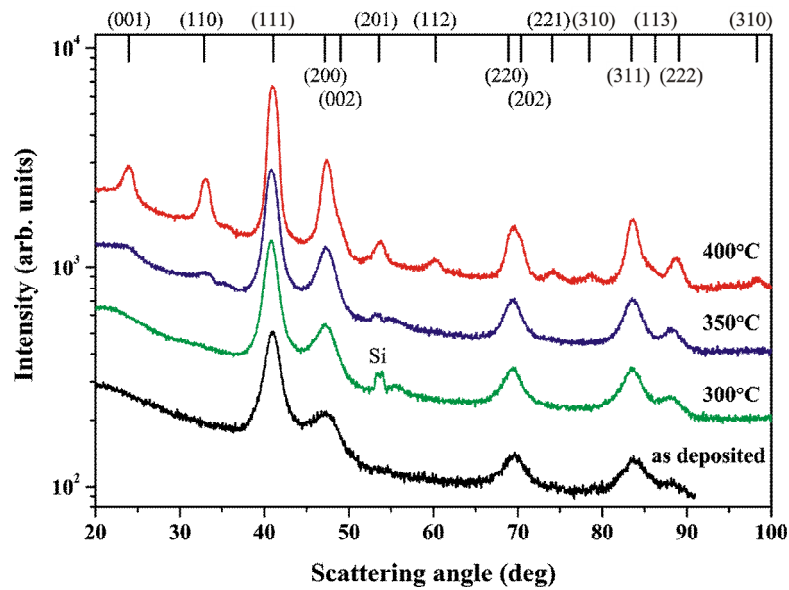


Figure 5.3: GIXRD patterns ($\alpha_i = 1.4^\circ$) recorded after vacuum annealing of the $\text{Fe}_{50}\text{Pt}_{50}$ layer deposited at 3 Pa.

The lattice parameters are $a = (3.850 \pm 0.003) \text{ \AA}$ and $c = (3.739 \pm 0.006) \text{ \AA}$ [149]. From the evaluation of the GIXRD FWHMs, it was detected a doubling of the average grain size with the annealing.

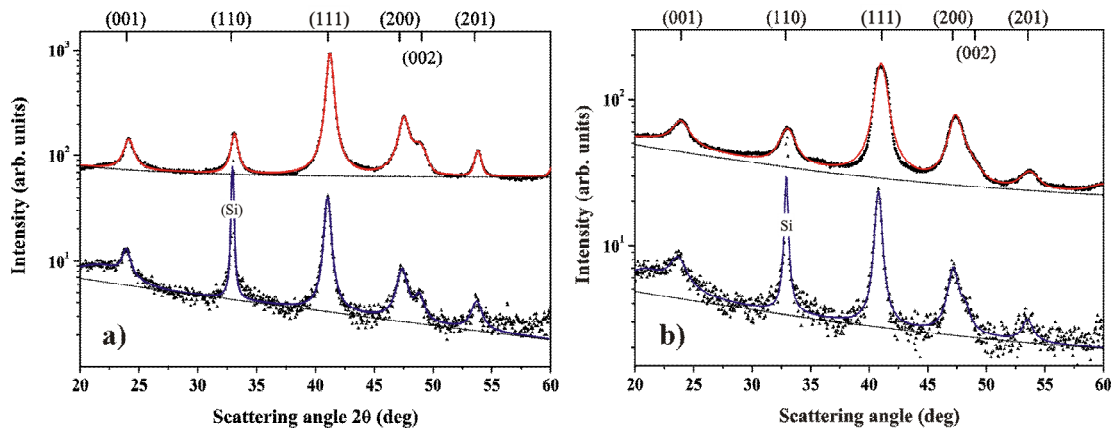


Figure 5.4: Comparison between a GIXRD ($\alpha_i = 1^\circ$) (upper curve) and a $\omega - 2\theta$ pattern (lower curve) recorded after vacuum annealing of the $\text{Fe}_{50}\text{Pt}_{50}$ layer deposited at a) 0.3 Pa and b) 3 Pa.

A direct comparison (Figure 5.4) between GIXRD and $\omega - 2\theta$ data confirmed a random, powder-like orientation of the film crystallites after annealing, irrespective to the deposition pressure. The long-range order parameter S can be determined from the GIXRD data with the procedure described in Appendix D. A value of $S = 0.94$ was achieved for the FePt film deposited at 0.3 Pa (Figure 5.4-a) after vacuum annealing at 325°C which

indicates a nearly complete Ll_0 ordered film. In the case of deposition at 3 Pa (Figure 5.4-b) the phase transformation is not complete, giving an order parameter $S = 0.62$.

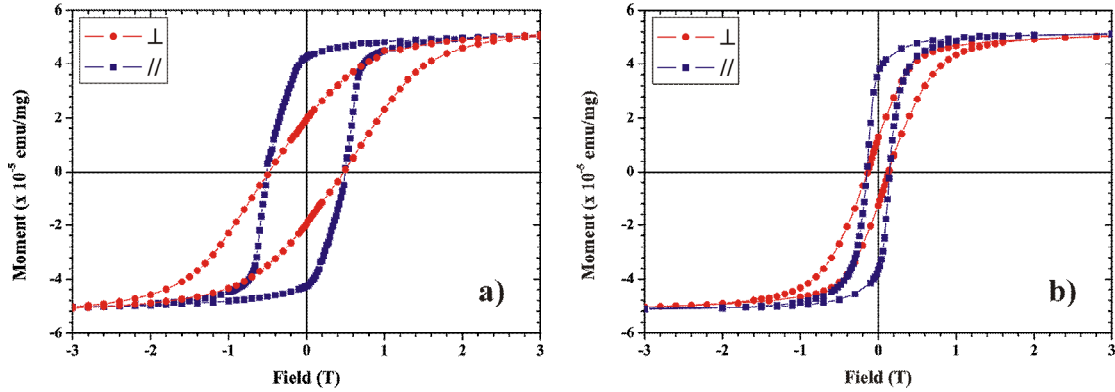


Figure 5.5: SQUID hysteresis loops at RT: a) 0.3 Pa and b) 3 Pa deposited layer.

The magnetic properties were investigated by SQUID at RT (Figure 5.5). The transition into the ferromagnetic Ll_0 phase, after annealing, is confirmed by the hysteresis loops (Figure 5.5) that reveal a coercivity of $H_C = 0.5$ T for the sample deposited at low pressure and $H_C = 0.2$ T for the 3 Pa grown layer. In both cases there is a partial alignment of the easy axes with the in plane direction that can be attributed to shape anisotropy. The hysteresis loops have a smooth slope, characteristic of a granular layer with partially decoupled grains. The loop *squareness* value S_q is 0.8 for both in-plane measurements, while there is a very weak difference between the two out-of-plane behaviours ($S_q(0.3 \text{ Pa}) = 0.4$, $S_q(3 \text{ Pa}) = 0.3$).

5.3. Discussion

Comparing the experimental results, before described, with the model developed in reference [16], and in particular with the TTT diagrams there reported (Figure 1.4), it comes out a strong reduction of annealing time required to obtain the same amount of Ll_0 phase in a FePt layer at $T_T = 300 \div 350^\circ\text{C}$. According to the JMAK model, the volume fraction transformed X_V can be written as:

$$X_V = 1 - \exp(-\gamma N \mathbf{v}^n t^n) \quad (5.1)$$

where γ is a geometrical factor equal to $4\pi/3$ for three dimensional growth (spheres), N is the Ll_0 nucleus density, t is the transformation time and n the Avrami exponent. \mathbf{v} is the growing velocity expressed in equation (1.3) [16] containing a negative exponential dependency from the transformation activation energy Q . The formation of short range order area, Ll_0 nuclei, is athermal: the nuclei are formed by a statistical arrangement of atoms resembling the ordered Ll_0 phase in the disordered Al matrix and it is not imputable to a particular deposition technique. Therefore, for an equal fraction of Ll_0 phase after annealing ($\sim 95\%$), supposing to have the same Ll_0 nucleus density in the as-deposited

state, a decrease of the transformation time should imply a faster growing rate and a lower transformation activation energy.

From our experimental result, we conclude that co-deposition of Fe and Pt via magnetron sputtering is already giving layers containing L1₀ nuclei in a Al matrix. Furthermore, for all investigated layers, the observed value of $T_T \cong 320^\circ\text{C}$ is only slightly above the characteristic temperature of 250°C where vacancies in metal films become mobile [35]. The low transition temperature and the short transformation time observed in our experiment suggest the presence of vacancies in the as-deposited layers at RT, reducing the chemical ordering to a vacancy jump probability. Therefore, a subsequent He⁺ irradiation is probably increasing the vacancy concentration but without any effect regarding the lowering of the transformation temperature. To confirm that, some RT deposited FePt films (~ 70 nm) were irradiated at RT or 250°C by He ions at 50 keV with fluences between $0.1 - 3 \times 10^{16}$ ion/cm². These parameters were chosen to have small energy transfers to minimize atom displacements; a low collision cross section in order to avoid vacancy interactions but sufficient beam energy to ensure that ions stopped inside the substrate.

In Figure 5.6 the influence of He⁺ irradiation fluences and temperature is shown by comparing X-ray $\omega - 2\theta$ analyses. The irradiation is not changing layer density and surface roughness as proved by XRR investigations, not showed here.

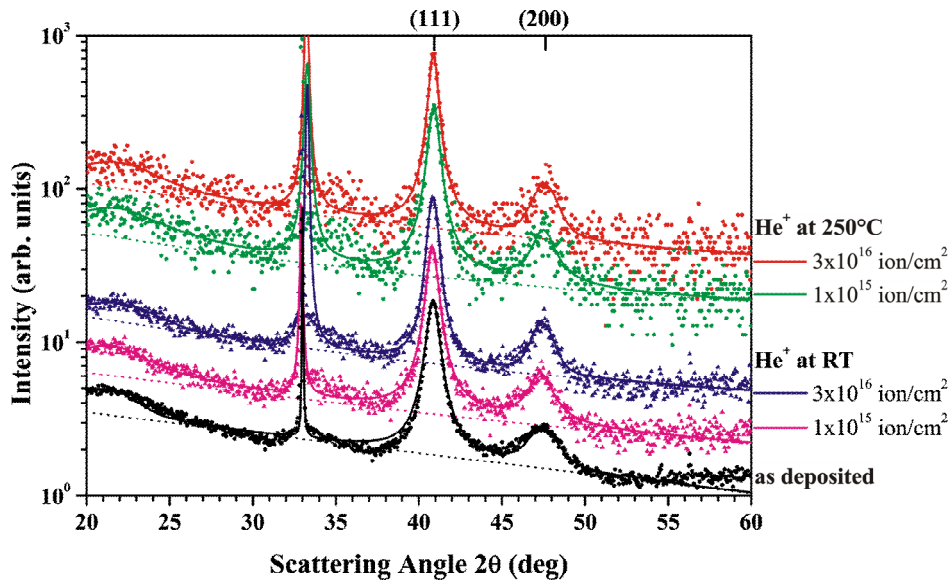


Figure 5.6: $\omega - 2\theta$ patterns collected after irradiation at RT and 250°C : comparison between the fluences 3×10^{16} ion/cm², 1×10^{15} ion/cm² and the as deposited layer.

All as deposited layers remain in *fcc* Al phase, independently from the irradiation conditions. The irradiation only causes a small increase of the grain size to 8 nm. Subsequently, the irradiated layers were annealed in vacuum at ROBL in order to detect, *in-situ*, the dependence of the phase transition temperature from the irradiation; an example, for the highest irradiation fluence, is reported in Figure 5.7. The *in-situ* GIXRD data showed no further lowering of phase transition temperature, on the contrary we obtain a slight increase of the T_T in comparison with the not irradiated films.

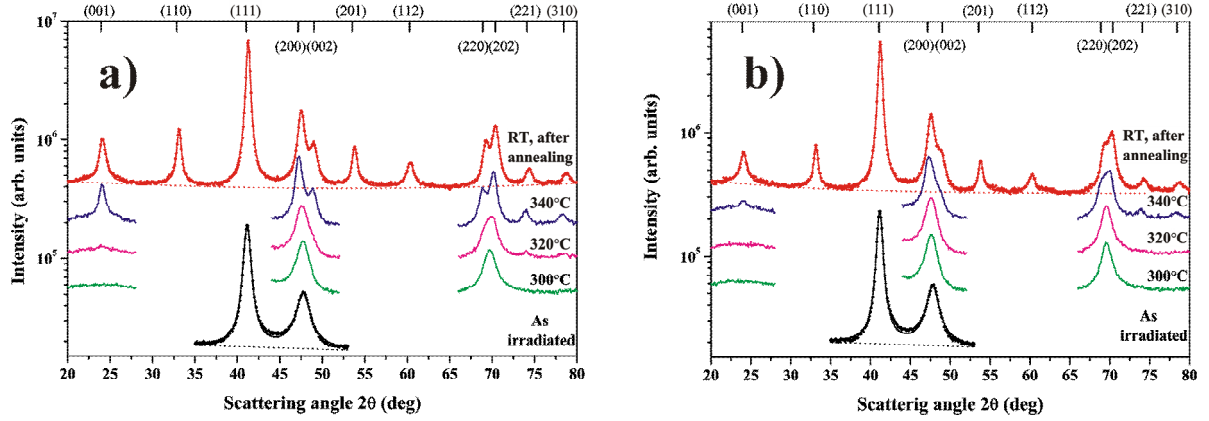


Figure 5.7: GIXRD patterns ($\alpha_i = 1^\circ$) collected during annealing: comparison between layers irradiated at the fluence of 3×10^{16} ion/cm² at RT (a) and at 250°C (b).

In the case of the layer irradiated at RT, the transition occurred at 340°C and resulted to be more complete ($S = 0.81$) than after irradiation at 250°C ($S = 0.74$), as confirmed by the difference in the superstructure peak intensities and by the not complete splitting of the (200)/(002) and (220)/(202) reflections. The thermal treatment caused a grain growth up to 12 nm for both investigated films. Comparing the *in-situ* GIXRD analysis during vacuum annealing of the irradiated layers (Figure 5.7) with the not irradiated films (Figure 5.2) we observed an increase of the transformation time, confirmed by a lower degree of order at the same annealing temperature.

As a consequence we suppose that already during deposition energetic particle impacts are generating enough vacancies to lower the thermal budget, in a comparable way as the He⁺ irradiation described in reference [35]. These hypotheses will be proved by estimating the energy impacting the substrate during deposition.

As a starting point, TRIDYN [97, 98] calculations were performed in order to get information about the energy distribution of the sputtered particles.

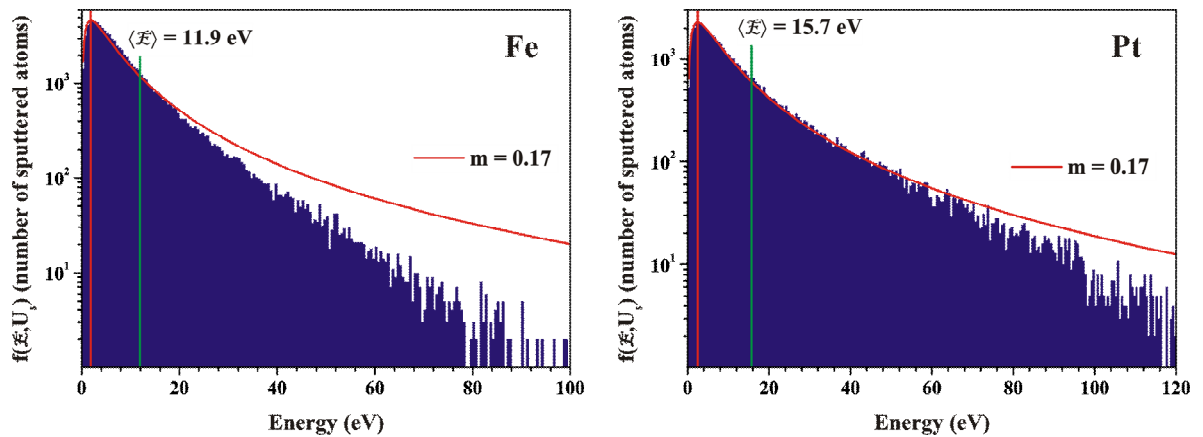


Figure 5.8: Energy distribution of the sputtered particles: Fe (left side) and Pt (right side).

For the case of Ar ions impacting the target with energy of 400 eV and normal incidence angle, the results are reported in Figure 5.8. TRIDYN results can be analytically approximated by the modified Thompson distribution function of equation (2.15). The

maximum number of Fe atoms is sputtered with an energy of 2.2 eV, with the mean energy of 11.9 eV, equation (2.16), with a sputtering yield $y_{sp} = 0.93$ at/ion. The maximum fraction of Pt atom is sputtered at the energy of 2.9 eV, obtaining $y_{sp} = 0.63$ at/ion, but the distribution mean value is at 15.7 eV. The maximum energy of the sputtered Fe atoms is 127 eV while for Pt is 145 eV.

According to the procedure described in paragraph 2.4, supposing an initial energy, at the target, $\langle E \rangle_{Fe} = 11.9$ eV $\langle E \rangle_{Pt} = 15.7$ eV it is possible to evaluate the mean free path and the average energy of the sputtered atoms at the substrate, after a distance $d = 10$ cm. The results are reported in Figure 5.9.

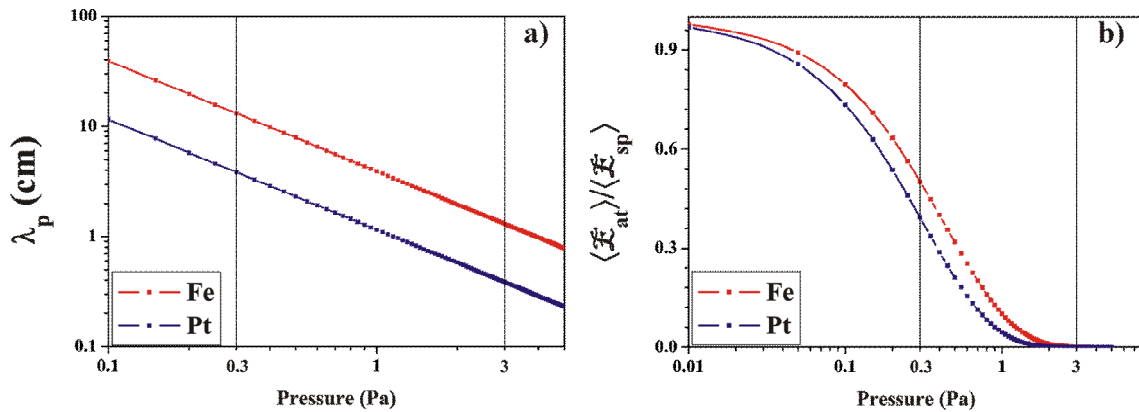


Figure 5.9: Mean free path (a) and energy decrease (b) for Fe and for Pt, as a function of the deposition pressure. The initial energy is the mean energy of the sputtered atom energy distribution: $\langle E \rangle_{Fe} = 11.9$ eV $\langle E \rangle_{Pt} = 15.7$ eV.

The calculated mean free path λ_p are 13.07 cm and 3.85 cm for Fe and Pt, respectively. As shown in Figure 5.9-b, the sputtered atoms reached the substrate surface with mean energies of 6.0 eV for Fe and 4.7 eV for Pt at 0.3 Pa. This means that about 50% of the initial sputtered atom energy is lost from the target to the substrate by ballistic collisions with the thermal gas atoms. Therefore, for this energy balance, the layer deposited at 0.3 Pa and RT should belong to the Zone 1 of the SZM model (Figure 2.5) [112], characterized crystalline columns shape grains separated by voids. That is in contrast with the previous results from RBS, XRR.

TEM investigations were performed to observe the layer cross section after annealing (Figure 5.10). Figure 5.10-a evidences a polycrystalline, granular, but compact, film without preferred orientation. Although no (001) spot is visible in the selected area diffraction (SAD) pattern (Figure 5.10-c), which is mainly due to low electron scattering intensity, the existence of the L1₀ phase is confirmed by the weak signal from the (110) and by the (220)/(202) splitting observed in SAD. By high-resolution TEM (Figure 5.10-b), it was possible to identify large FePt crystallites, with (001) planes with a spacing $d = 3.82$ Å.

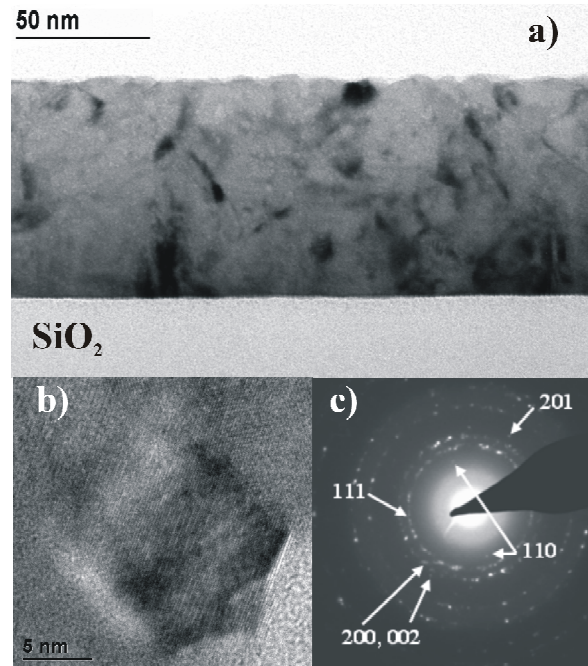


Figure 5.10: 0.3 Pa deposition: cross-section TEM micrographs of the film after annealing at 325°C. (a) Overview, (b) high-resolution image showing a large near-surface FePt crystallite, (c) SAD from \varnothing 1 μ m region, the main rings are indexed.

The contribution to the energy impacting the substrate given by the reflected Ar neutrals should be taken into account. In Figure 5.11 the backscattering yield and the mean energy of the Ar neutrals, reflected from the Fe and Pt targets, is reported.

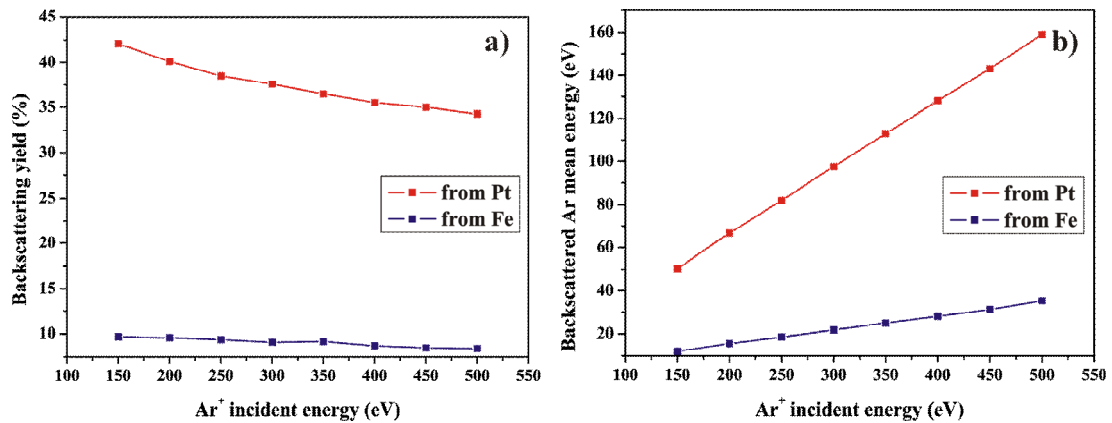


Figure 5.11: The backscattering yield (a) and the mean energy (b) of the Ar atoms at the target, calculated with TRIDYN, as a function of the Ar ion incident energies.

As expected, significant difference are obtained for the Fe and Pt target, as $m_{Pt} \gg m_{Ar}$. 36% of the total Ar ions are reflected by the Pt target, with a mean energy of 128 eV. The situation is significantly different in the case of the Fe target, where only 9% of Ar is backscattered with mean energy of 28 eV.

The Ar energy impacting the substrate, shown in Figure 5.12, was calculated according to the model described in Chapter 2.4, applying equation (2.25), for fast Ar travelling in thermalized Ar atoms. At 0.3 Pa, fast Ar neutrals can hit the substrate with an average

energy of 89 eV that exceeds the displacement energy threshold (~ 25 eV), necessary for point defect formation. Already during deposition at 0.3 Pa, energetic backscattered Ar atom impacts cause the formation point defects together with ions and sputtered atoms supported adatom mobility, creating the conditions to have a significant shorter phase transition time by decreasing the activation energy for the order transformation.

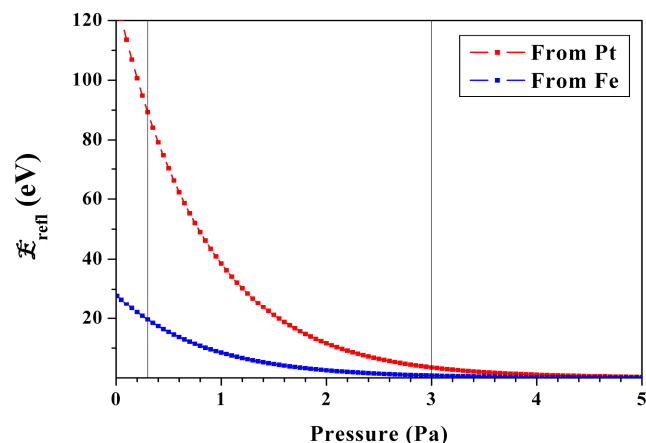


Figure 5.12: Mean energy of the backscattered Ar at the substrate position ($d = 10$ cm).

At 3 Pa the maximum energy for Ar neutrals impacting the substrate is only 3.5 eV. Higher operating pressure leads to a strong thermalization of the incident atoms and ions, which lowers the surface adatom mobility and suppresses the formation of point defects. According to Messier's model [112], with such low energy impacting the substrate, the layer should belong to the Zone M of the SZM (Figure 2.5) characterised by dome-shaped surface with clusters evolving in columns between 20 and 200 nm, this morphology was confirmed by the SEM and TEM investigations reported in Figure 5.13.

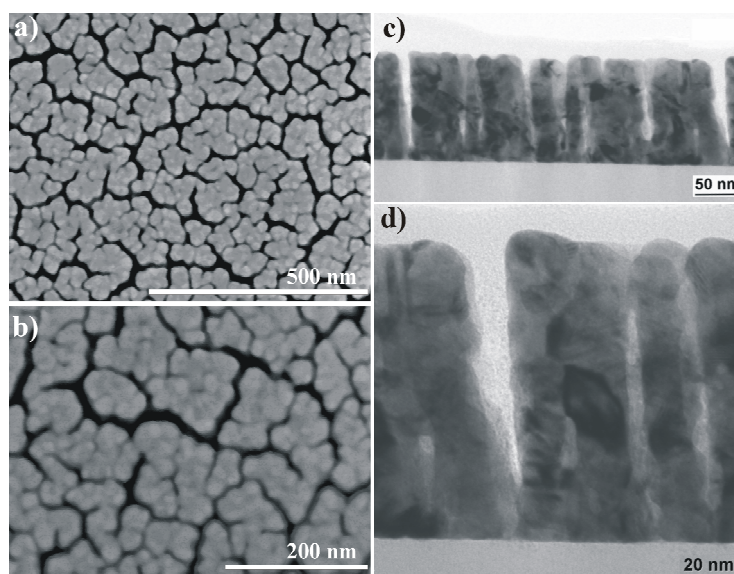


Figure 5.13: 3 Pa deposition: micrographs of the film after annealing at 400°C. a, b) SEM plain views, c, d) TEM cross-sections.

After annealing, the layer deposited at 3 Pa is characterised by percolated granular agglomerates (Figure 5.13). From SEM and TEM micrographs, it comes out that the clusters are separated by voids that can almost reach the substrate (Figure 5.13-d). The nanoislands, completely polycrystalline, can arrive to in-plane dimensions up to 200 nm. The layer thickness can be estimated by TEM cross-section picture to 123 nm, in complete agreement with the XRR results.

The SQUID (Figure 5.5) hysteresis loop shapes and the coercive field value indicate a layer characterised by a granular structure with not strongly coupled domains, also at 0.3 Pa growths. In fact, defect in magnetic materials, like grain and phase boundaries, can form pinning sites that impede the movement of magnetic domain walls leading to high coercivity [146, 146]. This behaviour can be explained with the low processing temperature (350°C) at which the film structure is not completely homogeneous.

5.4. Summary

The $L1_0$ -ordering of stoichiometric FePt films (~ 70 nm) deposited on amorphous SiO_2 by dc magnetron co-sputtering has been studied. The $A1 \rightarrow L1_0$ transition and the degree of ordering have been investigated as a function of the deposition pressure.

The FePt layers produced at 0.3 Pa showed a phase transformation at the low temperature of $(320 \pm 20)^\circ\text{C}$ (Figure 5.2). The film surface is smooth and it was not measured a significant loss of density with respect to the bulk value (Figure 5.1). The phase transformation is complete ($S > 0.94$) and the magnetic property measurements confirmed a high coercive field ($H_C = 0.5$ T, Figure 5.5-a). The layer produced with an operating pressure of 3 Pa revealed an increase of the transition temperature to 400°C (Figure 5.3). The layer morphology is characterised by percolated clusters divided by voids with 40% loss in density with respect to the bulk. After annealing it was measured a significant reduction of the long-range order parameter ($S \cong 0.6$) and of the coercivity ($H_C = 0.2$ T, Figure 5.5-b). The lower values of S and H_C suggest that even after 400°C annealing, a certain amount of the FePt alloy is still in the disordered, soft magnetic phase.

TRIDYN simulations and theoretical calculations revealed that for our experimental conditions no thermalization of the sputtered atoms and the reflected Ar neutrals occur in the plasma at 0.3 Pa. Fe and Pt will impact the substrate with an average energy of ~ 5 eV, while reflected Ar neutrals from the Pt target exhibit a mean energy of ~ 89 eV well above the displacement threshold. Therefore the low transition temperature, for the layer grown at 0.3 Pa, is explained in the reduction of the activation energy for atomic reordering by point defects, created by energetic impacts during deposition, which becomes mobile at temperatures $\geq 250^\circ\text{C}$. In fact, an additional post-deposition ion irradiation with He^+ at RT or at 250°C (50 keV, $1 \times 10^{15} - 3 \times 10^{16} \text{ cm}^{-2}$) does not influence this low transition temperature. At the growing conditions of strong thermalization (deposition at 3 Pa), the FePt film showed an increase of the transition temperature to 400°C and a reduced film density. Energetic particles impacts, low working pressure depositions, are therefore fundamental to enable a low disorder – order transformation temperature.

6. Preferred c -axis orientation in thin FePt films

Because of the need to obtain the magnetic moment alignment perpendicular to the film surface, the mechanism to achieve the (001) FePt preferential orientation must be investigated and controlled. Moreover, in the optic of real industrial applications, the film thickness must be strongly reduced. This will lead to an increase of the $A1$ to $L1_0$ transformation temperature [16].

To further decrease the $L1_0$ phase formation temperature, two different deposition techniques were applied. The co-deposition method, already studied for thicker films, will be compared with the layer – by – layer one. In the last one, the layer growth is performed by alternating Fe and Pt thin (from ~ 3 to ~ 1.5 Å) films to build, already at the deposition stage, a structure that emulates the $L1_0$ one and to reduce the random atom path to an atomistic scale [40]. This technique should also promote the formation of directional short range order needed to promote film (001) preferential orientation during annealing [35].

6.1. Growths on crystalline substrate

This experiment was mainly performed to investigate the influence of layer thickness on the FePt phase transformation. At this purpose, thin layers (~ 14 nm) were grown at the transition temperature of 350°C , previously studied for thicker layers. The choice of a crystalline substrate, MgO (001), is made to create favorable conditions to support the layer (001) preferential orientation.

6.1.1. Experimental parameters

FePt films were deposited, by co-sputtering and layer – by – layer deposition, at RT and 350°C on MgO(001) substrates of 10×10 mm² size, without any Ar pre-sputtering to clean the substrate surface. The layer – by – layer deposition had a period $N = 20$. The base pressure was below 5×10^{-4} Pa and the operating Ar pressure at 0.3 Pa. The magnetrons run with a power of 14 W for Fe and 3 W for Pt, corresponding to the I_{dc} and V_{dc} characteristics of 37 mA and 380 V for Fe and 8 mA and 375 V for Pt. The deposition time was 680 s and 340 s for the layer – by – layer and the co-sputtering methods, respectively.

The layer grown in the co-deposition technique was kept at the deposition temperature for the remaining time to equal the time of the layer – by – layer procedure.

RT deposited layers were annealed at $T_A = 550^\circ\text{C}$ for 600 s (heating rate: 5°C/s) in vacuum, in the set-up described in paragraph 3.3.1. All films were measured by RBS in order to obtain minimum thickness and stoichiometry. *Ex-situ* X-ray investigations were performed by using the Siemens D5005 diffractometer and the Seifert HRXRD at $\text{CuK}\alpha$. SQUID magnetometer analyses were performed at 300K.

6.1.2. Results

The RBS data revealed no strong difference between the layers deposited at RT and the ones at 350°C . For all films the mean stoichiometry was calculated to Fe (54 ± 1) at.% : Pt(46 ± 1) at.% corresponding to an average atomic flux of 1.51×10^{14} and 1.46×10^{14} at/cm²s for Fe and Pt, respectively.

The XRR data of the films are compared Figure 6.1.

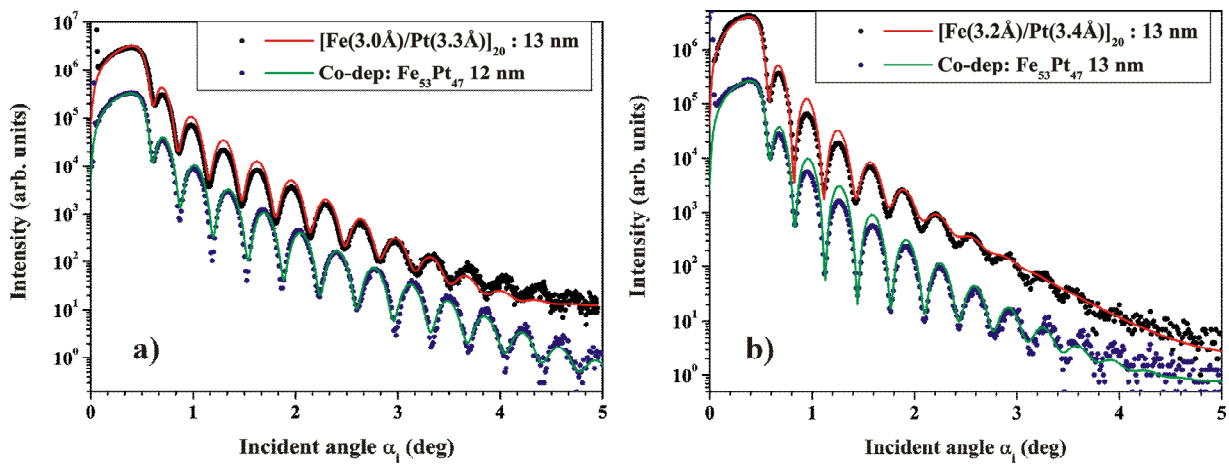


Figure 6.1: Comparison between XRR analyses from layer – by – layer and co-deposition technique: a) at RT, b) at 350°C . In the multilayer-like growths the single Fe or Pt film thickness is estimated by RBS measurements.

The growth temperature mainly influences the layer surface roughness evidenced by the permanence of the reflectivity oscillations to higher incident angles. The films deposited at RT have roughness of 0.2 nm and 0.5 nm for the co-deposition and the layer – by – layer growths, respectively. Also in the case of layers grown at 350°C , the surface roughness of the film produced by layer – by – layer technique showed a higher value (~ 0.8 nm) than the one co-deposited (~ 0.4 nm). Irrespective to the grown temperature, it is possible to identify, over the films grown by co-sputtering, very thin (~ 1 nm) surface layer having lower density than the bulk value (30% for the growth at RT and 25% at 350°C). The same is not observed in layers grown by multilayer sequence deposition because of the higher surface roughness.

The total thickness in all cases is (12.5 ± 0.6) nm, the values for the single layer is mentioned in Figure 6.1. All layers showed densities very close to the bulk one, confirmed by the position of the layer critical angle α_c for total external reflection.

Because of the interface roughness it is not possible to obtain any information about the multilayer quality by X-ray scattering analysis, no superlattice peak was detected at the expected position.

In Figure 6.2 the GIXRD patterns, collected at $\alpha_i = 0.6^\circ$, are shown.

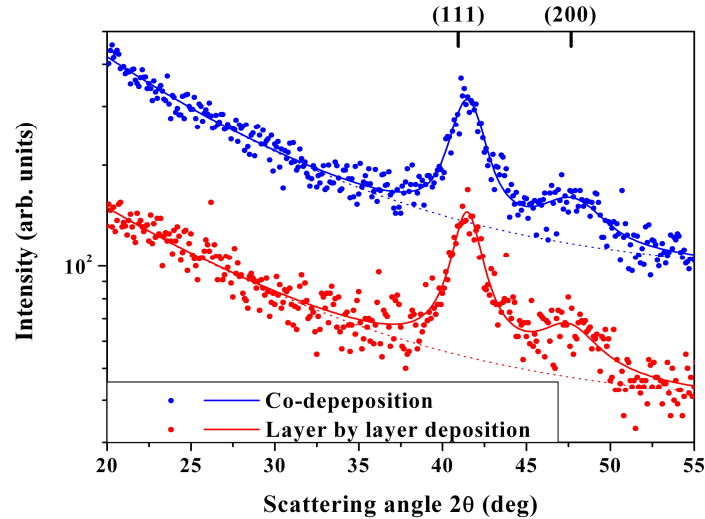


Figure 6.2: GIXRD ($\alpha_i = 0.6^\circ$) of the RT as-deposited layers: comparison between the co-deposition and the layer – by – layer technique. The theoretical positions of the (111) and (200) reflections from the *A1* phase are marked [22]

No strong difference can be detected from the layers deposited at RT, irrespective to the deposition technique used. Both layers are in the soft magnetic *A1* phase, characterized by ~ 4 nm grain size. The degree of crystallinity, evaluated by the integrated intensities of the (111) reflections, is slightly enhanced by the co-deposition technique ($A(111) \sim 600$, $\text{FWHM} = 2.3^\circ$ co-depositions; $A(111) \sim 300$, $\text{FWHM} = 2.1^\circ$ layer – by – layer growths). No influence of the deposition technique was measured on the lattice constant: $a = (3.83 \pm 0.05) \text{ \AA}$, calculated from the GIXRD reflection positions.

In Figure 6.3 the layers deposited at 350°C are compared by ω - 2θ patterns collected with an offset of -0.5° in respect with the MgO (002) Bragg condition, to decrease the signal from the substrate. The epitaxial relation between the substrate and the FePt layer forces a (001) preferential orientation of the deposited film, as confirmed by the GIXRD pattern where no reflections are detected (Figure 6.3-inset). In symmetric X-ray measurements (Figure 6.3) the main signal is due to a superposition of the (002) reflections from the *fcc* *A1* and *L1₀* phase, that slightly moves towards the *L1₀*-(002) direction for the film obtained in layer – by – layer mode. A clear proof of the presence of the *L1₀* phase in the layers is the signal from the (001) superstructure peak, even if the strong intensity of the (002) peak in comparison with the (001) suggested a very low fraction the *L1₀* phase in layers deposited at 350°C . The long range order parameter S was estimated at 0.15 for the layer grown in co-deposition mode and 0.26 for the layer – by – layer method. The integrated intensities of the (200) reflections assumed comparable values, indicating the same degree of crystallinity for both layers, irrespective to the deposition conditions. The comparison

between the integrated intensities of the (001) peaks confirmed a higher amount of $L1_0$ scattering centres in the film grown by the multilayer sequence deposition.

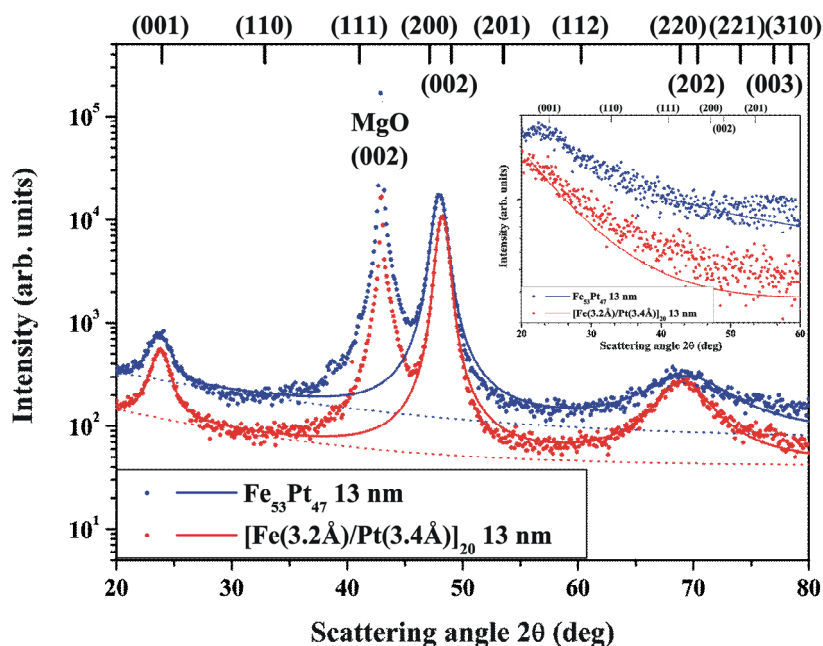


Figure 6.3: ω - 2θ patterns (offset = -0.5°) of the layers deposited at 350°C : comparison between the co-deposition and the layer – by – layer technique. Inset: GIXRD patterns collected at $\alpha_i = 0.6^\circ$

A very broad peak, composed by the superposition of the (220)/(202) reflections, is detected at $2\theta \sim 70^\circ$, indication of the layer crystalline fraction not (001) oriented.

The rocking curves, around the (001) and (002) peaks are shown in Figure 6.4. The FWHM of the (002) rocking curves results to be much smaller ($= 2.6^\circ$ and $= 2.0^\circ$ for the co-sputtering and the layer – by – layer mode, respectively) than the one measured from the (001) peaks ($= 7.5^\circ$ for the co-sputtering and $= 5.3^\circ$ for the layer – by – layer). Because the films are composed by a mixture of two phases nothing can be concluded regarding the angular distribution of the scattering planes around the (001) direction. The difference in the integrated intensities under the (001) rocking curve confirmed the higher degree of *fcc* phase in the film grown by layer – by – layer deposition mode.

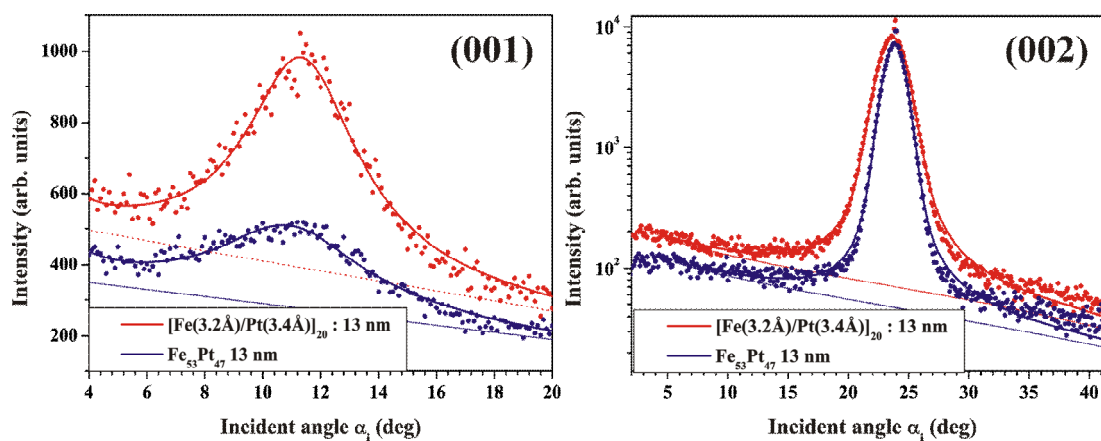


Figure 6.4: Rocking curves around the (001) and (200) reflections.

Figure 6.5 shows the magnetization versus field reversal (M - H) at RT, of samples deposited at 350°C.

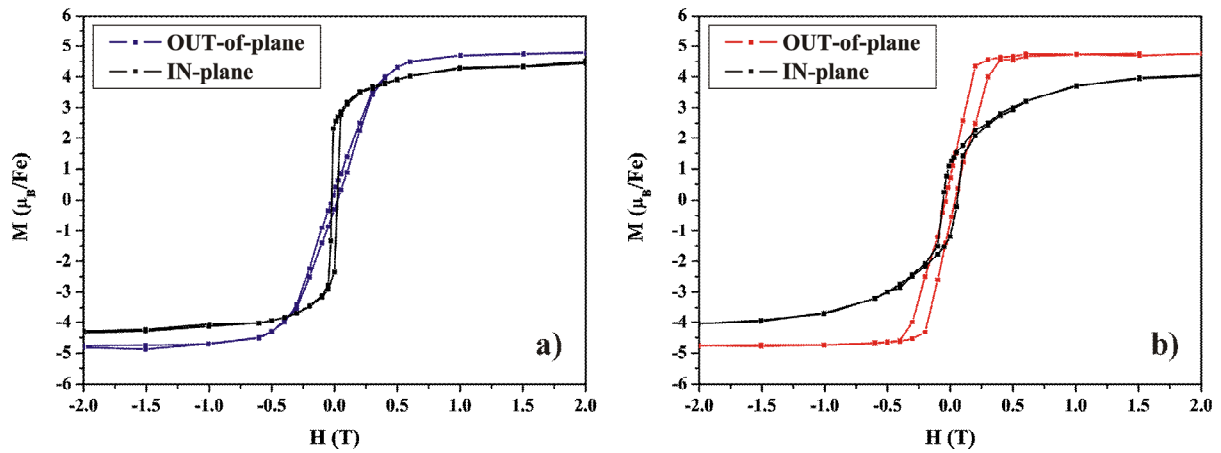


Figure 6.5: Hysteresis loops measured at RT for the layers grown at 350°C: a) co-deposition, b) layer – by – layer mode.

The layers mainly show the contribution of the soft-ferromagnetic phase $A1$ with small signal from the $L1_0$ phase, especially evident in the higher coercivity of the film grown in the multilayer sequence deposition. The coercivity fields are 2.6×10^{-2} T and 5.0×10^{-2} T for the co-deposition and layer – by – layer technique, respectively. The magnetisation easy axis lie in the out of plane direction in both cases, but the magnetic anisotropy is enhanced by the layer – by – layer deposited film. The saturation magnetisation has comparable values because of the same layer thickness.

Because of the low degree of order in 13 nm layers deposited at 350°C, the annealing temperature was chosen at 550°C, according to the TTT diagrams (paragraph 1.2) for a complete $A1$ to $L1_0$ transformation.

In Figure 6.6 the X-ray scattering investigations are reported. In the ω - 2θ geometry, mainly the (00 l) reflections could be detected that is a clear sign of the high (001) preferential orientation of the layer. A weak signal from the (111) peak also appeared but its evaluation is strongly altered by the presence of the (002) reflection from the MgO substrate. The order parameter, along the c -axis, was calculated at $S = 0.99$ the layer – by – layer and $S = 0.87$ for the co-deposition technique, confirming the high degree of LRO in the films. Around the FePt (001) peak it is possible to identify thickness oscillations fringes (Figure 6.6-inset), which period is inverse proportional to the layer thickness and confirms a sharp interface between the substrate and the FePt layer. The average grain size was estimated at 11 nm irrespective to the growing methodology.

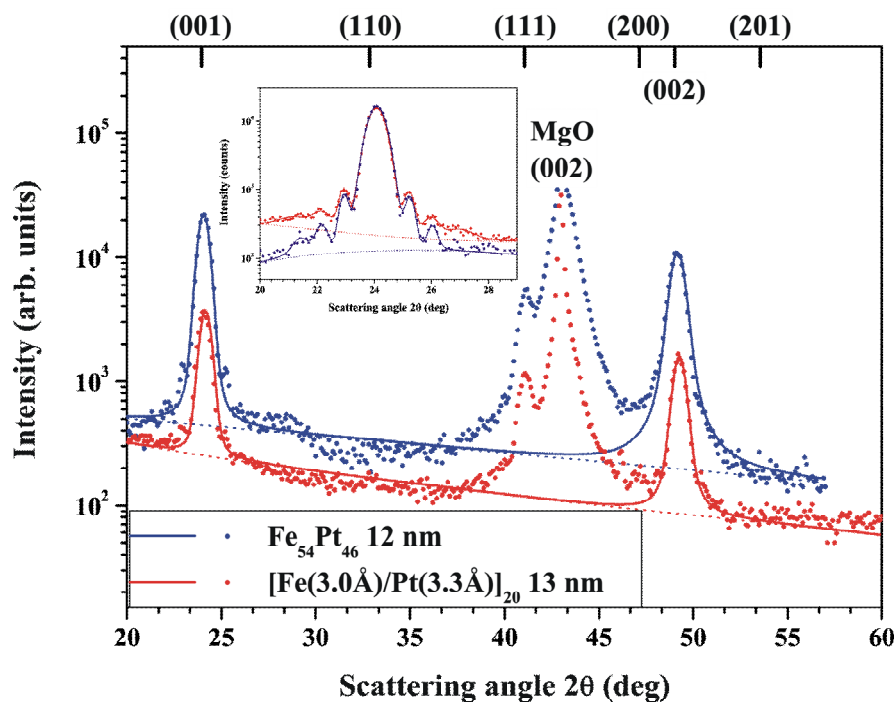


Figure 6.6: ω - 2θ patterns (offset = -0.5°) of the layers after annealing at 550°C : comparison between the co-deposition and the layer – by – layer technique. Inset: ω - 2θ patterns, in Bragg condition, around the (001) reflection.

The rocking curves around the (001) reflection are reported in Figure 6.7. The (001) planes are exactly, within the instrument resolution (0.12°), perpendicular to the layer surface, for both deposition techniques. By comparing, the FWHM of the rocking curve around the (001) and (002) peak, the angular dispersion is $\sim 1^\circ$, independently from the deposition technique.

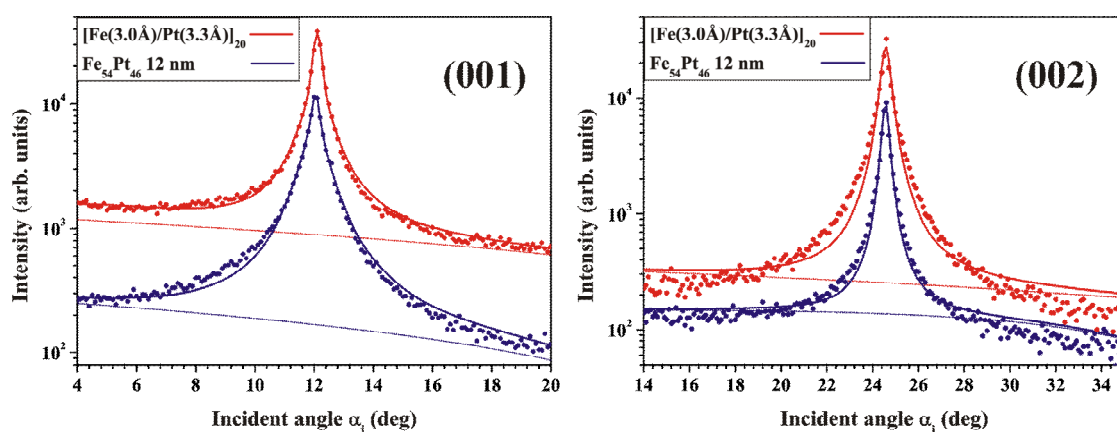


Figure 6.7: ω rocking curves around the FePt (001) (left side) and (002) peak (right side).

The calculation of the c lattice constant from the (00 l) reflections revealed a contraction of 3.7% with respect to the initial average value of the as-deposited state, independently from the deposition technique: the deformation of the FePt crystal structure, to compensate the

8.5% misfit with the substrate, must be confirmed by computing all unit cell lattice constants.

Because of the strong (001) preferential orientation of the FePt layers, the signals arising from the $(hk0)$ reflections are very weak in a coplanar geometry while the same are easy to be evaluated in the non coplanar one by in-plane measurements, where the scattering vector is almost parallel to the sample surface and therefore only the $(hk0)$ reflections are measurable. The results are shown in Figure 6.8 for the film grown in co-sputtering mode after annealing at 550°C. This grazing-incidence-grazing-exit investigation was carried out at the Seifert XRD3003 high resolution diffractometer with an incidence $\alpha_i = 0.6^\circ$.

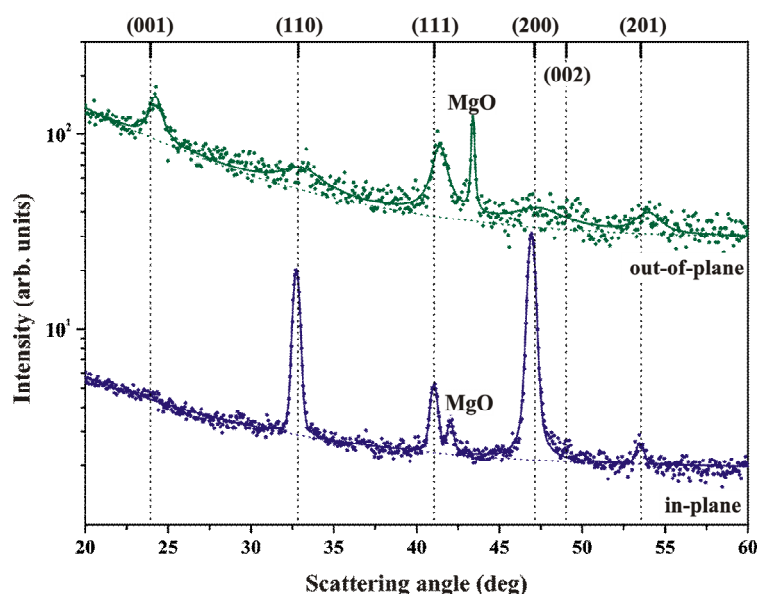


Figure 6.8: GIXRD ($\alpha_i = 0.6^\circ$) in the coplanar (out-of-plane, upper curve) and non coplanar geometry (in-plane, $\alpha_i = 0.6^\circ$ $\alpha_f = 1.2^\circ$, bottom curve) for the film grown in co-deposition mode after annealing.

The disappearing of the $(00l)$ reflections in the in-plane measurements confirm the (001) layer preferential orientation.

The calculated lattice constants [149] are $a = (3.87 \pm 0.01) \text{ \AA}$ and $c = (3.69 \pm 0.02) \text{ \AA}$. Together with a contraction along c it was observed a dilatation of a of 1% respect to the average value calculated for the as deposited films.

The SQUID hysteresis loops for the specimen deposited at RT and subsequently annealed at 550°C are reported in Figure 6.9. The coercive field is strongly increased, together with the degree of orientation of the magnetization easy axis in the out of plane direction, slightly further increased by the layer – by – layer deposition technique. When the magnetic field H is applied along the hard axes, parallel to the layer surface, the magnetization saturation is hardly reached at magnetic fields around 7 T. The coercivity reached 1.6 T and 1.7 T in the out of plane direction for the co-deposition and layer – by – layer technique, respectively. The smooth slope of all hysteresis loops and the huge out of

plane coercive fields evidenced films with granular structure, with grains not perfectly magnetically coupled.

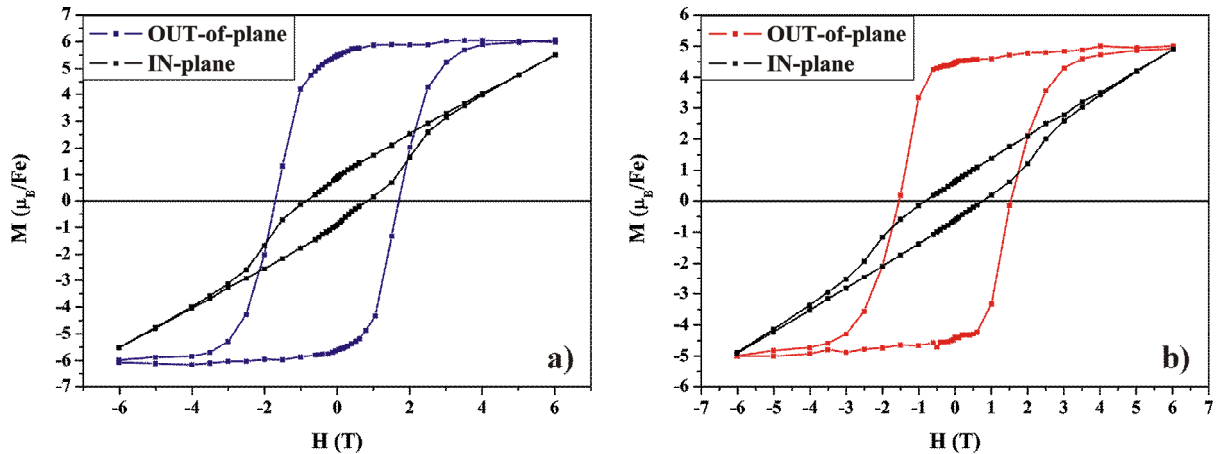


Figure 6.9: Hysteresis loops measured at RT for the layers grown at RT and annealed at 550°C: a) co-deposition, b) layer – by – layer mode.

6.1.3. Discussion

The difference of the roughness between depositions at RT and at 350°C can be explained considering the different surface energies of FePt ($\sim 2.9 \text{ J/m}^2$) in respect to the MgO ($\sim 1.1 \text{ J/m}^2$) [56]. FePt is expected to follow the Volmer-Weber growth, organising in nanoclusters at the beginning of the layer deposition that successively will weld together to form a closed layer structure [150]. The initial surface roughness is then partially levelled during growth, but the resulting layer surface roughness is still maintaining memory of the arrangement of the first growing stages and the temperature is increasing clustering at the beginning of the depositions.

In agreement with the TTT diagrams [16], 350°C was not a sufficient temperature to provide highly ordered layers like in the case of thickness around 70 nm. This result is in agreement with the investigations performed on the dependency of the transformation temperature on the layer thickness (appendix F and paragraph 7.2). The JMAK model assumes an infinite thick medium, without boundaries. In thin layers, where the surface to volume ratio is bigger, surface boundaries force the Ll_0 growth in an anisotropic way, along the layer, lengthening the transformation time at a fixed temperature (figure 6.10).

The vacancy creation, from energetic impacts of the backscattered Ar, it is not enough to overcome the limitations in the transformation temperature imposed by the layer thickness.

The main effect of the growth method arose with depositions at 350°C. The layer – by – layer mode increased the Ll_0 fraction and layer (001) orientation. This is due to the higher probability of realizing Ll_0 nuclei when depositing, decreasing the atoms random path, towards ordering, to an atomistic scale [40, 42]. The enhanced orientation is justified considering the Kinetic Lattice Monte Carlo simulations described in reference [35], proving that an initial DSRO is the necessary basis to produce a preferential orientation

along the (001) direction. The presence or absence of an initial DSRO comes clear only once a detectable fraction of the layer is in the ordered LI_0 phase.

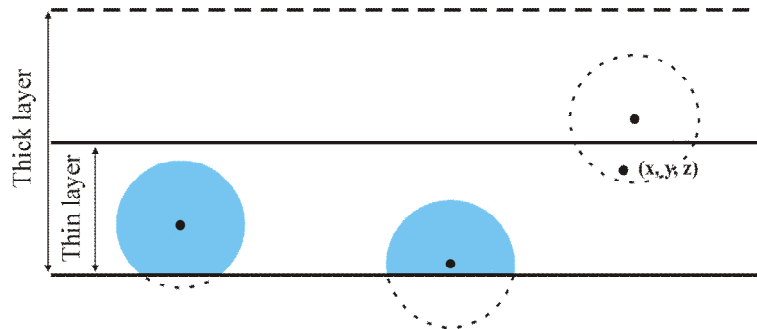


Figure 6.10: The effect of surface on the $AI - LI_0$ transition. The LI_0 fraction (blue areas) will increase only by being transformed from nuclei that are within the film. Point (x, y, z) must be transformed by a nucleus farther away, lengthening the transformation time [16].

After annealing at 550°C , the multilayer sequence deposition only slightly supports the layer (001) preferential orientation: the thermal process at so high temperature (550°C) is equalizing the two growing technique. The epitaxial relationship between FePt and MgO is anyhow predominant over the growing methodology.

In conclusion, by using a single crystal MgO (001) substrate, we were able to obtain highly (001) oriented and ordered 13 nm FePt layers after vacuum annealing at 550°C for 600 s.

6.2. Growths on amorphous substrate

In this paragraph it will be described and discussed the effect of the deposition methodology, the discharge gas type (Ar and Xe) and the annealing conditions on the FePt layer properties in relation to the control of the FePt (001) preferential orientation. To better understand the mechanism of (001) orientation development, FePt was deposited on α -SiO₂. This substrate, unlike the (001) MgO single crystal before described, gave no support to layer c -axes orientation perpendicular to the surface. The choice to use an amorphous substrate made the conclusions here enunciated valid for FePt thin films deposited by magnetron sputtering in general, allowing a complete freedom in choosing the buffer layer and the soft magnetic under-layer more suitable for recording media applications.

6.2.1. Experimental parameters

FePt layers were deposited, by co-sputtering and sequential Fe/Pt layer – by – layer deposition, in Ar or Xe discharges at RT on α -SiO₂(500 nm)/Si(001) substrates of $15 \times 15 \text{ mm}^2$ size. The layer – by – layer deposition had a period $N = 20$ and 50 , keeping the total layer thickness constant. Therefore, for $N = 50$, the single layer thickness is about one atomic-layer. The base pressure was below 5×10^{-4} Pa and the operating pressure at 0.3 Pa. The electrical magnetron inputs are reported in the following table.

<i>Gas</i>	<i>Fe</i>			<i>Pt</i>		
	W	V_{dc} (V)	I_{dc} (mA)	W	V_{dc} (V)	I_{dc} (mA)
Ar	16	(385 ± 5)	(41 ± 2)	3	(380 ± 2)	8
Xe	25	(420 ± 8)	(59 ± 2)	3	(420 ± 5)	8

Table 6.2-1: Magnetron working parameters (three different Fe target were used in this study).

The RT deposited layers were annealed by RTA (paragraph 3.3.3) at $T_A = 550^\circ\text{C}$ for 600 s (heating rate: 100°C/s) in Ar flow, or in vacuum at 700°C for 600 s (heating rate: 5°C/s) in the set-up described in paragraph 3.3.1. During RTA annealing the sample was “up-side-down” to avoid any possible contamination of the annealing chamber.

The layers were measured by RBS in order to obtain film minimum thickness and stoichiometry. *Ex-situ* X-ray investigations were performed by using the Siemens D5005 diffractometer at $\text{CuK}\alpha$ radiation. SQUID magnetometer analyses were performed at 300K .

6.2.2. Results

6.2.2.1. As deposited layers

In Figure 6.11, it is reported a comparison between RBS investigations (at an incidence angle of 70°) on layers deposited at RT, 0.3 Pa in Ar or Xe discharge. The layer – by – layer deposition method was applied to grow the film in Ar, extending the deposition time to 680 s in comparison with the 300 s for the co-deposited layer in Xe. From the RBS data there is only a weak signal from possible Xe embedded in the layer, which concentration is anyhow below 1 at.%. From RBS raw data analysis by RUMP [142], the amount of deposited material and the layer composition were calculated: the average values are reported in Table 6.2-2.

Gas	Fe (At/cm^2s)	Pt (At/cm^2s)
Ar	$(8.39 \pm 0.38) \times 10^{13}$	$(6.77 \pm 0.03) \times 10^{13}$
Xe	$(1.36 \pm 0.25) \times 10^{14}$	$(1.16 \pm 0.03) \times 10^{14}$

Table 6.2-2: Amount of deposited material.

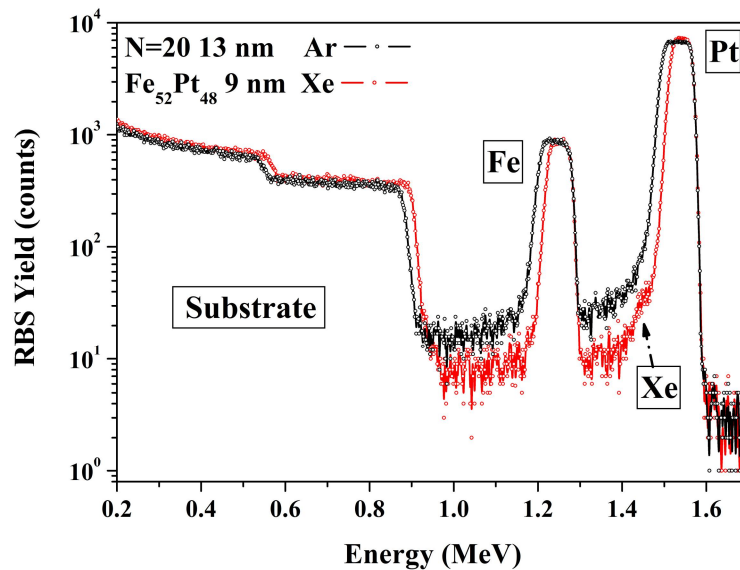


Figure 6.11: RBS at incidence angle of 70° . Comparison between a RT Xe co-deposition for 300 s and a layer – by – layer deposition in Ar for 680 s.

The RBS results (table 6.2-2) were used to calibrate the magnetrons to obtain a film composition slightly Fe rich in agreement with the TTT diagrams reported in paragraph 1.2 [16]: the average stoichiometry for the layers is Fe:Pt = $(53 \pm 2):(47 \pm 2)$.

In Figure 6.12 the layers deposited in the two different discharges are compared by XRR.

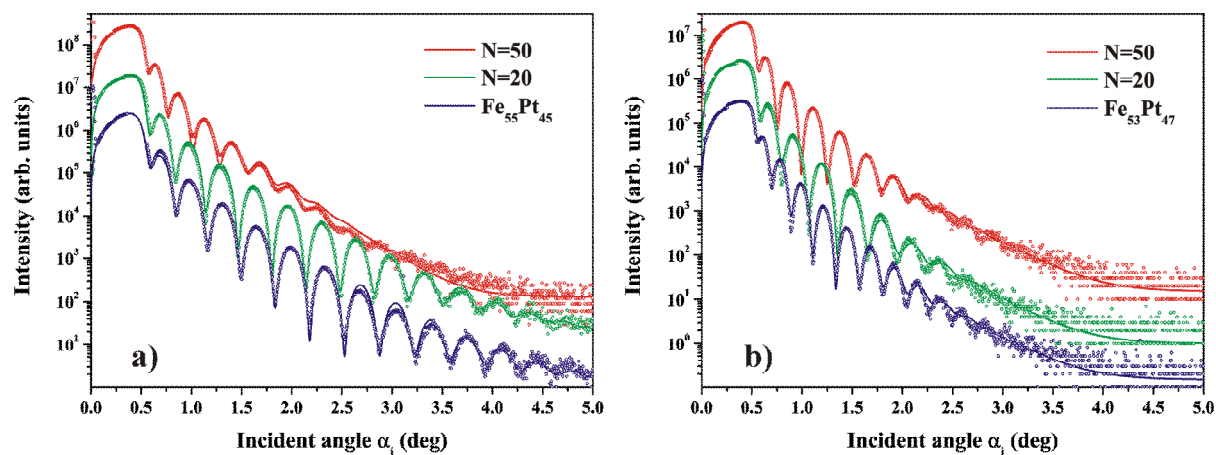


Figure 6.12: XRR: comparison between RT depositions a) in Ar and b) in Xe discharge (Intensities scaled for clarity).

To use Xe as sputtering gas had the effect to increase films surface roughness from 0.4 nm to 0.7 nm, in the co-depositions and the layer – by – layer methods with period $N = 20$. This is evidenced by the disappearing of the thickness oscillations fringes at lower incident angles for Xe assisted deposited layers (Figure 6.12-b: green and blue curves) than for Ar (Figure 6.12-a: green and blue curves). Surface roughness is further enhanced in layer – by – layer growing mode ($N = 50$), up to 1 nm, irrespective to the sputtering gas used. Independently from the discharge nature and the growing method, it is possible to identify the presence of a thin (~ 1 nm) surface layer (low frequency XRR beats) characterized by a lower density (between 50 and 70% of the bulk value), due to a partially oxidized surface.

The layers thicknesses measured by XRR are reported in the following table:

<i>Gas</i>	<i>Deposition technique</i>	<i>Thickness (nm)</i>
Ar	Co-sputtering	12.7
	MLs $N = 20$	12.5
	MLs $N = 50$	15.4
Xe	Co-sputtering	17.9
	MLs $N = 20$	14.0
	MLs $N = 50$	15.7

Table 6.2-3: Layers thickness by XRR.

In the case of multilayer sequence depositions, with $N = 50$, the single Fe/Pt slab has the thickness approximately of one atomic-layer.

As in the case of the films deposited on MgO, the low pressure (0.3 Pa) enhanced the layer density to values close to the bulk one; even if, layers grown in Xe discharges showed

density about $(86 \pm 2)\%$ of bulk value lower than that obtained using Ar as sputtering gas at $(95 \pm 2)\%$.

The superlattice peak was not detected, irrespective to the discharge gas, because of the high interface roughness.

In Figure 6.13 the GIXRD ($\alpha_i = 0.6^\circ$) are shown.

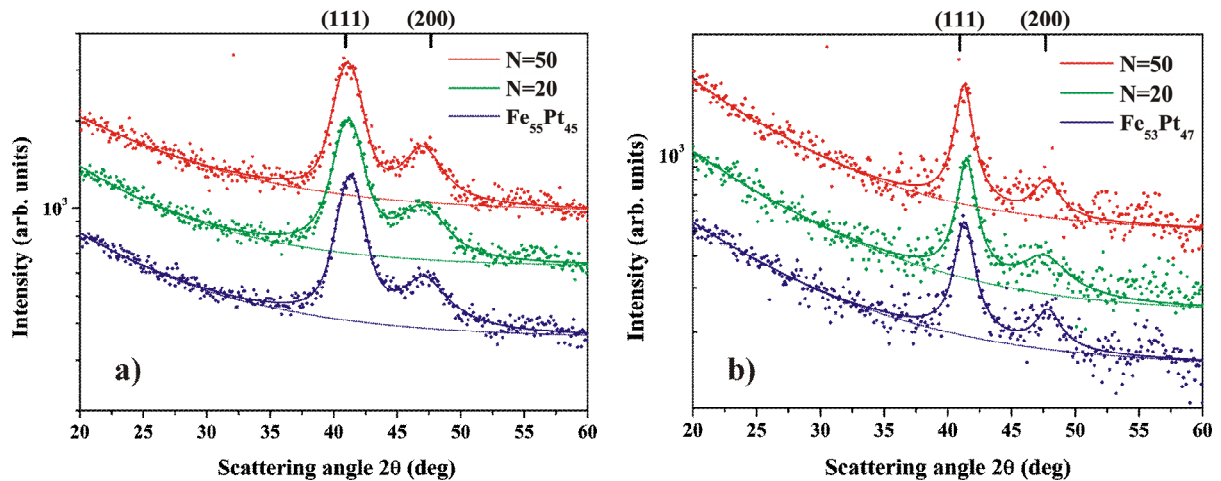


Figure 6.13: GIXRD ($\alpha_i = 0.6^\circ$): comparison between RT depositions a) in Ar and b) in Xe discharge (intensities are scaled for clarity).

Irrespective to the discharge nature or the deposition technique, the layers are in the disordered *AI* phase. It is easy to notice the smaller FWHM of the (111) peaks of the layers grown in Xe discharge. For the GIXRD data from the films grown in Ar the (111) peak FWHM is $(2.45 \pm 0.13)^\circ$, giving an average grain size of about 4 nm, independently from the deposition technique. In Xe depositions, the (111) peak FWHM slightly shrinks from the co-deposited layers to the multilayers sequence depositions giving an average grain size of at least 6 nm. Supposing an equal film thickness, it is possible to compare the absolute integral intensities of the (111) peak, the layer degree of crystallinity remains constant for all depositions independently from the gas discharge and the growing methodology applied. The average lattice constant, calculated from the reflection positions in GIXRD, is $a = (3.83 \pm 0.05) \text{ \AA}$, independently from the deposition technique or sputtering gas.

The magnetic properties of the as deposited layers are reported in Figure 6.14.

The hysteresis loops pointed out that the films are in the soft magnetic *AI* phase with in plane magnetic anisotropy, as a consequence of the shape anisotropy.

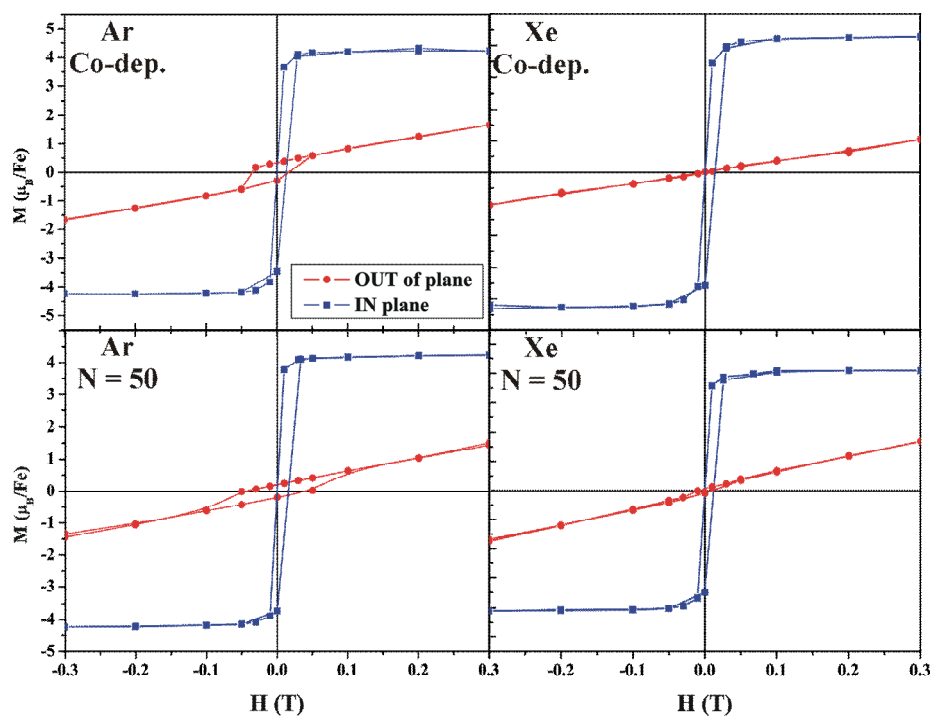


Figure 6.14: SQUID magnetometer measurements at RT: comparison between Ar discharges with a) co-deposited and b) layer – by – layer ($N = 50$) grown films and Xe discharges with c) co-deposited and d) layer – by – layer ($N = 50$) grown films.

The layers deposited with Ar as sputtering gas evidenced an increase of the out-of-plane coercivity, further enhanced to 0.05 T in the case of the layer – by – layer deposition. No difference was detected for the films produced in Xe discharges as function of the growing technique.

6.2.2.2. RTA at 550°C in Ar flow

The RT deposited layers were annealed in Ar flow by RTA at 550°C for 600 s: the whole campaign of X-ray scattering investigations, after annealing, is shown in figure 6.15. From the GIXRD spectra (Figure 6.15-a, b) it is not possible to evidence a significant difference between the layers produced with different techniques and discharges. In all cases all $L1_0$ reflections were detected. The disorder – order transformation took place during annealing, even if it was not observed a complete splitting of the (200)/(002) reflections, detected at lower temperature for the 70 nm layers.

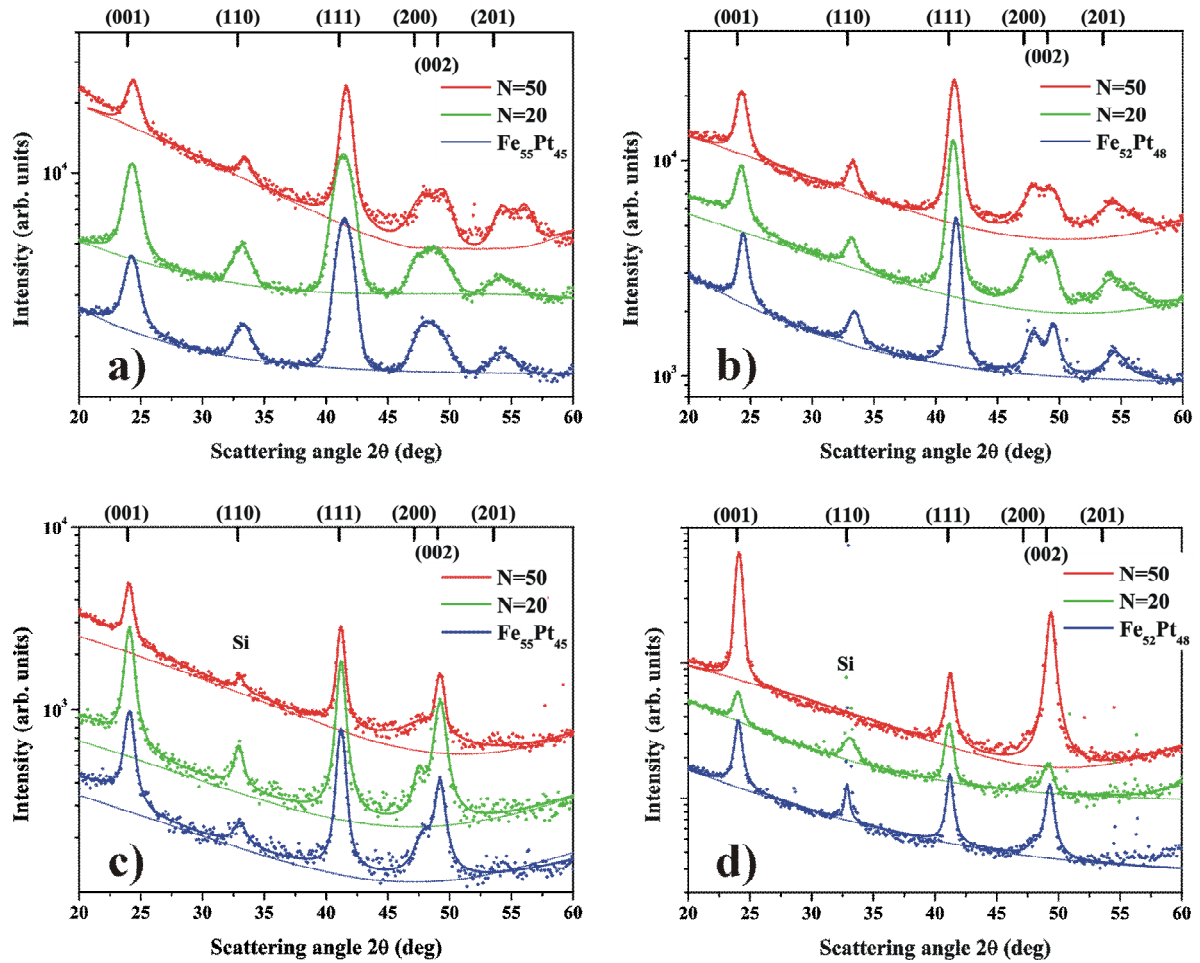


Figure 6.15: X-ray scattering analyses after RTA at 550°C for 600 s.

- GIXRD ($\alpha_i = 0.6^\circ$): a) Ar and b) Xe discharge
- $\omega - 2\theta$: c) Ar and d) Xe discharge

An immediate difference between the films grown in Ar discharge and those in Xe is the decrease of the (111) peak FWHM, as already evidenced by the investigations of the as-deposited films (Figure 6.13). In the patterns obtained from the layers deposited using Xe, the FWHM (111) = $(1.0 \pm 0.1)^\circ$ (instrument resolution $\sim 0.12^\circ$) giving an average grain size of about 9 nm. In the case of the films grown in Ar, the layers co-deposited and grown with multilayer period of $N = 20$ have an average grain size of 5 nm with a FWHM (111) = $(1.7 \pm 0.1)^\circ$. With the monolayer-like deposition, in Ar, the film is characterized by an average grain size of 7 nm, FWHM (111) = $(1. \pm 0.1)^\circ$.

The clear presence of all Ll_0 reflections in GIXRD and in $\omega - 2\theta$ (Figure 6.15-c, d) evidences a low degree of (001) preferential orientation in all layers. This can be analyzed comparing the ratio between the integrated intensities of the (001) and (111) peaks in GIXRD and $\omega - 2\theta$ and its variation as function of the growth technique and discharge characteristic. In fact, in the GIXRD geometry it is possible to detect reflections from planes having not the same orientation as the substrate, while, in the $\omega - 2\theta$ set-up, the signals arise only from those planes parallel to the Si(001). Therefore, an increase of $A(001)/A(111)$ in the $\omega - 2\theta$ geometry, together with a decrease in the GIXRD patterns is a

clear indication of the degree of (001) preferential orientation of the film. The results are reported in the table 6.2-4.

<i>Gas</i>	<i>Deposition technique</i>	<i>A(001)/A(111)</i>	
		<i>GIXRD</i>	<i>ω-2θ</i>
Ar	Co-sputtering	0.5	0.6
	MLs $N = 20$	0.7	1.7
	MLs $N = 50$	0.6	1.3
Xe	Co-sputtering	0.6	2.7
	MLs $N = 20$	0.5	1.3
	MLs $N = 50$	0.6	7.2

Table 6.2-4: Comparison between the $A(001)/A(111)$ from GIXRD and ω -2 θ patterns

In the GIXRD patterns it is not detected a strong change in the $A(001)/A(111)$ as a function of the discharge gas or the deposition technique. On the contrary, in the ω -2 θ patterns, from layers deposited in Ar discharge (Figure 6.15-c), the $A(001)/A(111)$ is enhanced in the growths by multilayer method with period to $N = 20$. In Xe discharges (Figure 6.15-d), $A(001)/A(111)$ is strongly increased by the monolayer sequence deposition ($N = 50$) to $A(001)/A(111) = 7.2$. Computing the FWHMs of the spectra obtained in the ω -2 θ geometry, it is possible to obtain the out-of-plane grain size. No correlation was found between the deposition techniques or the gas discharge and the out-of-plane grain size, the average value is (13 ± 1) nm, coincident with the layer thickness.

The importance of the deposition technique in Xe discharges is further confirmed by the rocking curves around the (001) and (002) peaks, reported in figure 6.16. Evaluating the FWHM of the (001) and the (002) peaks along Q_x , it is possible to calculate the degree of layer mosaicity and the in-plane grain size. The angular distributions around the (001) peak are reported in the table 6.2-5.

<i>Gas</i>	<i>Mode</i>	<i>Mosaicity (deg)</i>
Ar	co-deposition	-
	$N = 20$	16
	$N = 50$	7
Xe	co-deposition	-
	$N = 20$	13
	$N = 50$	5

Table 6.2-5: Angular dispersion around the (001).

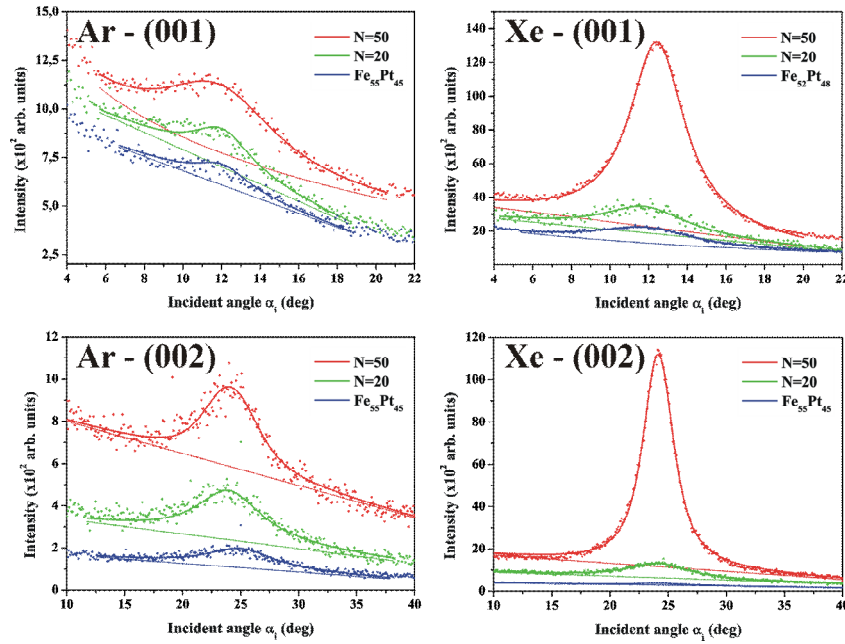


Figure 6.16: Rocking curves around the (001) and (002) reflections.

Independently from the gas discharge, the rocking curve peak to noise ratio is strongly enhanced by the monolayer-like sequence deposition ($N = 50$). Assuming the same layer thickness and considering the peak integral area as a direct indication of the amount of scattering centres (paragraph 4.2.2), it is evident the increase of the (001) oriented fraction from the co-deposition to the layer – by – layer growth technique: $A(\text{multilayer } N = 50)/A(\text{co-deposition}) \approx 4.5$. The use of Ar as sputtering gas is not supporting the layer final orientation; on the contrary, depositing in Xe discharges is lowering the angular distribution of the scattering planes around the (001) preferential orientation. It was possible to evaluate the film LRO only for the layer grown in Xe discharge by the layer – by – layer method with $N = 50$: the LI_0 transformation is complete giving an S parameter equal to 0.98.

No influence of the deposition technique or discharge was found on the lattice constants. The calculated values [149] are $a = (3.81 \pm 0.02) \text{ \AA}$ and $c = (3.68 \pm 0.04) \text{ \AA}$: the resulting crystal cell is a contraction only along the c axis of about 3.9% of the initial *fcc* lattice of the *Al* phase of the as-deposited films.

The SQUID $M - H$ loops for the specimen deposited at RT and subsequently rapid thermal annealed at 550°C are reported in Figure 6.17.

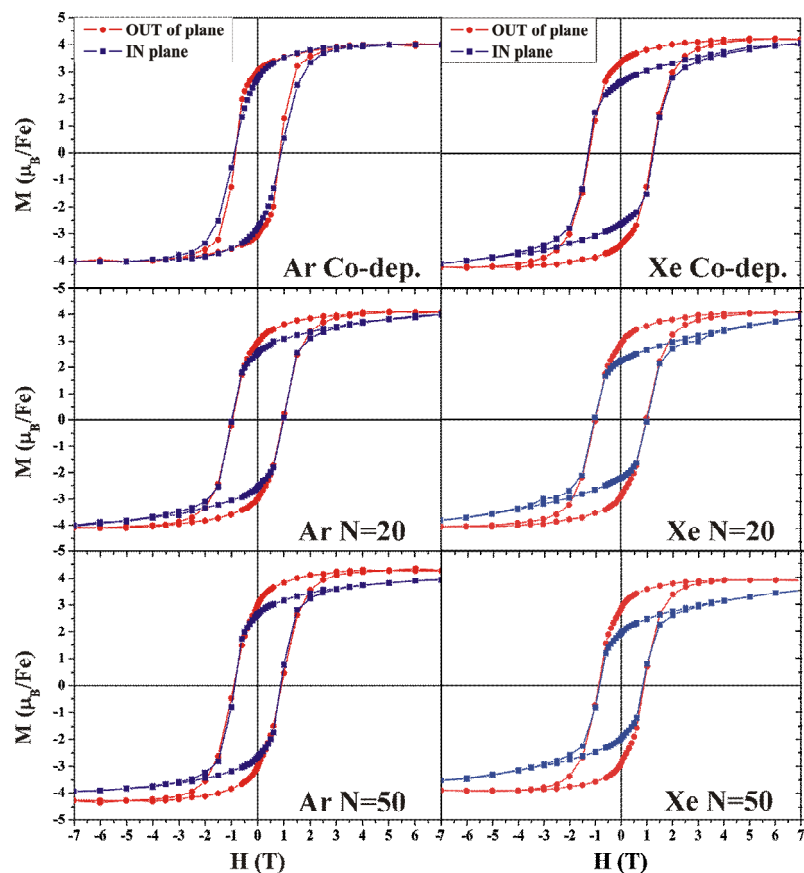


Figure 6.17: SQUID $M - H$ loops after RTA at 550°C : comparison between Ar discharges (left side) and Xe discharges (right side) with co-deposited and layer – by – layer ($N = 20, 50$) grown films.

Despite the high annealing temperature, the magnetic hysteresis loops have a smooth slope and a huge coercivity indicating a material with defects [146]. The out of plane orientation of the easy axis is enhanced by the deposition in the layer – by – layer mode, independently from the sputtering gas applied. In Ar discharges, the in-plane S_q decreased from 0.8 to 0.6 in Ar discharge. No change in the coercive field was detected: it remained stable to $\sim 1\text{T}$ irrespective to the deposition technique. For Xe deposited layers the in plane S_q decreased only from 0.7 to 0.5, in agreement with the better (001) preferential orientation of the film grown by multilayer sequence with $N = 50$. A further confirmation of the influence of the sputtering gas was found for the layers produced in Xe discharge. The decrease of the coercive field from 1.3 T for the co-deposition to 0.85 T for the layer – by – layers mode with period $N = 50$ indicating an enhancement of magnetic coupling between the grains.

6.2.2.3. Annealing at 700°C in vacuum

To investigate the effect of the annealing atmosphere and temperature, RT deposited layers were annealed in vacuum at 700°C for 600 s. The X-ray investigations, performed after annealing, are reported in Figure 6.18.

From the GIXRD and the $\omega - 2\theta$ investigations (Figure 6.18-a, b and c, d) all layers are in the LI_0 ordered phase, confirmed by the appearance of the superstructure reflections. In GIXRD (Figure 6.18-a, b) patterns it is possible to note the splitting of the (200)/(002) reflections, with a predominance of the (002) peak on the (200) in GIXRD and a complete disappear of the (200) peak in the $\omega - 2\theta$ geometry (Figure 6.18-c, d).

The GIXRD data (Figure 6.18-a, b) showed the same trend of the (111) FWHM, observed after annealing at 550°. The layer grain size increases when film growth is performed in Xe discharges to ~12 nm. The average grain size of films deposited in Ar is about 7 nm. From the (001) FWHMs of the $\omega - 2\theta$ patterns, the out-of-plane grain size was estimated at (15 ± 3) nm, close to the total layer thickness independently from the deposition conditions.

To firstly evaluate the effect of the deposition parameters on the (001) film preferential orientation, the $A(001)/A(111)$ values from the GIXRD and the $\omega - 2\theta$ spectra were computed and compared (table 6.2-6).

<i>Gas</i>	<i>Deposition technique</i>	<i>A(001)/A(111)</i>	
		<i>GIXRD</i>	<i>$\omega-2\theta$</i>
Ar	Co-sputtering	0.8	2.9
	MLs $N = 20$	0.9	3.5
	MLs $N = 50$	1.4	2.4
Xe	Co-sputtering	0.9	6.1
	MLs $N = 20$	1.0	8.7
	MLs $N = 50$	-	-

Table 6.2-6: Comparison between the $A(001)/A(111)$ from GIXRD and $\omega-2\theta$ patterns

From the film grown by the monolayer-like technique in Xe, it was observed a shift of the (111) peak, in GIXRD geometry (Figure 6.18-a), to higher scattering angles, due to diffuse scattering from the (220) Si peak overlapping the (111) LI_0 reflection altering its evaluation.

In the $\omega - 2\theta$ patterns, from layers deposited in Ar discharge (Figure 6.18-c), no sharp increase of the $A(001)/A(111)$ with the growing technique was detected. In Xe discharges (Figure 6.18-d), it was observed a complete disappearing of the signal from the (111) planes in the $\omega - 2\theta$ pattern from the layer - by - layer growing mode with $N = 50$, together with a strong enhancement of the $A(001)/A(111)$.

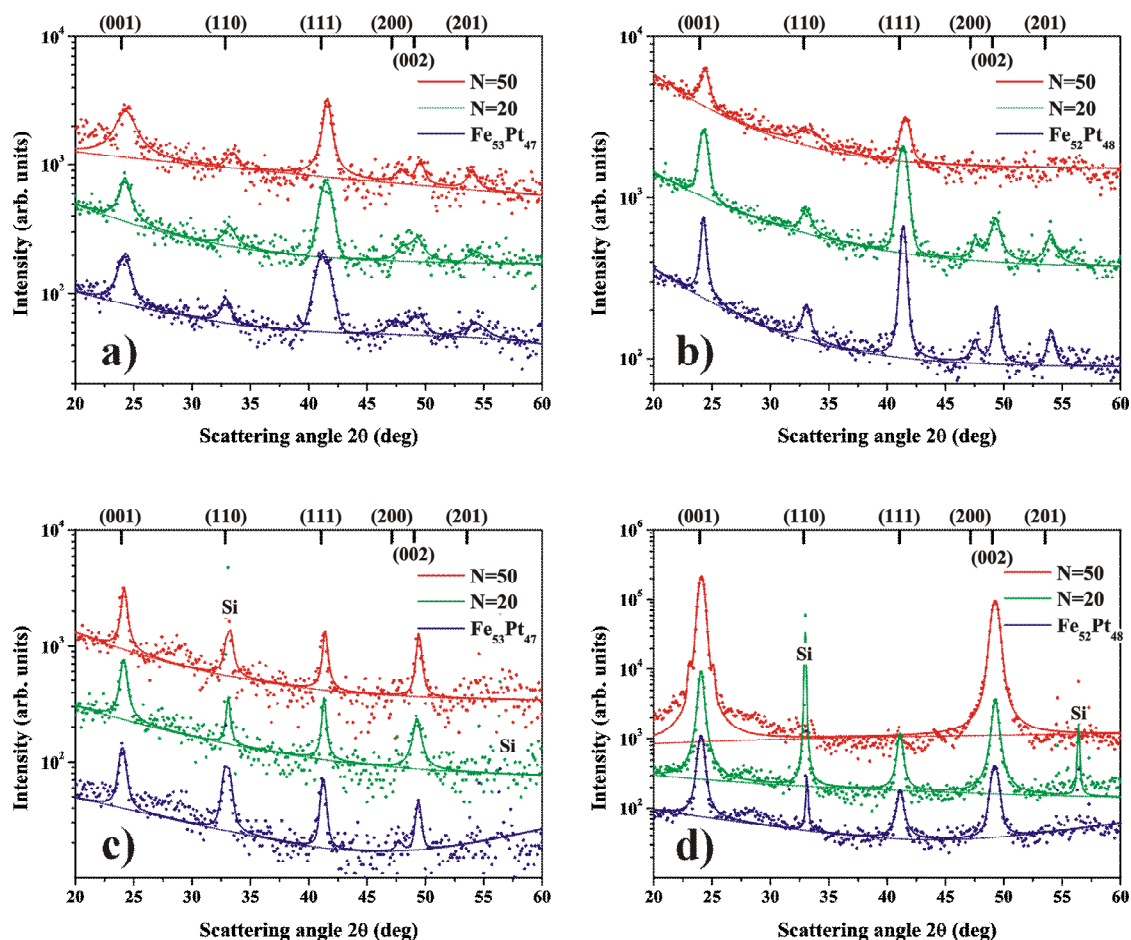


Figure 6.18: X-ray scattering analyses after vacuum annealing at 700°C for 600 s.: GIXRD ($\alpha_i = 0.6^\circ$): a) Ar and b) Xe discharge; $\omega - 2\theta$: c) Ar and d) Xe discharge

It is possible to recognize thickness fringes around the (001) peak in the $\omega - 2\theta$ spectra from the film deposited in Xe by the layer – by – layer technique with $N = 50$ (Figure 6.18-d, red curve), confirming the high degree of crystallinity and a sharp interface between layer and substrate, as already found in highly oriented (001) FePt layers on MgO (001) (paragraph 6.1.2).

Comparing the integral area of the (001) peak, in the $\omega - 2\theta$ spectra (Figure 6.18-c, d), from the co-deposited film and those grown by the layer – by – layer mode with $N = 50$, the amount of (001) oriented LI_0 fraction was evaluated, supposing an equal layer thickness. In Ar discharges $A(\text{multilayer } N = 50)/A(\text{co-deposition}) \approx 1$ and significantly increases in Xe assisted depositions: $A(\text{multilayer } N = 50)/A(\text{co-deposition}) = 9$. This means that the change from a deposition technique to another one is influencing the amount of (001) oriented scattering centres only in films grown in Xe discharges. These results must be compared with the FWHM of the rocking curves around the (001) peak.

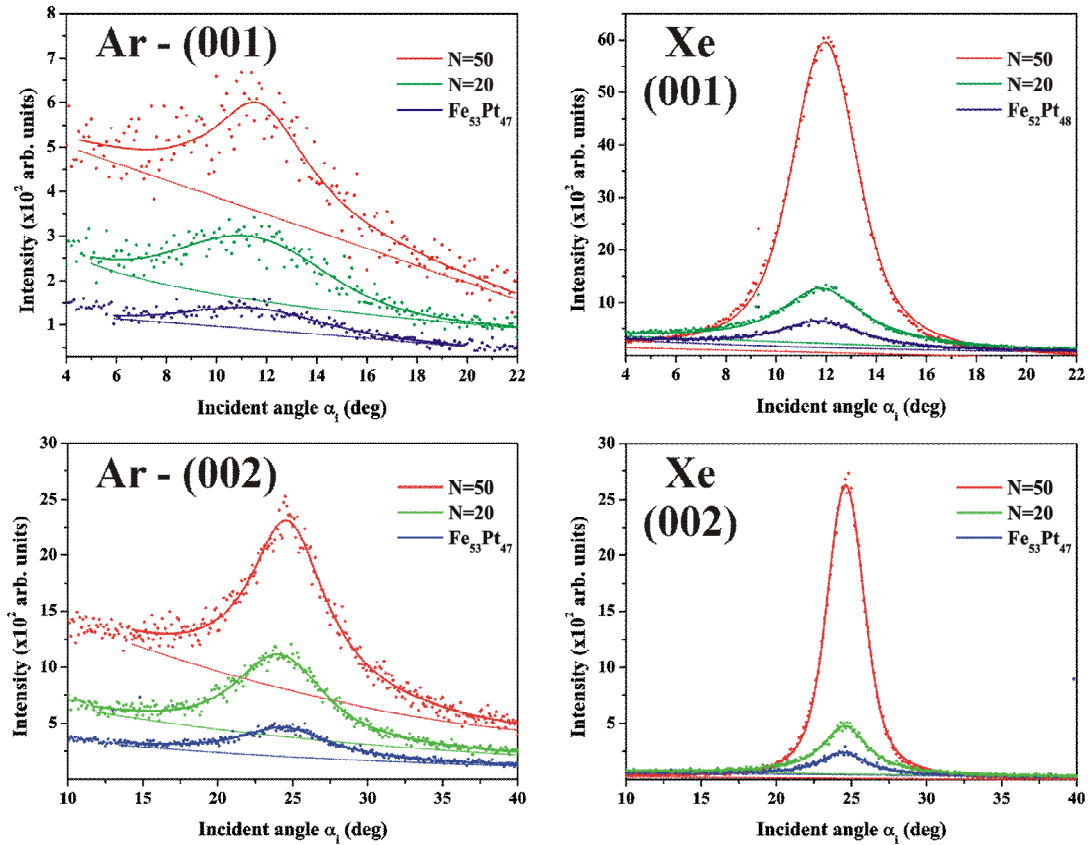


Figure 6.19: Rocking curves around the (001) and (002) directions.

The rocking curve FWHMs (Figure 6.19) is the sum of the contributions from the angular dispersion of the (001) planes around the surface normal and the lateral grain sizes (paragraph 4.2.2). By combining the FWHMs in Q_x from the (001) and the (002) peaks it is possible to divide these two contributions, the results are reported in table 6.2-7.

<i>Gas</i>	<i>Mode</i>	<i>Mosaicity (deg)</i>
Ar	co-deposition	10
	$N = 20$	9
	$N = 50$	9
Xe	co-deposition	7
	$N = 20$	6
	$N = 50$	5

Table 6.2-7: Angular dispersion around the (001).

As already noticed for the film after RTA, using Ar as sputtering gas is not significantly supporting the layer orientation (Figure 6.19-left side). In this discharge, the lower degree of mosaicity was detected for the layer – by – layer deposition with $N = 50$ with an angular dispersion of about 9° . In comparison, the films deposited in Xe discharge have in average a higher degree of (001) preferential orientation (Figure 6.19-right side). The layer

deposited in Xe discharge with the monolayer-like technique ($N = 50$) showed a strong (001) preferential orientation, confirmed by an angular dispersion of the (001) planes around the out of plane direction of 5° .

It was possible to calculate the S parameter only in the case of the film grown in Xe by the layer – by – layer method with $N = 50$: this is equal to 0.98 proving a high degree of LRO in the film after annealing

No correlation between the deposition technique and the gas discharge was found on the lattice constants. As already noticed in the layers after RTA, the lattice parameter a remained approximately equal, $a = (3.82 \pm 0.02) \text{ \AA}$, to the AI average value (paragraph 6.2.2.1); on the contrary, it was measured a strong contraction of 4.1% along the c axis to $(3.67 \pm 0.03) \text{ \AA}$.

The SQUID magnetometer hysteresis loops for are reported in Figure 6.20.

The results from the X-ray scattering investigations are completely confirmed by the film magnetic properties. The high coercive field and the smooth slope of the H - M curves evidence a layer structure characterized by the presence of defects preventing domain walls motion. The only exception is the film grown in Xe with a multilayer period $N = 50$.

The layers deposited in Ar discharges (Figure 6.20-left side) showed a weak alignment of the magnetization easy axis with the surface normal. The out-of-plane magnetic anisotropy is only slightly enhanced by the monolayer-like growth. The higher magnetic coupling between grains was found for the film deposited with the layer – by – layer technique, having $H_C = 1.2 \text{ T}$ in comparison with $H_C = 1.5 \text{ T}$ for the specimens obtained by the other two growth methodologies.

Similar magnetic properties are obtained for the film grown by co-sputtering in Xe discharge (Figure 6.20-right side). Changing the deposition technique to the layer – by – layer mode provided an increase of the out-of-plane magnetic anisotropy. In the case of Xe deposition with a period of $N = 50$, the magnetization easy axis lied completely in the out of plane direction while the in-plane saturation magnetization M_S was hardly reached at 7 T. The fast transition between positive and negative magnetization and $M_S \approx M_R$ ($S_q \sim 1$) indicated a film without defects, with magnetically coupled grains. The coercive field is therefore reduced to 0.5 T.

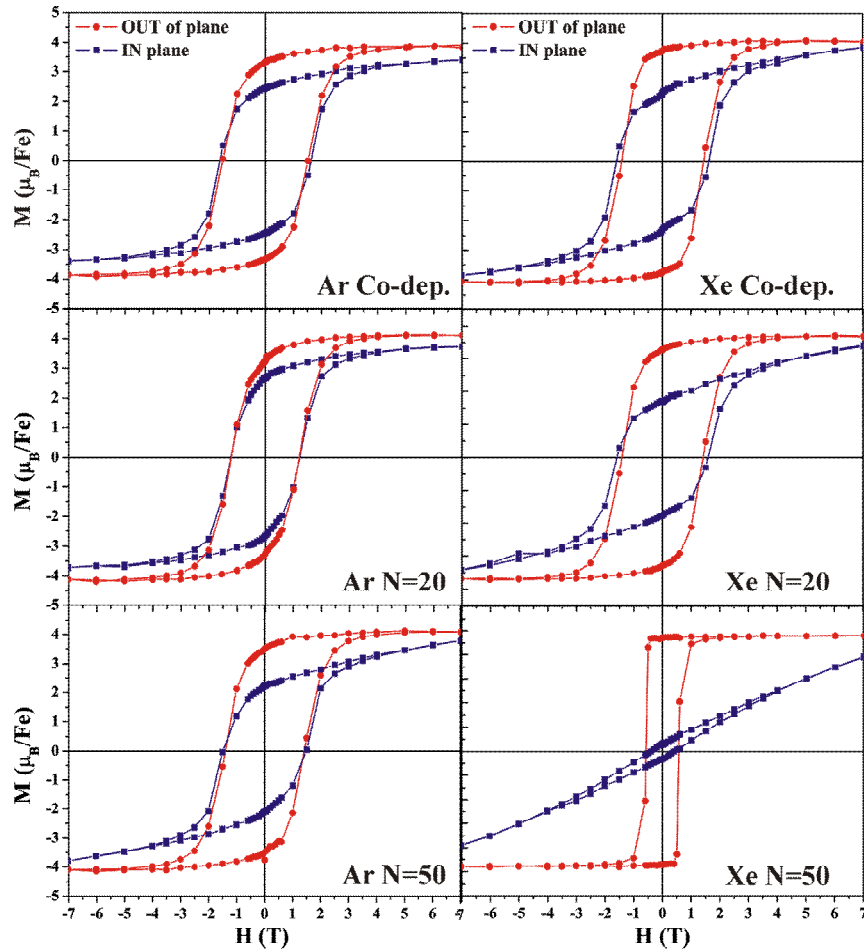


Figure 6.20: SQUID magnetometer measurements after vacuum annealing at 700°C for 600 s: comparison between Ar discharges (left side) and Xe discharges (right side) with co-deposited and layer – by – layer ($N = 20, 50$) grown films.

6.2.2.4. Summary of the results

Before proceeding in the data interpretation, it could be useful to summarize the obtained results as function of the gas discharge, growing mode and annealing conditions.

As deposited layers:

No strong differences were detected between the layer characteristics as a function of the deposition conditions. The films are all in the soft ferromagnetic phase $A1$. Growths in Xe discharge slightly support larger grain size. The monolayer sequence deposition technique is enhancing film surface roughness.

RTA at 550°C in Ar flow:

- the $A1$ to $L1_0$ transformation occurred for all layers, with a contraction of the only c axis, while the a axis remained almost unchanged;
- Ar discharge is not supporting the final (001) preferential orientation,
- layers grown in Xe discharges showed a higher fraction of (001) oriented scattering centers,

- the layer – by – layer deposition technique is decreasing the film mosaicity, irrespective to the sputtering gas,
- the influence of the deposition technique is more pronounced in layer grown in Xe discharge than in Ar,
- the *M-H* curves confirm the X-ray investigation results: the out-of-plane orientation of the magnetization easy axis is enhanced in films deposited with Xe and by the layer – by – layer method
- films deposited in Xe show a higher degree of crystallinity and therefore a lower coercive field in comparison to layers grown in Ar

Annealing at 700°C in vacuum:

The thermal treatment at higher temperature is enhancing the differences, already noticed after RTA, between the films grown in Ar discharges and those deposited using Xe as sputtering gas. The layer –by – layer growths is strongly supporting the (001) preferential orientation and become fundamental to obtain a highly oriented layer in depositions with Xe.

On the contrary, Ar assisted growths do not provide layers having properties increased by the higher annealing temperature, in particular, the layer preferential orientation is not strongly improved with respect to the RTA at 550°C.

6.2.3. Discussion

The used sputtering gases, Ar and Xe, have a significantly difference in mass and atomic radius, it was, therefore, expected a strong impact on the layers physical properties. The higher surface roughness, of the as deposited films, is explained with a higher momentum transfer from the Xe atoms impacting the surface to the Fe and Pt atoms composing the growing layer; while, as already discussed in paragraph 5.3, the high energetic atoms impacting the substrate during Ar assisted depositions is supporting atomic rearrangement during growth and producing a smoother surface. Also from the magnetic properties point of view, Ar depositions result in a more isotropic layer characterised by an increasing the out-of-plane magnetic coercivity with respect to the Xe grown films.

After annealing at 550°C the *AI* to *LI₀* phase transformation occurred, independently from the gas discharge. The effect of an amorphous substrate manifests itself in the value of the *LI₀* lattice constants after annealing. In both thermal processes, RTA and vacuum annealing, it was not observed a dilatation along the *a* axis in the *AI* to *LI₀* transformation. The tetragonal distortion is realized mainly by a strong contraction (up to 4%) along the *c* axis.

The effect of the vacancies formation occurring in Ar discharges does not further enhance the *LI₀* fraction, in comparison with the films grown in Xe, where, on the contrary, the deposition technique started to play a fundamental role. As explained in paragraph 1.3, sequential deposition of Fe and Pt creating a structure that emulates the desired *LI₀* should

not only decrease the phase transformation temperature but strongly enhance the (001) preferential orientation. But from our results the importance of the deposition mode is mainly evident in Xe assisted depositions. The average energy of the Ar atoms impacting the substrate is 89 eV (paragraph 5.3) that is enough to cause a vertical material intermixing during growth suppressing the DSRO which is fundamental for developing a (001) preferential orientation [35]. To compare these results with Xe depositions, the energy impacting the substrate must be computed also in Xe discharges. The results of TRIDYN simulation are shown in figure 6.21, supposing an initial Xe ion energy of 400 eV.

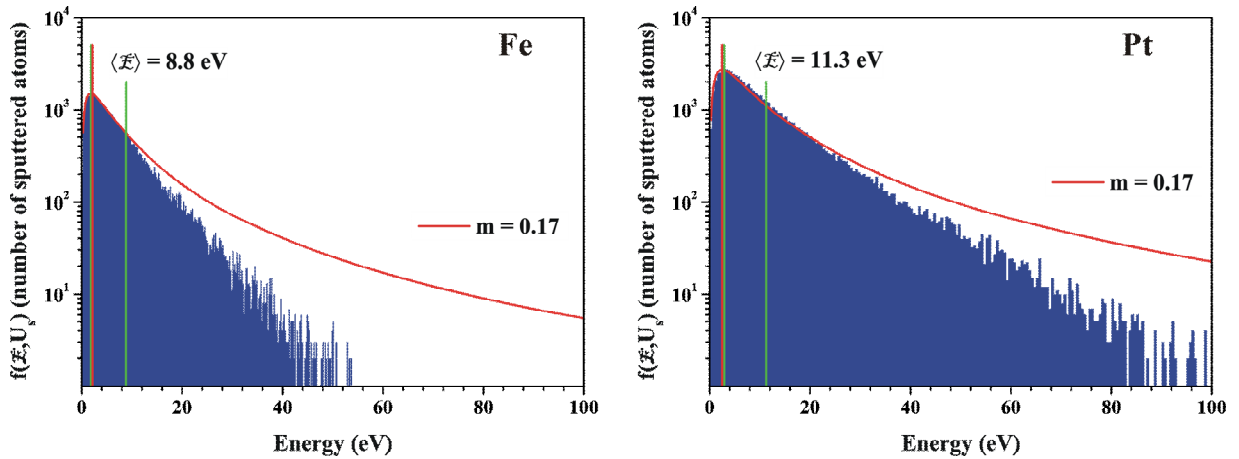


Figure 6.21: Energy distribution of the sputtered particles: Fe (left side) and Pt (right side).

The energy distribution was simulated with the modified Thompson distribution function of equation (2.15) with $m = 0.17$. The energy tails of the distributions are not well described, but the modified Thompson function with $m = 0.17$ is in good agreement with the center of the distribution. The maximum number of Fe atoms is sputtered with an energy of 1.8 eV. The distribution mean energy, calculated according equation (2.16) is 8.8 eV; the sputtering yield is $y_{sp} = 0.60$ at/ion. The maximum fraction of Pt atom is sputtered at the energy of 2.5 eV, with $y_{sp} = 0.70$ at/ion, but the distribution mean value is at 11.3 eV. It should be noticed that the maximum energy of the sputtered Fe atoms is 71 eV while for Pt is 124 eV. The calculation of the atom mean free paths and the average atom energies impacting the substrate were accomplished according the procedure described in paragraph 2.4, supposing an initial average energy, at the target, of $\langle E \rangle_{Fe} = 8.8 \text{ eV}$ $\langle E \rangle_{Pt} = 11.3 \text{ eV}$. The results are reported in Figure 6.22.

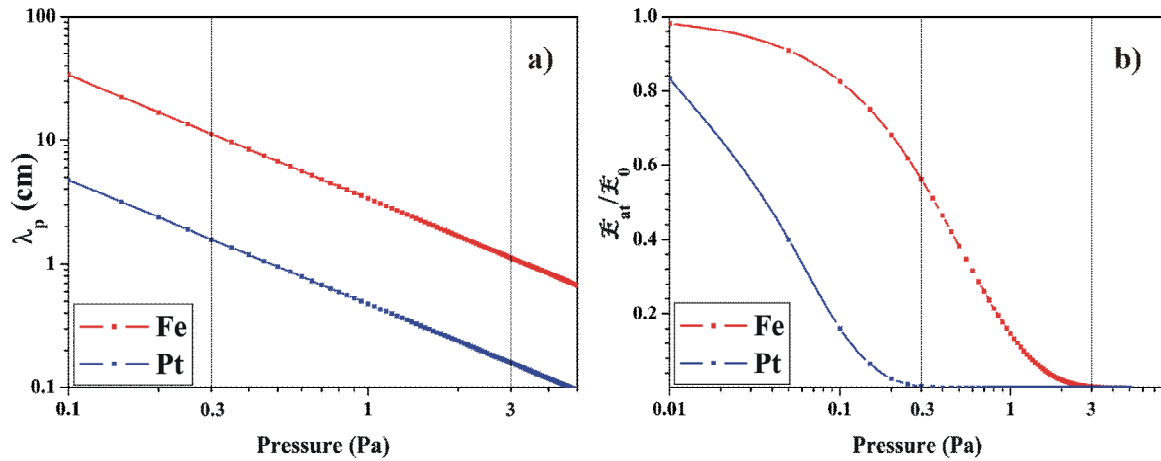


Figure 6.22: Mean free path (a) and energy decrease (b) for Fe and for Pt, as a function of the deposition pressure. The initial energy is $\langle E \rangle_{Fe} = 8.8$ eV and $\langle E \rangle_{Pt} = 11.3$ eV.

The calculated mean free path λ_p is 11.23 cm and 1.58 cm for Fe and Pt, respectively. The average sputtered atom energy at the substrate, after travelling the distance $d = 10$ cm (Figure 6.22), is 4.9 eV for Fe and 0.4 eV for Pt. Fe energy is therefore sufficient to support adatom mobility during layer growth (paragraph 2.5), while the sputtered Pt atoms are completely thermalized. In Figure 6.23 the backscattering yield and the mean energy of the Xe neutrals, reflected from the Fe and Pt targets, are reported. Reflection from the Fe target is impossible due to $m_{Xe} \gg m_{Fe}$.

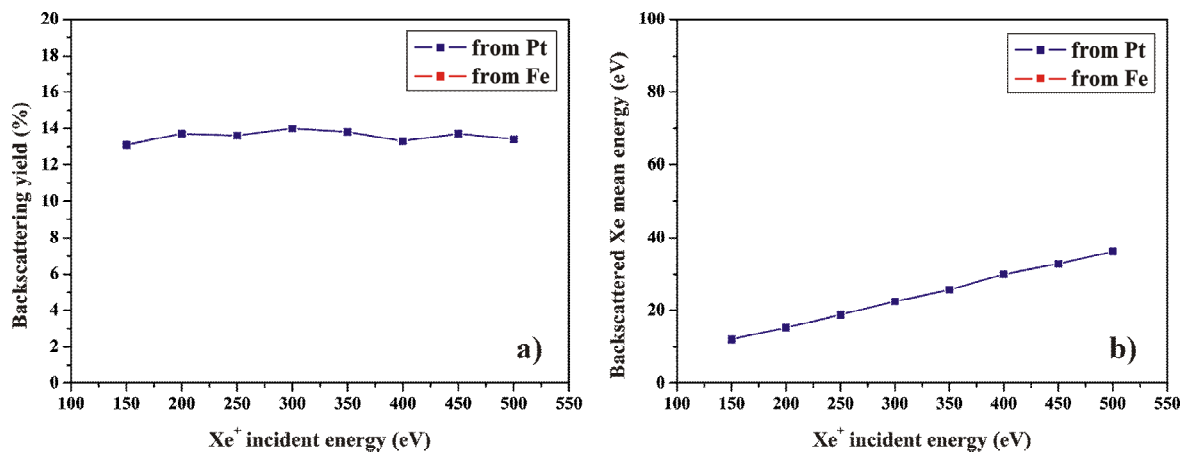


Figure 6.23: The backscattering yield (a) and the mean energy (b) of the Xe atoms at the target, calculated with TRIDYN, as a function of the Xe ion incident energies.

Only 13% of the total Xe ions are reflected by the Pt target with a mean energy of 30.0 eV in comparison with the Ar assisted depositions where 36% of the total ions were backscattered with a mean energy of 128 eV.

In Figure 6.24, the Xe contribution to the energy impacting the substrate is shown, calculated according to the model described in paragraph 2.4.

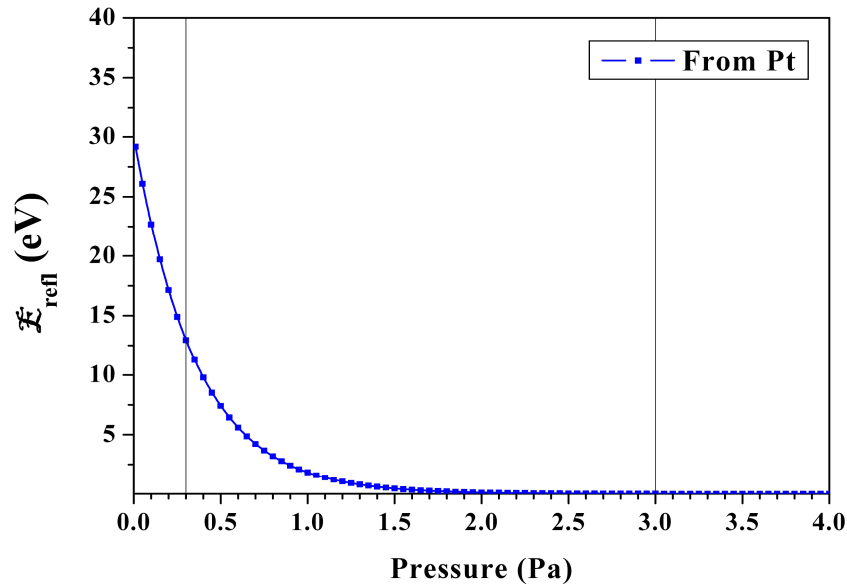


Figure 6.24: Backscattered Xe energy contribution to the energy impacting the substrate during deposition.

The average energy of the Xe neutrals is strongly reduced at the substrate at 13 eV, which cannot cause a significant material intermixing during growth preserving the DSRO area constructed by layer – by – layer deposition technique.

In disagreement with other studies [10, 40, 42, 58] it was surprising that even for the films grown in Xe discharges, it was not possible to obtain a complete (001) preferential orientation after RTA at 550°C. According to [42], the annealing temperature determines the LI_0 fraction in the layer, while the annealing time influences the degree of orientation. They indicated in 600 s an optimum annealing time to support layer orientation. But it must be remembered that, in our experiment, the RTA process was performed with the specimen in the up-side-down position and in Ar flow and the temperature was monitored with a thermocouple touching the sample corner. It is therefore extremely probable that the “real” annealing temperature, seen by the layer, was lower than the indicated value. Annealing in vacuum is preferable to support the layer (001) orientation, avoiding any risk of oxidation of the surface Fe. 700°C is definitely a high annealing temperature, but also in this case the degree of mosaicity is still high in comparison with films grown in Xe discharges by the same deposition techniques. We, therefore suppose that Ar assisted depositions provide layers in which the DSRO area amount is strongly decreased by the energetic atoms impacting the substrate during growth.

The highest preferential orientation was obtained when the deposition is performed by nearly monoatomic layers, for both discharges. In this case, the multilayers already emulate an ordered (001) LI_0 phase. During subsequent annealing the atoms need only to move slightly to obtain the *fcc* structure. This preserves the orientation prescribed by the multilayer geometry, namely (001). In the case of the specimen with greater bilayer thickness, however, the atoms of each layer must undergo longer random walks to achieve LI_0 phase, losing the original pattern of the growth structure.

The magnetic properties are in perfect agreement with the X-ray scattering results: a strong (001) magnetic anisotropy was achieved only from a Xe-assisted deposition in a monolayer-like sequence deposition. In this case it was observed a higher magnetic coupling between the grains because of a higher degree of crystallinity in the layer, as evidenced by the presence of the thickness fringes (Figure 6.18-d).

6.2.4. Summary and conclusions

The LI_0 (001) preferential orientation was investigated for FePt films (~ 14 nm) deposited on amorphous SiO_2 as a function of the gas discharge, growing methodology and the annealing conditions.

The FePt layers grown in Ar discharges at 0.3 Pa showed a weak (001) preferential orientation after RTA at 550°C or vacuum annealing at 700°C. The deposition method, co-sputtering or multilayer sequence deposition, is only slightly influencing the final (001) layer orientation after annealing. At both annealing temperatures the order transformation is achieved confirmed by the magnetic property measurements of high coercive fields $H_C = 1.5$ T (Figure 6.17 and Figure 6.20, left side).

Xe assisted depositions produced layers with a higher degree of (001) orientation after annealing. The growing technique is strongly influencing the film (001) orientation: the highest degree of orientation was achieved after vacuum annealing from the layer grown by the monoatomic layer sequence method. In this case, the coercivity is decreased from 1.5 T, of the film grown by co-deposition, to 0.5 T (Figure 6.20-right side).

Computing the energy impacting the substrate by TRIDYN simulations and analytical calculations it was found that while in Ar discharges Fe and Pt will reach the substrate with an average energy of ~ 5 eV, Ar reflected neutrals have a high mean energy ~ 89 eV. The high energetic contribution is completely suppressed in Xe discharges. The Xe reflected atoms impact the substrate with an average energy of 13 eV that preserve the DSRO area, created by the monolayer-like sequence deposition, fundamental for the (001) orientation.

To create a high degree of (001) in the layer, after annealing, it is essential to emulate the (001) LI_0 . Thus, energetic particles impacts must be suppressed to avoid strong material intermixing during growth.

7. FePt nanoclusters

7.1. The effect of the sputtering gas and the deposition pressure on clusters formation

It will be reported about the effect of the sputtering gases, Ar and Xe, on FePt clusters formation by magnetron sputtering deposition at high working pressures and subsequent annealing by RTA at 550°C for 600 s. This study was published in *Journal of Applied Physics* 105, 07B529 (2009)

Yuji Itoh *et al.* [76, 77] described the deposition of Fe/Pt at 1.2 Pa in Ar: controlling the layer thickness, they produced particulate layers or nanoislands, after RTA at 500°C for 1 s. From a 2 nm bi-layer system they observed the formation of 17 nm grains embedded into the SiO buffer layer, having a coercive field $H_C = 40$ kOe and magnetic moments oriented perpendicular to the sample surface.

As already described in paragraph 2.5, the layer morphology and structure are strongly influenced by the deposition conditions: an increase of the working pressure will lead to layers composed by crystal agglomerates, separated by void defects, as a consequence of the increase of the oblique component in the plasma flux and an enhancement of the shadowing effect at the substrate.

The two different layer deposition methods (co- and layer – by – layer deposition) will be here also compared. The latter is expected to be suitable to increase the LI_0 fraction after annealing by reducing the element diffusion paths inside a unit cell size and to support the *c*-axis orientation parallel to the surface normal [42].

7.1.1. Experimental parameters

FePt was deposited on *a*-SiO₂ (500nm) / Si (100) substrates. The growths are realised at 3 Pa. This high deposition pressure was chosen in order to increase clusters formation already at the layer growing stage. The base pressure was below 5×10^{-5} Pa and 22 sccm Ar or 26 sccm Xe were injected to reach 3 Pa. The magnetrons run with power of 40 W and 4 W in Ar discharges for Fe and Pt respectively. In Xe discharges, the magnetron power was increased to 44 W for Fe and 4 W for Pt. The subsequent annealing is performed in the rapid thermal processing facility, described in paragraph 3.3.3, in Ar flow at 550°C for 600 s (100°C/s). XRR, surface diffuse X-ray scattering at $2\theta = 2^\circ$ and GIXRD, at incident angle $\alpha_i = 0.6^\circ$, are accomplished by D5005 Siemens-Bruker diffractometer (Cu - $K\alpha$, paragraph 4.2.4). The magnetic properties are studied by SQUID at 300K.

7.1.2. Results

Every sample is investigated by RBS at an incident angle of 70° for layer chemical composition. The atom deposition rate can be averaged at $(9.18 \pm 0.78) \times 10^{16}$ at/cm²s and $(7.74 \pm 0.37) \times 10^{16}$ at/cm²s for Fe and Pt, respectively, in Ar assisted depositions. In Xe discharges, these value are calculated at $(4.52 \pm 0.43) \times 10^{16}$ at/cm²s for Fe and $(3.69 \pm 0.20) \times 10^{16}$ at/cm²s for Pt, roughly half of the corresponding deposition rates obtained in Ar: in fact the sputtering yield is reduced in Xe. Assuming closed-packed crystalline density values, a minimum film thickness Δ_{RBS} (Table 7- 1) can be calculated.

<i>Deposition conditions</i>	<i>Composition</i>	Δ_{RBS} (nm)	Δ_{XRR} (nm)
A1 – Co-deposition with Ar	Fe ₅₄ Pt ₄₆	3.3	5.1
A2 - Co-deposition with Ar	Fe ₅₆ Pt ₄₄	5.1	7.8
A3 – Layer-by-layer deposition with Ar	[Fe(1.3Å)/Pt(1.5Å)] ₂₀	5.6	9.2
X1 - Co deposition with Xe	Fe ₅₃ Pt ₄₇	2.9	5.2
X2 - Co deposition with Xe	Fe ₅₃ Pt ₄₇	5.7	12.0
X3 – Layer-by-layer deposition with Xe	[Fe(1.3Å)/Pt(1.4Å)] ₂₀	5.4	10.5

Table 7- 1: List of the investigated grown conditions and comparison between as-deposited layers composition and thickness t from RBS and XRR results

In Figure 7.1, it is reported the comparison between RBS measurements as a function of the gas discharge for layers grown in the layer – by – layer mode.

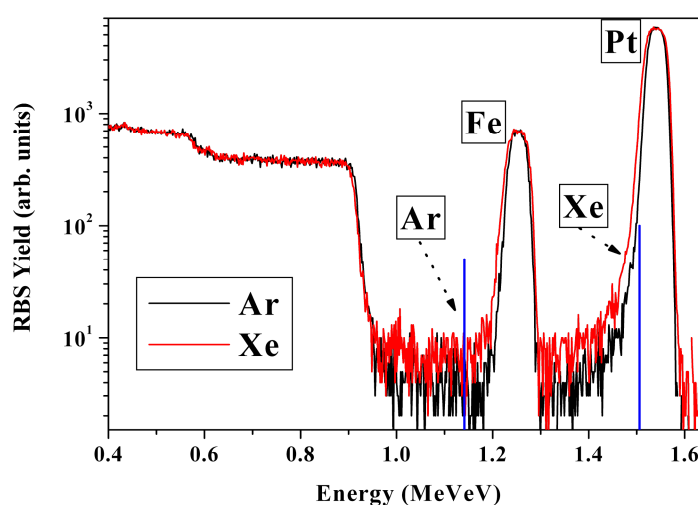


Figure 7.1: Comparison between RBS data obtained from as-deposited films grown by the layers – by – layer mode at 3 Pa in Ar or Xe discharge.

Despite the high deposition pressure, the slopes of the Fe and Pt peaks indicate a quite smooth interface on the contrary of the 125 nm layer described in chapter 6. From the RBS

data analysis there is no indication of Xe or Ar trapped into the layer. As-deposited sample RBS results are compared with the XRR ones (Table 7- 1 last column; Figure 7.2-a, b). All layers are characterized by a density reduction in comparison with the bulk crystalline one, evaluated by a comparison between the RBS layer thickness Δ_{RBS} and Δ_{XRR} . Samples deposited in Ar have densities at 60-65 % of bulk density and in Xe case densities are between 48-55 %, because of a different surface coverage as visible in the SEM plain views (insets Figure 7.2). In the case of Xe (Figure 7.2-b inset), grains agglomerate in clusters of about 50 nm in lateral size. *Yoneda wings* angular positions [125] in the diffuse scattering (Figure 7.2-a, b) confirm film density reduction, by a shift of the critical angle for total external reflection to lower incident angles with respect to the theoretical ones.

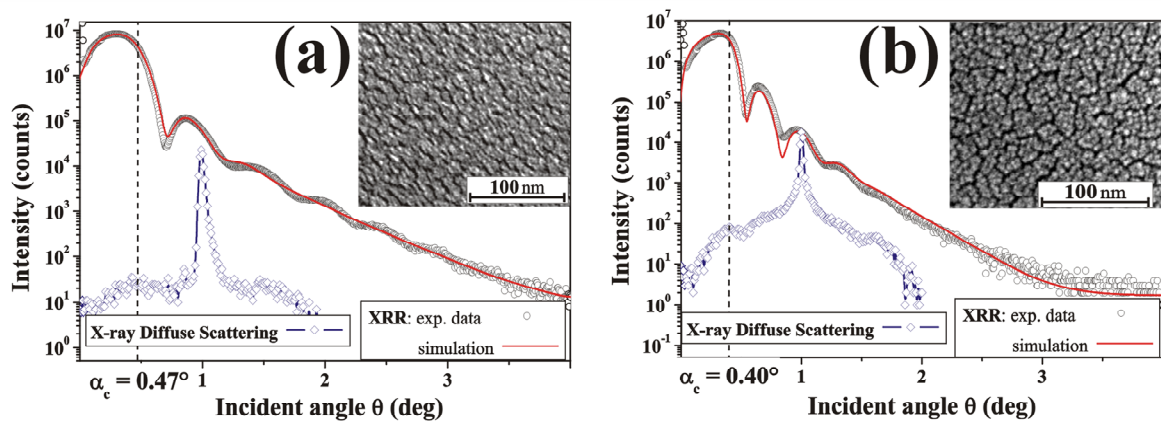


Figure 7.2: Comparison between XRR patterns obtained from as-deposited films grown by the layer – by – layer mode at 3 Pa in a) Ar (A2) or b) Xe (X2) discharge. The bar indicates the critical angle α_c angular position. Insets: SEM plain views of the corresponding films.

From XRR curves damping, the layer roughness results of about 1.0 nm for all as-deposited films. From the shape of the DS (see paragraph 4.2.1, figure 4.11) it is possible qualitatively conclude that the in-plane surface roughness of the layers deposited in Ar is completely uncorrelated. On the contrary, the surface roughness of the films grown in Xe is characterized by a higher correlation length.

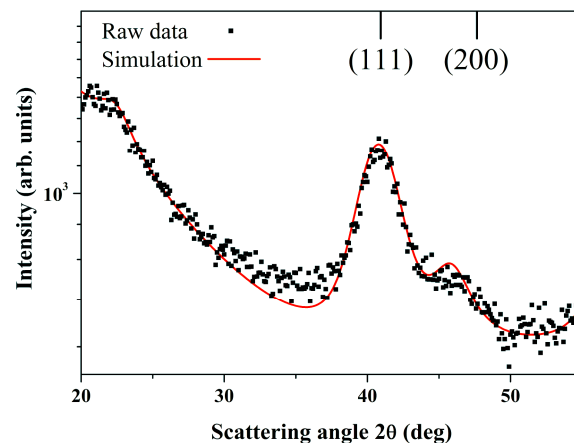


Figure 7.3: GIXRD at ($\alpha_i = 0.6^\circ$) of Al as-deposited film: angular positions of Al phase are marked

The GIXRD investigations showed the same profile for all as-deposited films in all deposition conditions. In Figure 7.3, a typical example from the layer grown in the condition A1 is reported, that indicates as a main phase the *fcc* chemically disordered one having an average crystallite size, calculated by Debye-Scherrer formula (paragraph 4.2.2), of 2.5 nm.

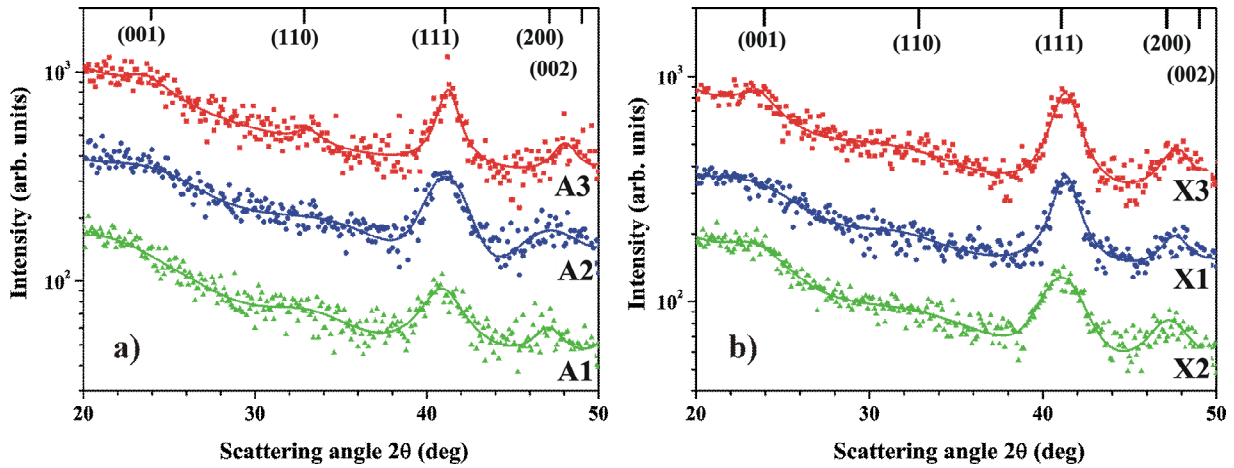


Figure 7.4: GIXRD analysis ($\alpha_i = 0.6^\circ$) of the annealed layers: a) deposited with Ar, b) with Xe. On top, Ll_0 phase reflections are reported.

In Figure 7.4 the GIXRD measurements after RTA are reported. The Ll_0 phase fraction reaches the detectable limit only when the film is grown in the sequential deposition method. Analyzing the (111) peak shape and area, the degree of crystallinity was calculated: FePt layers of the same thickness co-deposited in Ar (Figure 7.4-a: A1, A2) have lower degree of crystallinity than those in Xe (Figure 7.4-b: X1, X2). But, there is no difference between the deposition methods in Xe discharge (layers X2 and X3 in Figure 7.4-b), while the sequential layer deposition increases the degree of crystallinity in the A3 film in comparison with A2 one (Figure 7.4-a). This points out a stronger Fe and Pt intermixing during Xe assisted depositions. The crystallite sizes increases to a maximum value of 5 nm in the films A3 and X3, and remains approximately unchanged for A1 and X1 to 2.5 nm.

In Figure 7.5, the comparison between the XRR and DS patterns measured on layers grown in Ar and Xe after RTA. The annealing causes a reduction of film thickness computed from XRR measurements, therefore, an increase of layer density, confirmed by a shift of the critical angle α_c in X-ray surface scattering (Figure 7.5-a, b). In Ar discharges, after annealing, the layer A1 exhibits a density at 73% and A2 and A3 reach 85% of the bulk crystalline one; in Xe, films densities increase to an average value of 65% for X2 and X3 and remain constant to 56% for X1.

The RTA caused grain coalescence for all layers (Figure 7.5-insets). For the films grown in Xe discharges the clusters can reach larger in-plane dimensions (up to ~ 100 nm) than in the case of Ar assisted depositions. In all deposition conditions, the clusters are not isolated but joint together by FePt bridges.

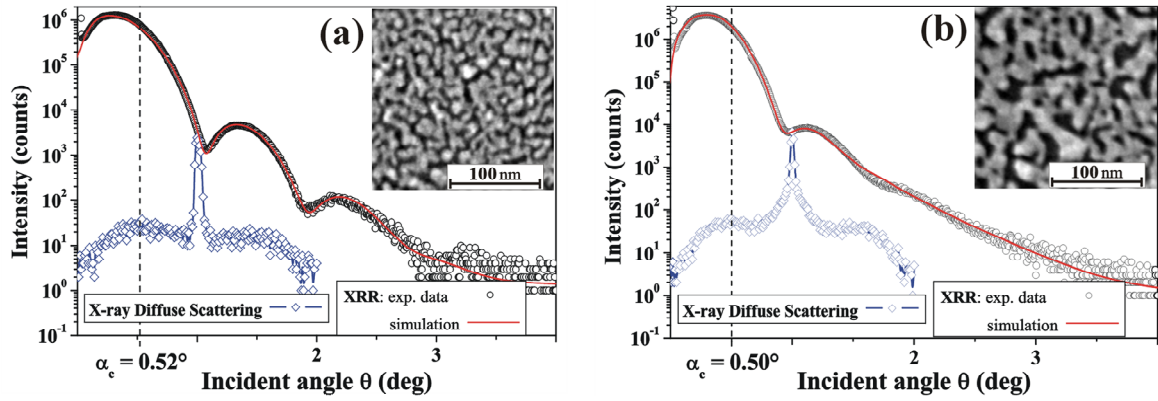


Figure 7.5: Comparison between XRR and surface DS at $2\theta = 2^\circ$ for the annealed layers: a) A1 b) X1: the bar indicates the critical angle α_c angular position. SEM plain views of the corresponding films.

SQUID measurements, collected at 300K (Figure 7.6), show the effect of using Xe as sputtering gas.

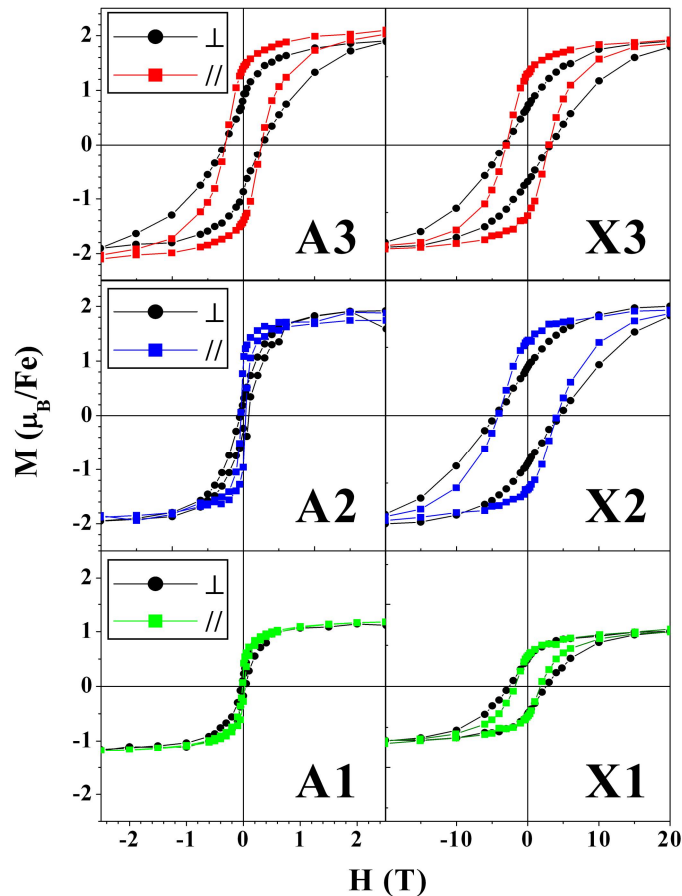


Figure 7.6: SQUID hysteresis loops at 300K of the annealed layers: A1; X1; A2; X2; A3; X3.

The coercive field increases from 0.3 kOe of A1 sample (Figure 7.6.A1), to 2.4 kOe of X1 (Figure 7.6.X1). For layers deposited with Ar, a thickness rise (samples A2 in Figure

7.6.A2) does not give a higher $L1_0$ fraction: for A2 the coercive field remained unchanged to 0.3 kOe.

The layer-by-layer growth slightly decreased the coercivity of layers deposited in Xe: comparing the coercive field of X2 at 4.2 kOe with the one of X3 at 3.0 kOe. On the other side, the sequential layer deposition strongly increased the $L1_0$ fraction in A3 sample (Figure 7.6.A3), with $H_C = 2.5$ kOe, in comparison to A2 (Figure 7.6.A2, $H_C = 0.3$ kOe).

7.1.3. Discussion

The main effect of the high deposition gas pressure is to provide a plasma completely thermalized where the contribution to the deposition rates is only driven by diffusion. As already pointed out in the previous chapters (chapters 5.3 and 6.2.3) the atom mean free path is strongly reduced at these working conditions ($\lambda_{Fe} = 1.3$ cm, $\lambda_{Pt} = 0.4$ cm in Ar and $\lambda_{Fe} = 1.1$ cm, $\lambda_{Pt} = 0.2$ cm in Xe discharge – Figure 5.9 and Figure 6.22), as a consequence a creation of a many collisions regime occurred in which all the atoms (sputtered and reflected gas neutrals) will lose their kinetic energies before impacting the substrate ($\langle E \rangle_{Ar} = 3.5$ eV, $\langle E \rangle_{Xe, Fe, Pt} < 1$ eV). The calculations reported in paragraphs 5.3 and 6.2.3 are still valid under the assumption of a collisionless sheath at the target, according to Keller *et al.* [83]. Moreover the particle stream from the target to the substrate will be completely isotropic. According to the SZM (figure 2.7 paragraph 2.5) the layers belongs to the Zone 1. The growth at strongly reduced surface adatom mobility will produce films characterised by tapered crystallites forming columns shape grains separated by voids. This indication is confirmed by the SEM investigation shown in (Figure 7.2-a, b insets).

The stronger FePt conglomeration, in the case of Xe assisted depositions, is unexpected considering that a lower deposition rate (like in Xe discharges) should support the realization of a smooth and compact layer [108], but it can be explained considering a longer diffusion length for the Fe and Pt atoms during depositions in Xe. The extracted Xe ions are accelerated by the plasma potential (~ 1 V) and the floating potential (~ -6.4 V for Ar and ~ -5.0 V in Xe, see appendix D) towards the substrate acquiring a higher momentum in comparison to the Ar ones; therefore, they will transfer a higher driving force to the already deposited atoms. In disagreement with *Thornton et al.* [108], who attributes a reduction of the surface adatom mobility, in high working pressure depositions, to trapped gas at the substrate surface, we had no indication of adsorbed inert Ar or Xe in the layer. The observed density reduction is therefore caused by an incomplete substrate coverage, which resulted more pronounced in the films deposited in Xe discharges.

The amount of the $L1_0$ phase, after annealing, is mainly ruled by two factors: the gas discharge and the deposition technique. By analyzing the SQUID measurements, it comes clear that in the case of Xe assisted deposition the energy budget required for the disorder – order transformation is reduced. According to the TTT diagrams and to the model proposed in Ref. 16, a reduction in layer thickness will significantly increase the annealing

time. Therefore, we argue that the creation of agglomerates enhances the probability to achieve a higher density of LI_0 nuclei that can then grow and transform the whole cluster during annealing. A more disperse structure, like those produced in Ar discharges, is not favorable to achieve a considerable LI_0 fraction and it is characterized by a low degree of crystallinity after annealing. This hypothesis is confirmed also by the results obtained investigating the layers grown in Ar discharges. In this case, the ordered phase fraction reaches the detectable limit (in GIXRD, too) only when the film is grown in the sequential deposition method. At 3 Pa the energetic component from the reflected Ar neutrals is vanished, not causing anymore atom intermixing during deposition and increasing the importance of a deposition in the layer – by – layer mode. The creation, already during growth, of a structure that emulates the LI_0 one decreases the ordering transformation energetic budget. The layer – by – layer deposition didn't further increase the LI_0 fraction in layers deposited in Xe. This effect can be justified considering the higher momentum transfer from Xe to the Fe / Pt atoms in comparison to Ar: the same force that is provoking agglomeration is responsible of a local atoms intermixing during layer growth.

In conclusion, Xe assisted deposition enhances layer coarsening in the as deposited state. Small 2.5 nm crystallites agglomerate in clusters having a lateral size of about 50 nm. In Ar discharges, layers show an almost closed morphology with high a degree of uncorrelated roughness.

Using Ar as sputtering gas, disorder-order transformation occurs only for a layer – by - layer deposition. In Xe, the minimum amount of FePt, to obtain the LI_0 phase at 550°C, is decreased to 3 nm bulk equivalent thickness.

Cluster shape anisotropy forces a weak preferential orientation of the layer easy axis in the in-plane direction.

7.2. FePt/Ag nanocomposite layers

Ag is widely studied for FePt particulate layer formation, [11, 12, 70 - 73] being a suitable matrix with a lower surface energy ($\sim 7.11 \times 10^{14}$ eV / cm² [74]) than FePt ($\sim 1.31 \times 10^{15}$ eV / cm² [75]) and therefore, cannot be easily segregate into the FePt particles.

In this study, the effect of Ag is investigated to enhance FePt cluster formation. The methodology applied is a sequential deposition of FePt and Ag at 400°C. The evolution of the nanostructures during deposition, as function of the amount of Ag, is observed, *in-situ*, by GISAXS (paragraph 4.2.3). GISAXS is a powerful tool to investigate *in-situ* the morphology and distribution of nanostructures on a substrate surface or buried in a matrix. The use of a synchrotron source is fundamental to have a reliable GISAXS signal to control the clusters morphology even during growth. In the end, we will discuss about their magnetic properties by SQUID hysteresis loops measured at 300 K. This study was published in *Advanced Engineering Materials* 11-6, 478 (2009).

7.2.1. Experimental parameters

The *in-situ* studies of the FePt/Ag nanoparticles growth was performed by using the set-up described in paragraph 3.2 at the ROBL beamline (paragraph 4.2.4). Figure 7.7 shows a schematic sketch of the experiment.

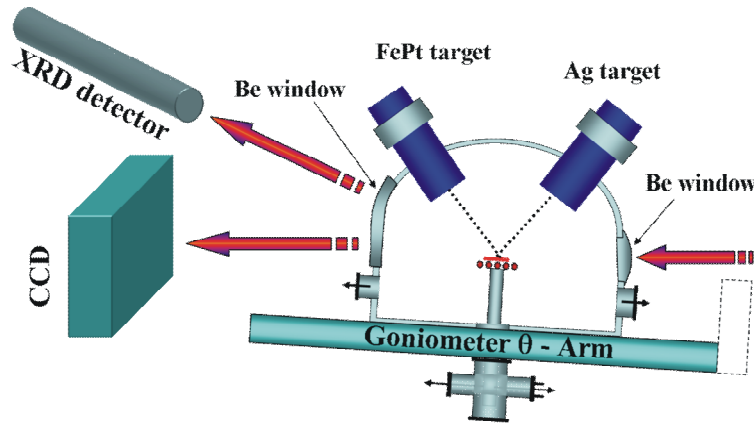


Figure 7.7: schematic drawing of the setup using two detectors (point detector for diffraction and CCD for GISAXS) and two magnetrons for deposition.

The layer deposition was carried out using a base pressure of 5×10^{-5} Pa and applying Ar as sputtering gas at a working pressure of 0.3 Pa. The FePt and Ag layers were deposited on $15 \times 15 \text{ mm}^2$ Si(100) substrates with 500 nm amorphous SiO_2 layer on top. The deposition temperature was 400°C at the substrate surface. From 1 inch targets of FePt (50 at% Fe – 50 at% Pt) alloy and pure (4N) Ag, two layers were prepared both consisting of two Ag-FePt double layers finishing with a FePt layer. For sample A the deposition sequence starts with FePt and a low Ag amount (~ 0.3 nm) that should separate the FePt islands [73]. Sample B starts with a larger Ag amount corresponding to a layer thickness of about 5 nm that forms directly small Ag islands on the SiO_2 -surface [151].

The *in-situ* X-ray investigations were carried out at an energy of $E = 10$ keV ($\lambda \sim 1.24$ Å) to decrease the air scattering for GISAXS measurements. A two-dimensional position sensitive CCD detector, at 174.3 cm from the goniometer rotation centre, was used for GISAXS studies. To obtain a reasonable signal to noise ratio and resolution the incident beam size was chosen to be $0.2 \times 0.22 \text{ mm}^2$ (H×V). The CCD data have been corrected for the dark signal and the flat field. A sequence of patterns was collected during deposition when particles formation starts and evolves. To detect the formation of the $L1_0$ FePt phase, a scintillation detector was positioned to analyse the (110) FePt superstructure peak at $2\theta = 26^\circ$. The experimental setup and the chosen X-ray energy were optimised to suppress the Fe fluorescence resulting in an almost homogenous background.

To study the degree of the $L1_0$ phase after deposition, X-ray diffraction experiments (in grazing incidence and in ω - 2θ geometry) were performed, by the D5005 Bruker/AXS diffractometer with Cu- K_α radiation (paragraph 4.2.4). Plan view micrographs, realized by SEM, were used to investigate the layer surface morphology and finally SQUID hysteresis loops were collected at 300 K to analyse the nanostructures magnetic properties.

7.2.2. Results and discussion

After the *in-situ* scattering experiments the layers were characterised by RBS that had revealed the following compositions, assuming bulk densities and closed films: for sample A: 7.3 nm thick Fe₅₄Pt₄₆ layer separated by 0.2 nm Ag and for sample B: 7.5 nm thick Fe₅₇Pt₄₃ layer separated by 6.0 nm Ag. The following deposition rates could be calculated: 0.4 Å/s for FePt, and for Ag, 0.05 Å/s for sample A and 0.5 Å/s for sample B. The difference in Ag deposition rates is explained considering that, at 400°C, Ag is highly mobile on surfaces especially when the total amount of deposited material is not enough to form a continuous layer. The Ag binding surface energy is 3 eV therefore it can be sputtered away by Ar atoms impacting the substrate with energies of about 89 eV, as shown from the calculations in paragraph 5.3.

Figure 7.8 shows the GISAXS patterns recorded during deposition at $\alpha_i = 0.35^\circ$, slightly below the FePt and Ag critical angles for total external reflection.

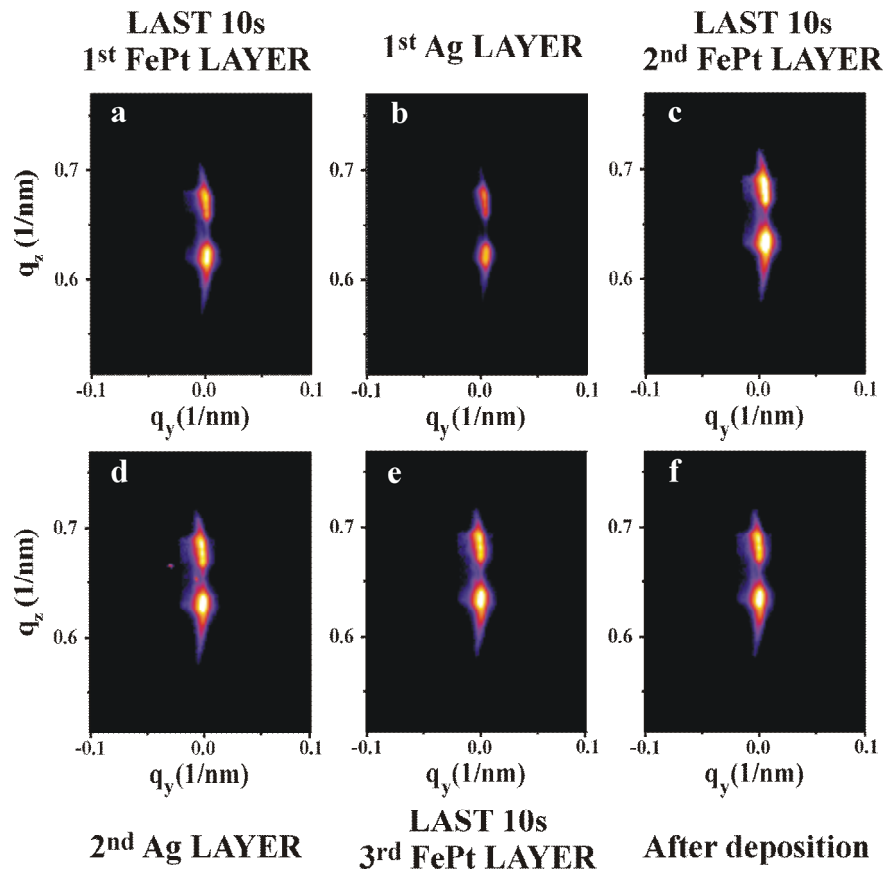


Figure 7.8: GISAXS evolution patterns collected for 10s during deposition at an incident angle $\alpha_i = 0.35^\circ$ for sample A (intensity in logarithmic scale): (a) is the profile at the end of the first FePt layer deposition, (b) is the beginning of the first Ag deposition (c) is the last 10s of the second FePt film, (d) is collected during the last Ag layer, (e) the last 10s of the fourth FePt layer; figure (f) is collected just after deposition at 400°C.

There is no significant change during growth. The broadening of the specular and transmitted signals points out a film structure with increasing roughness during growth.

The FePt phase evolution is reported in Figure 7.9, by the data collected from the point detector around the (110) reflection (counting time 48 s for each scan).

The Ll_0 phase formation started at 300 s after the start of deposition corresponding to a FePt thickness of about 12 nm. A homogeneous increase of the background, ascribable to Fe fluorescence into the detector window, was detected during the whole experiment. Therefore, peak integral area has been calculated by subtracting to every peak its own background signal. We observed a constant increase of the peak integral intensity, having a Boltzmann like behaviour, but, it didn't reach a constant value during deposition time indicating a not completed phase transformation; but a further annealing would induce undesired islands coalescence. During deposition, crystallite size is increasing from 6 to 11 nm. The FWHM of the (110) peak after 372 s of deposition is about 1.0° and shrinks to 0.6° in the final state, indicating that the amount of Ag is too low to separate the FePt islands that is confirmed by missed GISAXS signal at the corresponding Q values.

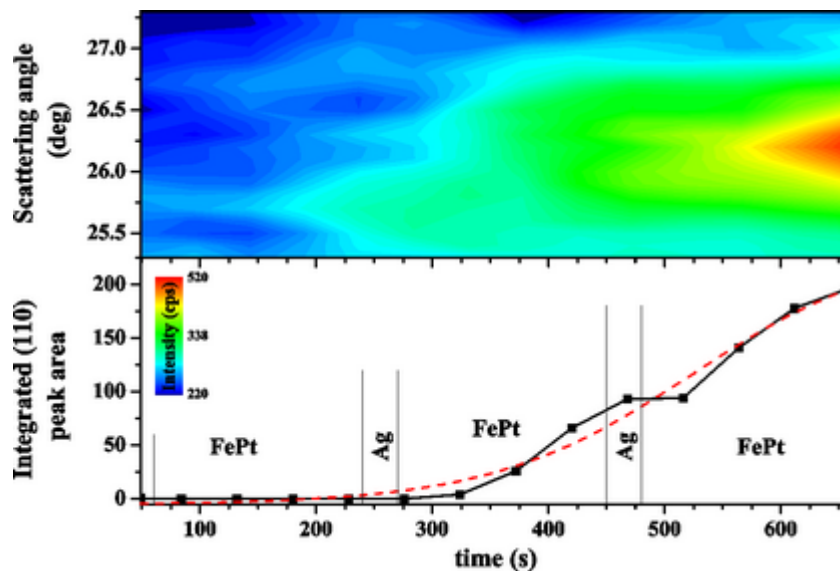


Figure 7.9: GIXRD ($\alpha_i = 0.5^\circ$) results on the (110) FePt reflection during deposition of sample A. Lower graph: peak integrated area vs. deposition time, experimental points (black line with dots) corresponding to the middle of each scan; simulation with Boltzmann function: red dashed line. Upper graph: (110) reflection peak evolution.

The second investigated sample is characterised by a deposition of 6 nm of Ag directly on the a -SiO₂ at 400°C that should lead to Ag islands formation [151]. In Figure 7.10, the GISAXS evolution is shown: during growth Figure 7.10-a to Figure 7.10-e and after cooling down at RT, Figure 7.10-f. From other experiments, using an identical sputtering chamber [151], it is known that Ag, deposited on SiO₂ forms nanoclusters according to the Volmer-Weber mechanism [150], characterised by an initial nucleation followed by the nucleus growth. The subsequent FePt layer is, therefore, replicating the low frequency roughness created by Ag enhancing the GISAXS signal (Figure 7.10-c). The next Ag layer is, again, forming islands that will further divide the FePt. The use of Ag is forcing the agglomeration of FePt into clusters, having side facets tilted by almost 25° from the sample surface normal that can be clearly distinguished from the GISAX pattern collected at the end of the last FePt layer deposition (Figure 7.10-f).

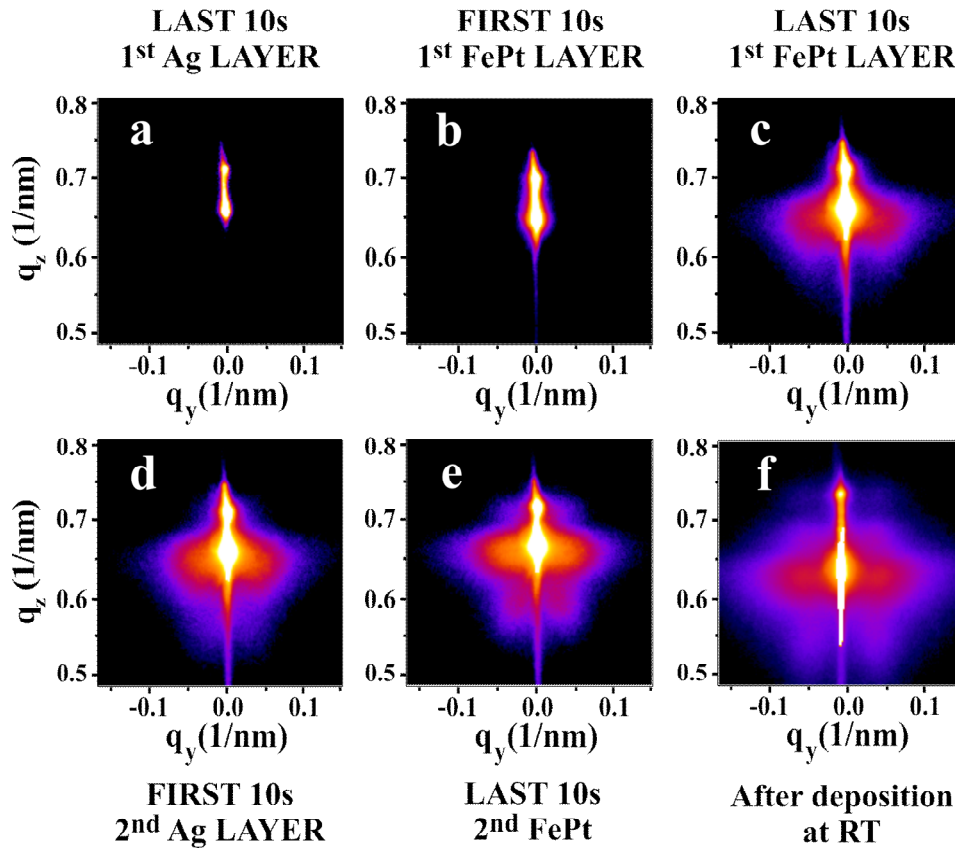


Figure 7.10: GISAXS evolution patterns collected for 10s during deposition at an incident angle $\alpha_i = 0.35^\circ$ for sample B (intensity in logarithmic scale): (a) is the profile at the end of the first Ag layer deposition, (b) is the beginning of the FePt deposition concluded in (c), (d) is the last Ag deposition and (e) the last FePt layer at 400°C ; (f) is taken at RT directly after deposition.

Figure 7.11 shows line scans parallel to Q_y during and after the deposition. From Figure 7.11-a a characteristic length size was calculated, that shrinks at RT (Figure 7.10-f) to 150 nm from 180 nm at the end of the first FePt deposition (Figure 7.10-c). The facets are getting stronger during the growth as it can be seen in Figure 7.11-b.

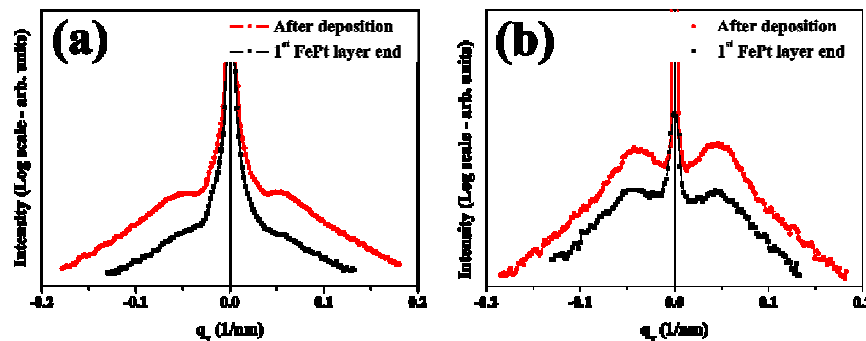


Figure 7.11: Line scans along q_y , of the GISAXS patterns of fig. 4 at (a) $Q_z = 0.97 \text{ nm}^{-1}$ ($\sim \alpha_c$) and (b) showing the facet peaks slightly below α_c at $Q_z = 0.95 \text{ nm}^{-1}$ of sample B taken at the end of the first FePt layer deposition and directly after growth at RT.

The samples were additionally characterized by *ex-situ* diffraction experiments; X-ray measurements at fixed grazing incidence angle (GIXRD $\alpha_i = 0.6^\circ$) and $\omega/2\theta$ -scans, the results are reported in Figure 7.12. Sample A shows almost no difference for both scans

indicating a polycrystalline behaviour. In the $\omega - 2\theta$ symmetric scan of Sample B, which is characterised by a much higher amount of Ag, the $L1_0$ phase is hardly observed, while a clear (001) superstructure peak appears in the GIXRD pattern. Therefore, the $L1_0$ phase has a weak in-plane preferential orientation. On the other side, decreasing the amount of Ag gives potentially a larger amount of the ferromagnetic $L1_0$ phase, but completely random oriented. The crystal grain size for both samples is in the order of 10 nm, i.e. one cluster itself consists of more than one grain.

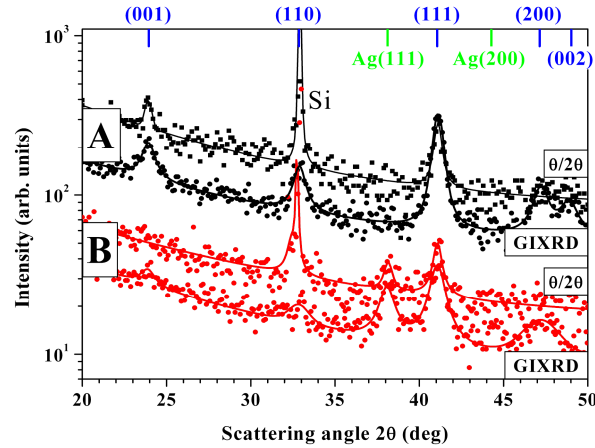


Figure 7.12: $\omega - 2\theta$ and GIXRD ($\alpha_i = 0.6^\circ$) patterns of sample A (black line) and the sample B (red line).

The GISAXS investigations were *ex-situ* confirmed by SEM plan views shown in Figure 7.13. The granular morphology of the two layers is strongly different: Sample A is characterised by a grain size distribution of around 50 nm. Already a low amount of Ag (2 layers of 0.2 nm) causes the formation of FePt nanoparticles but without clear separation between the islands. The deposition of Ag directly on SiO_2 is forming clusters. The subsequent FePt deposition is, therefore, covering the Ag nanoislands surface. At the chosen deposition temperature of 400°C , Ag has a high surface mobility and tends to agglomerate; this leads to the formation of big nanoclusters up to a size of 500 nm. But, it is possible to distinguish smaller particles, within the big agglomerates, with an average size above 50 nm. The last ones are then detected by the GISAXS experiment.

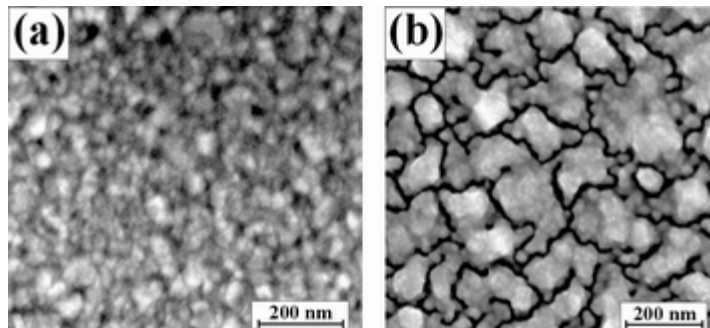


Figure 7.13: SEM micrograph of the sample A (a) and the sample B (b)

The position of the *Yoneda wings*, in the X-ray DS not shown here, indicates the critical angle α_c [125], which is connected with the average electron density and therefore with the material density. Sample A shows a value of the critical angle of $\alpha_c \approx 0.46^\circ$ close to the

bulk value of FePt (FePt: $\alpha_c = 0.49^\circ$, Ag: $\alpha_c = 0.44^\circ$), that supports SEM results that evidence no separation between the FePt islands. Sample *B* shows a smaller value $\alpha_c = 0.4^\circ$ corresponding to a reduction of the material density of more than 30% in comparison to a theoretically closed layer system, i.e. the grown islands are separated by each other by voids.

In Figure 7.14, the SQUID hysteresis loops are reported. Two geometries were used with the magnetisation vector in and out of the sample surface plane.

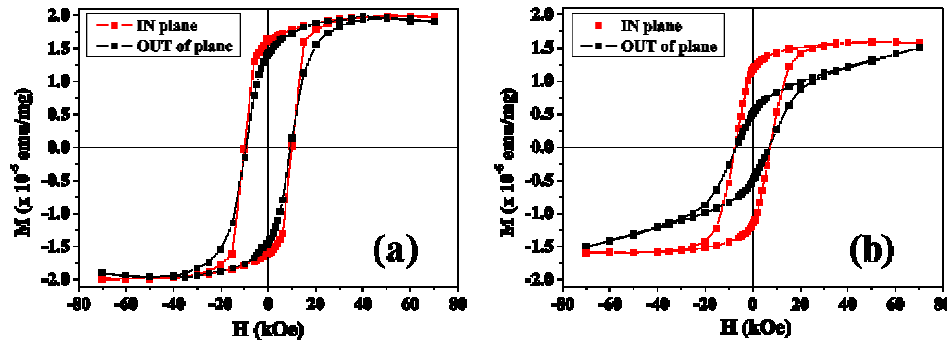


Figure 7.14: SQUID hysteresis loops of the sample A (a) and the sample B (b) at 300K.

Both samples have a similar coercive field: 9.5 kOe and 7.5 kOe for sample A and B, respectively. The *squareness* value is 0.7 for both in-plane measurements, while there is a strong difference between the two out-of-plane behaviours: the cluster structure of the sample *B* causes in-plane anisotropy. The increasing of the Ag amount is not decreasing the magnetic properties of the layer, as a proof that there is not an alloy creation during deposition.

7.2.3. Conclusion

The simultaneous detection of cluster growth and evolution by GISAXS and phase transition in XRD geometry was successfully applied to investigate, *in-situ*, the deposition of the FePt/Ag system on amorphous SiO_2 at a deposition temperature of 400°C . The strong ferromagnetic $L1_0$ phase was obtained already during growth. The possibility to tune beam energy, to reduce air scattering and absorption, together with the high brilliance of the synchrotron source had made possible to obtain a reliable GISAXS signal to control the clusters morphology even during formation and evolution. We have shown that the use of Ag is not decreasing the FePt magnetic properties. Using a certain amount Ag it is possible to trigger islands growth of the hard ferromagnetic $L1_0$ -FePt phase. Small isolated FePt cluster can be created that give a preferential in-plane magnetisation (sample *B*). However, with increasing Ag amount we observed the formation of large clusters (> 500 nm) composed by the agglomeration of smaller grains. A further optimisation of the process parameters is necessary to reduce the tendency to large clusters formation by finding out the right Ag content and an appropriate process temperature that allows the transition to the oriented $L1_0$ -FePt phase and prevents clusters agglomeration, to achieve the ideal state in which one cluster is one magnetic domain.

8. Conclusions

This study was focused in three main subjects:

1. *to achieve low Al to Ll_0 phase transition temperature,*
2. *to control FePt (001) preferential orientation independently from the substrate nature,*
3. *to realize Ll_0 -FePt nanoclusters.*

The aim was to correlate film structural characteristics, investigated by X-ray scattering methods, with the magnetic properties. Especially, *in-situ* X-ray analyses performed by synchrotron radiation (ROBL beamline at the ESRF) prove to be a very powerful method to study and understand the effect of the layer growth conditions on phase transformation and preferred orientation. Theoretical calculations about the particle energy distribution during layer deposition justified the film physical properties evidenced by X-ray scattering results.

The phase transition was investigated for thick (~ 70 nm) equiatomic FePt layers on *a*-SiO₂ deposited by dc magnetron co-sputtering of Fe and Pt in Ar discharge at 0.3 Pa. This study was mainly conducted at the synchrotron (ROBL beamline) to exploit the possibility of *in-situ* X-ray scattering measurements during vacuum annealing. The disorder-order transformation occurred at $(320 \pm 20)^\circ\text{C}$, achieving an high degree of order $S > 0.94$, and was confirmed by SQUID magnetic measurements ($H_C = 0.5$ T). On the contrary, the film grown at 3 Pa, showed a higher transition temperature (400°C) and a lower magnetic hardness ($H_C = 0.2$ T). TRIDYN simulations together with considerations about particle transport inside the plasma reveal that the sputtered atoms arrive at the substrate with energies of only few eV, whereas a significant amount of reflected Ar neutrals, from the Pt target, carries energies well above the displacement threshold (~ 25 eV in metals). Therefore, it was supposed that vacancies are created in the layer grown at 0.3 Pa decreasing the thermal budget required for the disorder-order transformation. In this way, the Fe diffusion length is enhanced with respect to the values calculated by Rennhofer *et al.* [29]. The hypothesis of point defect formation during film growth can also explain the discrepancy between our results and the JMAK model as adapted to FePt by Berry *et al.* [16]. After calorimetric studies, they indicated $\sim 10^5$ s as the required time to achieve 95% of Ll_0 phase in 10 nm thick films at 350°C . Results comparable to those described in our work can be found only when the FePt layers are grown by the multilayer sequence deposition method, preferably by MBE [40, 41] and with post He⁺ irradiation [35, 37-39].

By means of a sequential monolayer-like deposition the (001) preferential orientation can be forced by growing a structure that emulates the final (001) Ll_0 phase. The creation of directional short range order (DSRO) areas, during deposition, will strongly support the (001) orientation. For this purpose, the analysis of the deposition process results to be

fundamental. In fact, the energetic Ar impacts during layer growth were extremely counterproductive to control the (001) preferential orientation in thin (~ 14 nm) FePt films. Comparing layers deposited by co-sputtering and multilayer sequence methodology, in Ar discharge at 0.3 Pa, it was not found any significant improvement of the film (001) orientation using the sequential layer growth, even after vacuum annealing at 700°C. This result was justified considering that the energetic Ar atoms impacting the substrate cause atom intermixing that suppresses the DSRO of the as deposited film. Layers grown at the same pressure in Xe discharge showed, after annealing at 700°C, a strong (001) preferential orientation when the growth is performed by the multilayer sequence deposition. The energy contribution of reflected Xe neutrals during growth is reduced to 13 eV, supporting adatom mobility to provide films with a compact structure and a smooth surface. This energy is also low enough to maintain the DSRO created by layer –by – layer depositions. The importance of the discharge characteristics on layer properties is absolutely underestimated in the FePt literature. The effect of the sputtering gas on FePt ordering was briefly investigated by Liu *et al.* [152] but without any remark about the possibility to use Xe discharges. On the contrary, the evaluation of the particle energy impacting the substrate is widely applied to semiconductors processing that is the usual field of application of the theoretical studies used in this thesis (paragraphs 2.4 and 2.5) to develop the model of plasma particle transport in magnetron sputtering. The ordering transformation temperature and the film preferential orientation are usually correlated only to the multilayer structure (i. e. single layer thickness) [10, 35, 40-43] without any investigation of the growth technique, that, as demonstrated in this work, can have a high impact on the film (001) preferential orientation.

The acquired methodology to control FePt (001) preferential orientation can be applied to FePt deposition on whatever suitable buffer layer meeting the criteria of the recording magnetic media technology. Usually a buffer layer like CrRu [54] or MgO [40] is required to promote the film (001) preferential orientation, but how to integrate these buffer layers with the soft-magnetic underlayer (NiFe, CoNbB, FeAlSi, CoFeB, FeTaN, FeTaC and CoFe) is an up-to-date challenge [66]. Therefore, the possibility to exploit Xe discharges features together with *in situ* X-ray scattering studies, during layer deposition and annealing, allows a faster optimization of the process parameters in terms of growth conditions and thermal stability.

A high working pressure regime provides complete thermalized plasma, vanishing all energetic particle contributions, enhancing the particle stream oblique component and suppressing adatom mobility. Therefore, clustering is supported. FePt nanoisland formation, in Ar or Xe discharges at 3 Pa, was studied. Ultra thin (< 10 nm) layers were grown on *a*-SiO₂ at RT and subsequently annealed by RTA at 550°C for 600 s. The use of Xe as sputtering gas is increasing the FePt conglomeration because of a higher momentum transfer from the impacting Xe ions to the deposited atoms in comparison with Ar ions. Nanoislands formation, already in the as deposited layers, provide the *LI*₀ phase after annealing also in the case of a total FePt amount below 5 nm. In Ar discharges it is necessary to use the multilayer sequence deposition to obtain a comparable fraction of *LI*₀

phase for a comparable thickness. To explain the higher LI_0 fraction obtained in nanoclusters grown in Xe discharges it was suggested that the creation of compact agglomerates during deposition enhances the probability to form LI_0 nuclei, reducing the phase transition to a grain growth process. These results are in good agreement with the research conducted by Itoh *et al.* [76, 77] in Ar discharges at 1.2 Pa. But, with the introduction of Xe as sputtering gas, it is possible to further decrease the total amount of deposited FePt, to enhance cluster formation and separation obtaining a high LI_0 fraction in the isolated nanoislands after annealing.

At the end, it was described a preliminary study to realize nanocomposite layers of FePt and Ag. FePt nanoisland formation and growth, at 400°C, was monitored *in-situ* by GISAXS at the ROBL beamline. Simultaneously the LI_0 phase formation was detected giving an indication of the critical thickness (~ 12 nm) for the disorder-order transformation at 400°C. Ag has a lower surface energy therefore is supporting FePt clustering by diffusing interstitial. For a total amount of Ag of ~ 0.4 nm, it was observed the formation of a granular film without any clear indication of spread FePt nanoisland in a Ag matrix. If Ag is directly deposited onto α -SiO₂ and its total amount is increased to ~ 6 nm, the formation of large clusters was detected. These preliminary results confirm the investigations of Zhao *et al.* [73] on similar FePt/Ag systems but deposited on MgO, that is well known for supporting FePt Volmer-Weber growth. The simultaneous detection of the AI to LI_0 phase transformation (by GIXRD) and the nanoislands formation and evolution (by GISAXS) is an absolute unique technique and allows to put in direct relation the minimum FePt amount for the formation of the hard magnetic phase with the minimum FePt amount necessary for isolated nanoclusters creation. This approach could be also applied to completely clarify the role of Xe in the AI to LI_0 phase transformation in ultrathin layers grown at 3 Pa.

Towards an increase of the signal-to-noise-ratio, well isolated nanoclusters are preferred. The study of the addition of insoluble materials is the nowadays research. Very good results were obtained by layer – by – layer depositions of FePt and SiO₂ [10, 66-68]. Alternatively, the combination of a pre-patterned substrate (ripples, dots) and the deposition at 3 Pa seems a more flexible way to obtain separated aligned FePt nanoislands.

Appendix A:

The nuclear stopping cross section

The nuclear stopping cross section $S_n(E_0)$ of the incoming ion in the target can be calculated in terms of the reduced energy $\varepsilon(E_0)$ [153]:

$$\varepsilon(E_0) = \frac{0.8853 \cdot a_0}{Z_i Z_T \cdot e^2 \cdot (Z_i^{1/2} + Z_T^{1/2})^{2\beta}} \cdot \frac{m_i}{m_i + m_T} \cdot E_0 \quad (\text{A.1})$$

by an analytical approximation to [154]:

$$S_n(E_0) = \frac{84.78 \cdot Z_i Z_T}{(Z_i^{2/3} + Z_T^{2/3})^{0.5}} \cdot \frac{m_i}{m_i + m_T} \cdot \frac{3.441 \cdot \varepsilon^{0.5} \cdot \ln(\varepsilon + 2.718)}{1 + 6.355 \cdot \varepsilon^{0.5} + \varepsilon(6.88 \cdot \varepsilon^{0.5} - 1.708)} \quad (\text{A.2})$$

where $S_n(E_0)$ is given in eV/A² and E_0 in eV. Equation (2.14) includes two correction factors $\alpha, \beta < 1$. The term $\alpha(m_T/m_i)$ considers the preferred collision cascade propagation in forward direction for $(m_T/m_i) < 1$ and $\beta(E_{th}/E_0)$ the significant reduction of the sputter yield for energies close to the threshold energy (E_{th} is equal to 22.6 eV and 32.2 eV for Fe; 23.4 eV and 34.1 eV for Pt impacted by Ar and Xe, respectively [90]).

The dependencies of $\alpha = f(m_T/m_i)$ and $\beta = f(E_{th}/E_0)$ are plotted in Figure A.1.

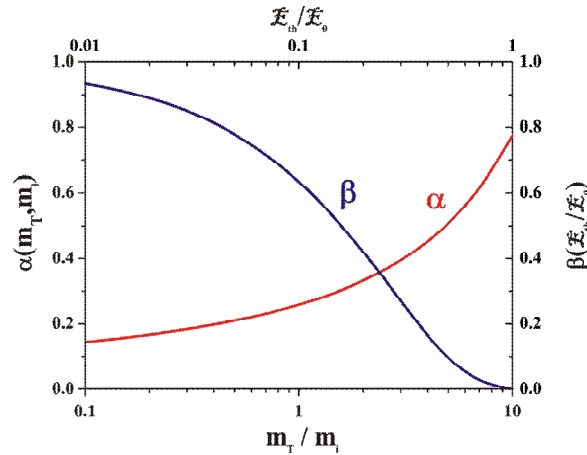


Figure A.1: Values of $\alpha = f(m_T/m_i)$ and $\beta = f(E_{th}/E_0)$ [89].

Appendix B:

X-ray scattering from a free electron

As already mentioned in Chapter 4, X-rays will interact only with the electrons, it is, therefore, fundamental to describe X-ray interactions with matter starting from the description of the Thompson scattering. Here it will not be taken into account any photon energy loss due to scattering (Compton scattering) but only the classical model will be described.

Considering an unpolarized X-ray beam incident on a free electron along the x direction (Figure B.1), we would like to evaluate the electric field intensity in the point P at a distance R from the scattering centre O .

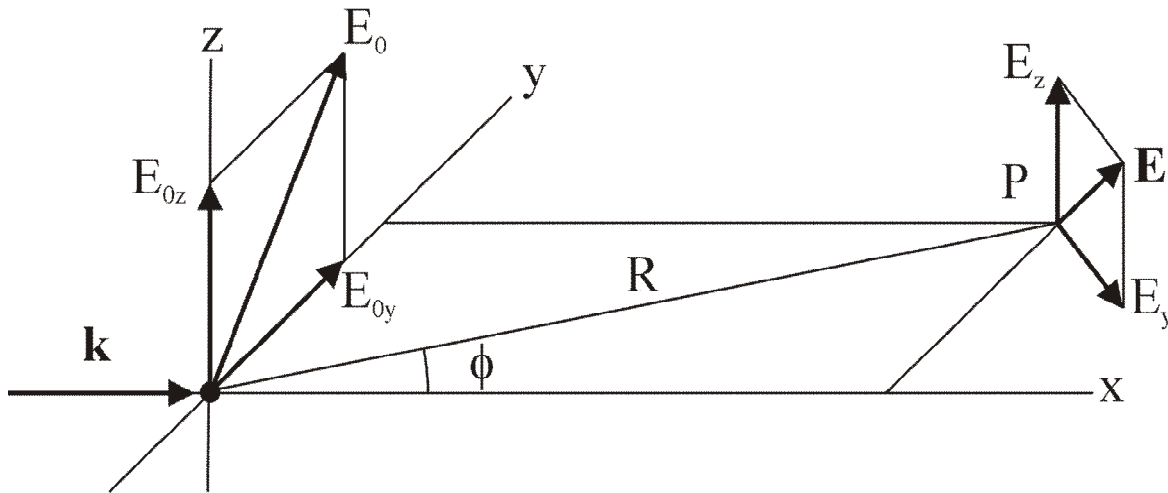


Figure B.1: X-rays scattering from a free electron: classical approximation [21].

Choosing an arbitrary direction of the electric field in the plane (y,z) (\mathbf{E}_0), the y component E_{0y} will make the electron oscillate with an acceleration $a_y = -(e/m) \cdot E_{0y} \cdot e^{i\omega(R/c)}$, along y . The electron will act as a dipole radiating a scattered wave which electric field will lie in the charge oscillation plane and R (x, y).

The amplitude [$\varepsilon_{y'} = E_{0y} \exp(i\omega t)$] of the electric field in P will be:

$$E_{y'} = - \left(\frac{e^2}{4\pi\epsilon_0 mc^2} \right) \cdot \frac{E_{0y}}{R} \cdot \cos \phi \quad (\text{B.1})$$

and along z :

$$E_z = - \left(\frac{e^2}{4\pi\epsilon_0 mc^2} \right) \cdot \frac{E_{0z}}{R} \quad (\text{B.2})$$

The electric field in P , perpendicular to the beam direction of incidence, can be expressed as:

$$E^2 = \left(\frac{e^2}{4\pi\epsilon_0 mc^2} \right)^2 \cdot \frac{1}{R^2} \cdot (E_{0y}^2 \cos^2 \phi + E_{0z}^2) \quad (\text{B.3})$$

But E_0 has equal probability to assume any orientation in the plane (y, z) , therefore it is necessary to consider the average value:

$$\langle E^2 \rangle = \left(\frac{e^2}{4\pi\epsilon_0 mc^2} \right)^2 \cdot \frac{\langle E_0^2 \rangle}{R^2} \cdot \left(\frac{\cos^2 \phi + 1}{2} \right). \quad (\text{B.4})$$

The observable quantity $I \sim \langle E^2 \rangle$ can be therefore easily calculated.

The factor $r_0 = \frac{e^2}{4\pi\epsilon_0 mc^2}$ is the *Thompson scattering length* equal to $2.82 \times 10^{-5} \text{ \AA}$, the scattering length of X-rays with a free electron in vacuum. The term $\left[(\cos^2 \phi + 1)/2 \right]$ is called polarization factor for an unpolarized primary beam.

Appendix C:

The equivalence between the Bragg law and the Laue condition

It can be demonstrated that the Bragg's law is exactly equivalent to the Laue's condition in the reciprocal space (Figure C.1).

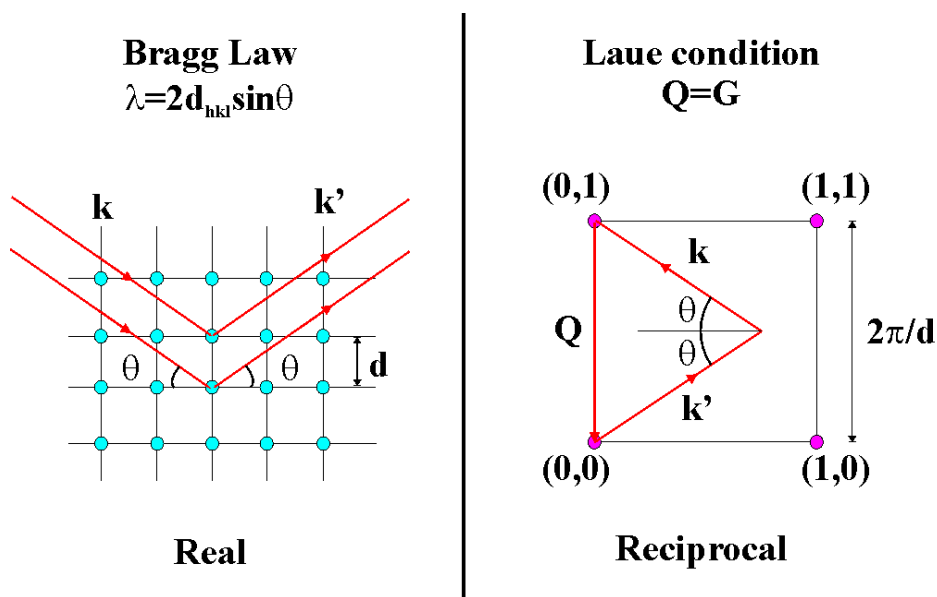


Figure C.1: the same scattering event described by the Bragg's law and by the Laue's condition in the 2D case [118].

In the real space the Bragg's law expresses:

$$\lambda = 2d_{hkl} \sin \theta \quad (C.1)$$

and in the reciprocal space it must be $\mathbf{Q} = \mathbf{G} = \mathbf{k}' - \mathbf{k}$. From geometrical point of view it is

$|\mathbf{Q}| = \frac{2\pi}{d}$. In the case of symmetrical reflections $|\mathbf{k}'| = |\mathbf{k}|$ and also, from Figure C.1,

$|\mathbf{Q}| = 2k \sin \theta$, thus $\frac{2\pi}{d} = 2k \sin \theta$, that is again equation (C.1).

Appendix D:

The order parameter S

As already mentioned in chapter 1, the FePt phase transition from the disordered *fcc* $A1$ to the ordered *fcc* $L1_0$ phase can be quantified by the introduction of the long range order parameter S .

It is possible to calculate the S parameter by computing the integral intensities of the (001) superstructure peak in comparison with the (002) fundamental one: those reflections independent from the degree of order are called fundamental, while reflections vanishing when the order vanishes are called superstructure. S is directly connected to the amount of atoms occupying the right sites: $S = 0$ for completely random arrangement, $S = 1$ for perfect ordered structures. It is therefore clear that the structure factor must be involved in the calculations because it is taking into account the position of all atomic positions in the unit cell. Considering the equation (1.1), where $r_{Fe, Pt}$ represents the fraction of sites occupied by the right atom and $w_{Fe, Pt}$ that fraction of sites occupied by the wrong atom, it can be written, in the case of the $L1_0$ structure:

$$F = (r_{Pt}f_{Pt} + w_{Pt}f_{Fe}) \cdot (e^{\pi i(h+l)} + e^{\pi i(k+l)}) + (r_{Fe}f_{Fe} + w_{Fe}f_{Pt}) \cdot (1 + e^{\pi i(k+h)}) \quad (D.1)$$

with $h+k = \text{even}$, $k+l = \text{odd}$

where $f_{Fe/Pt}$ are the Fe or Pt X-ray atomic scattering factor.

In this way the unit cell structure factor F can be evaluated: for the fundamental part

$$F = 4(x_{Fe}f_{Fe} + x_{Pt}f_{Pt}) \quad (D.2)$$

and for the superstructure part

$$F = 2 \cdot S \cdot (f_{Fe} - f_{Pt}) \quad (D.3)$$

that contains the S parameter.

Unfortunately this methodology is very sensitive to several effects that can produce appreciable errors. The two atoms are characterised by different Debye-Waller factors ($\propto \exp^{-M_{Pt/Fe}}$) and this difference become significant at high-order superstructure reflections, therefore it is important to choose low order superstructure peaks.

Moreover, in the real case, it must be introduced a correction that takes into account the angular dependency of the absorption, while, in this study, we neglected the surface roughness correction. Considering that the dispersion is contained in the imaginary part of the structure factor f , it is possible to write:

$$f_{Pt/Fe} = \text{Re}(f_{Pt/Fe}) + i \text{Im}(f_{Pt/Fe}) = f_{Pt/Fe} + i\Delta_{Fe/Pt} \quad (D.4)$$

The areas of the fundamental and superstructure peaks must be corrected according to the following relation:

$$A_{F/S} = K \cdot m \cdot (LP)_{F/S} \cdot (FF^*)_{F/S} \quad (D.5)$$

where K is a constant, m is the reflection multiplicity, LP represents the Lorentz-polarization factor and (FF^*) is:

$$(FF^*)_F = 16 \left[\left(x_{Pt} f_{Pt} \exp^{-M_{Pt}} + x_{Fe} f_{Fe} \exp^{-M_{Fe}} \right)^2 + \left(x_{Pt} \Delta_{Pt} \exp^{-M_{Pt}} + x_{Fe} \Delta_{Fe} \exp^{-M_{Fe}} \right)^2 \right] \quad (D.6)$$

and

$$(FF^*)_S = 4 \cdot S^2 \cdot \left[\left(f_{Fe} \exp^{-M_{Fe}} - f_{Pt} \exp^{-M_{Pt}} \right)^2 + \left(\Delta_{Fe} \exp^{-M_{Fe}} - \Delta_{Pt} \exp^{-M_{Pt}} \right)^2 \right]$$

where the term $\exp^{-M_{Fe/Pt}}$ takes into account the Debye-Waller correction that indicates a decrease of the scattered intensity due to temperature effects. The value of M can be calculated for temperatures $T > \Theta$, the Debye critical temperature [155]:

$$M = \frac{1.14 \cdot 10^4}{m_a \Theta} \frac{\sin^2 \theta}{\lambda^2} \left[\frac{1}{4} + \frac{T}{\Theta} \cdot \varphi \left(\frac{\Theta}{T} \right) \right] \quad (D.7)$$

where m_a is the atomic mass and λ is expressed in \AA . The value of the term $\left[(1/4) + (T/\Theta) \cdot \varphi(\Theta/T) \right]$ is tabulated as a function of Θ/T . The Debye temperature is 470 K and 240 K for Fe and Pt, respectively [155].

Therefore S can be calculated from the following expression:

$$\frac{A_S}{A_F} = \frac{(LP)_S \cdot (FF^*)_S}{(LP)_F \cdot (FF^*)_F} \quad (D.8)$$

At the beginning of the FePt study, the layers were deposited on 1.5 μm of $a\text{-SiO}_2$ on Si(001). The signal from the amorphous SiO_2 (figure D.1) was increasing the background underneath the FePt (001) reflection, altering the integrated intensity calculation. For this reason, thin FePt layers were grown on 500 nm $a\text{-SiO}_2$.

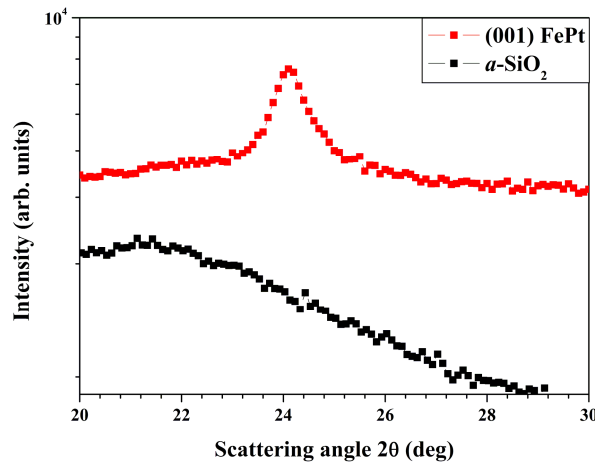


Figure D.1: Comparison between GIXRD patterns from (001) FePt and pure $a\text{-SiO}_2$ 1.5 μm , collected at ROBL.

Appendix E:

Langmuir probe measurements

In order to understand and control FePt growth process, the particle energy distributions have to be known. For this purpose ion, electron and plasma density, together with the electron temperature and the plasma potential were measured with a Langmuir probe at the substrate position.

One of the most popular devices to characterize plasma is the Langmuir probe [153, 157]. Langmuir probes are merely electrostatic probes consisting in a small metallic electrode inserted into the plasma. A power supply is biasing the probe to voltages of different polarity, the current collected at the electrode, the V - I curve, gives information about plasma conditions [78].

The Langmuir probe used in this study is the *SmartProbe*TM© provided by Scientific Systems [158]: a schematic drawing of the equipment is shown in Figure E.1.

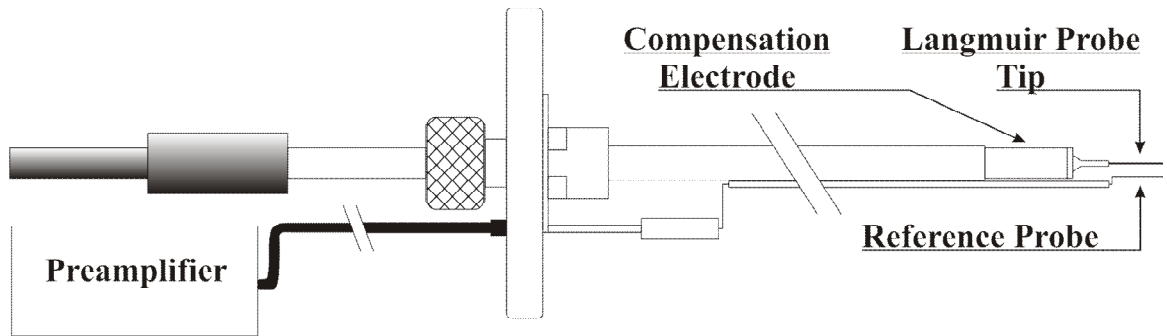


Figure E.1: Scheme of the Langmuir probe. The tungsten probe tip has a radius $r_p = 0.19$ mm and a length of 10 mm.

In absence of strong magnetic fields, when $r_{ce} \gg r_p$ ($r_{ce} = \frac{1}{H_0} \sqrt{\frac{2m_e V_{dc}}{e}} \approx 3.4$ mm is the electron Larmor radius, considering a $V_{dc} \approx 400$ V) [159], the plasma is supposed to be homogeneous in the probe surrounding and therefore local measurements of plasma parameters [78, 160].

The evaluation of the V - I characteristics requires the approximation of an isotropic Maxwellian electron velocity distribution function (2.4): the electron density n_e and the average electron energy can be determined according to equations (2.7).

In Table E-1 the deposition conditions, used during Langmuir probe measurements, are summarized.

Gas	P (Pa)	Target material	W_{dc} (W)	V_{dc} (V)	I_{dc} (mA)
Ar	0.3	Fe	16	368	43
		Pt	3	379	8
Ar	3	Fe	38	275	138
		Pt	4	271	14
Xe	0.3	Fe	25	414	61
		Pt	3	416	8
Xe	3	Fe	44	402	110
		Pt	5	385	13

Table E-1: Deposition parameters

In Figure E.2 are reported the V - I curves collected for Ar and Xe discharge, as function of the pressure.

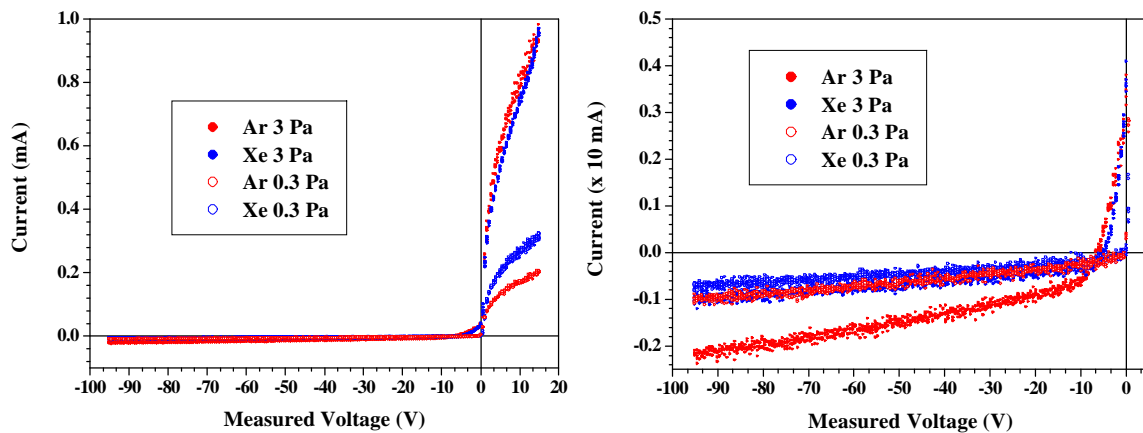


Figure E.2: V - I curves collected at the sample position as function of the sputtering gas and pressure. For $I \leq 0.05$ mA, current values are amplified of factor 10 (bottom graph).

Three different zones can be identified:

- $V_{probe} \ll 0$: ion saturation current region. Only ions are collected at the probe while the electrons are repelled. This causes the formation of a thin positively charged sheath between plasma and probe surface.
- Small V_{probe} values: transition region. The probe has a negative voltage with respect to the plasma and the collected current is mainly due to electrons energetic enough to overcome the barrier: the current has an exponential tendency and from its slope the electron mean energy can be derived
- $V_{probe} \gg 0$: electron current region. The tip current is due to accelerated electrons. In this region, the probe could be damaged because of excessive electron current collected; therefore the V_{probe} was limited to 15 V.

There is about two order of magnitude difference between the ion and the electron saturation current, because of different masses, temperatures and therefore different sheathes between probe and plasma, in the case of collection of cold particles (ions) or hot species (electrons).

When $I = 0$ the probe is at the *floating potential* V_{fl} , i. e. the probe is at sufficiently negative voltage to compensate the electron current with accelerated ion current.

Data acquisition and analysis is performed by the software *SmartSoft*© supplied together with the Langmuir probe device.

The software uses an iterative algorithm, the *intersecting slope* routine, to determine the values of kT_e and n_e . The iterative algorithm, in *SmartSoft*©, is based on reference [161], taking into account the Laframboise theory of sheath expansion because of change in the probe bias [162]. The first step is to evaluate the plasma potential V_{pl} from inflection point of the V - I curve: $d^2I/dV^2 = 0$. Subsequently, this value is refined extending the current exponential part, which is below the first V_{pl} , to higher V_{probe} . Current values above the first V_{pl} will be extrapolated back until the point where the two lines intersect: the new V_{pl} .

The first approximation of the mean value of the electron temperature can be then calculated by:

$$kT_e = \frac{e \int_{V_{fl}}^{V_{pl}} I(V) dV}{I(V_{pl})} \quad (\text{E.1})$$

As shown Figure E.2, the electron current increases with pressure. At 0.3 Pa, the electron component increases with gas mass, but this effect is negligible at 3 Pa. The ion current is slightly affected by the working pressure in Xe plasma, but it is doubling in the case of Ar, increasing the pressure from 0.3 to 3 Pa.

The sputtering gas mass has only a minor effect on the floating and plasma potentials ($V_{fl} \approx -0.9$ V at 0.3 Pa and $V_{fl} \approx -6.0$ V at 3Pa; $V_{pl} \approx 1$ V). Otherwise, the increase of the working pressure is correlated with a significant decrease of V_{fl} , while V_{pl} remains almost unchanged. This could be explained by the enhancement of the electron current with the working pressure, the floating potential is therefore increasing in negative values to compensate the negative charge arriving.

The calculated average values of the electron temperature are reported in Table E-2:

<i>Deposition gas</i>	<i>Pressure (Pa)</i>	<i>kT_e (eV)</i>
Ar	0.3	0.39 ± 0.02
Xe	0.3	0.35 ± 0.06
Ar	3	0.60 ± 0.11
Xe	3	0.61 ± 0.07

Table E-2: Calculated values for kT_e as function of the deposition gas and pressure

No difference was detected in the mean electron temperature in relation with the gas mass, but kT_e is low and doubles when the working pressure increases.

Anyhow, from the Langmuir probe investigations, the deposition process is characterised by a weak plasma (plasma density $< 10^9 \text{cm}^{-3}$) and no strong differences between Xe and Ar discharges were observed, irrespective to the deposition pressure.

From current measurements performed with a flat electrode arrangement (figure E.3), it was possible to estimate the ion flux in Ar discharges at 0.3 and 3 Pa.

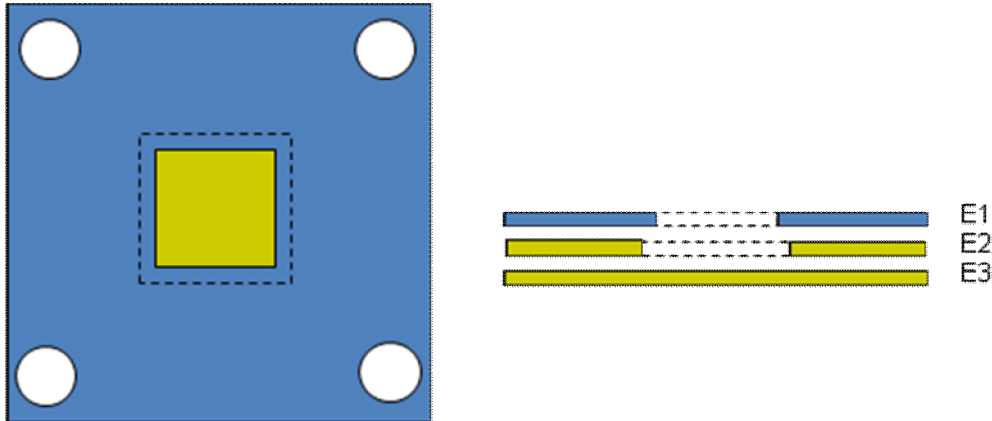


Figure E.3: Sketch of the flat electrode configuration: the current was collected at the plate $E3$ while $E1$ and $E2$ were connected to ground. The $E3$ electrode area is 0.64 cm^2

Considering the ions saturation current measured at -50 V , the ion flux is about $4.1 \times 10^{15} \text{ ion/cm}^2\text{s}$ and $3.5 \times 10^{15} \text{ ion/cm}^2\text{s}$ at 0.3 and 3 Pa, respectively.

This experiment was performed with slightly different magnetrons electrical input giving the deposition rate in $\text{atoms/cm}^2\text{s}$ reported in paragraph 5.1 ($4.20 \times 10^{14} \text{ at/cm}^2\text{s}$ at 0.3 Pa and $2.56 \times 10^{14} \text{ at/cm}^2\text{s}$ at 3 Pa). This will give an ion/atoms ratio equal to 10 at 0.3 Pa and 14 at 3 Pa.

Appendix F: Dependence of the disorder- order transformation on the layer thickness

Here it is briefly reported about the investigation of the Al to Ll_0 phase transformation as a function of the layer thickness. Layer stoichiometry, as film thickness, was calculated by RBS: $Fe : Pt = (52 \pm 2) : (48 \pm 2)$. In figure F.1 it is shown the GIXRD patterns collected *ex-situ* for three different layer thicknesses: 9, 19 and 27 nm.

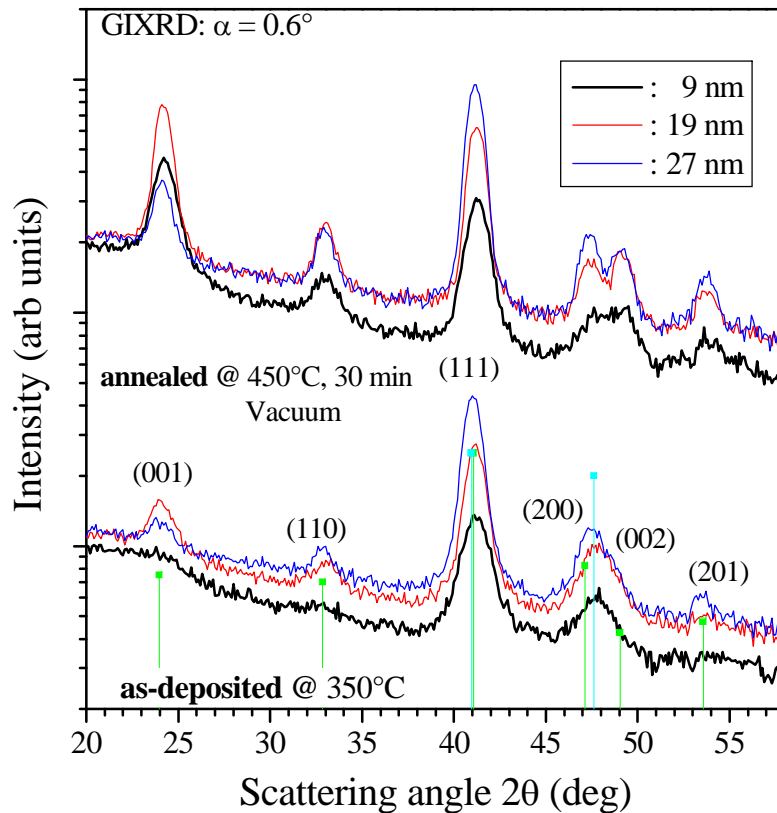


Figure F.1: GIXRD ($\alpha_i = 0.6^\circ$). Bottom curves: after co-deposition in Ar at 0.3 Pa at 350°C; top part: RT deposited layers after annealing in vacuum at 450°C for 30 min.

The Ll_0 phase appeared in the 9 nm layer only after annealing at 450°C. For the thicker layers, 19 and 27 nm, the deposition temperature is enough to initiate the phase transformation as it is possible to notice with the appearance of the superstructure peaks. But, a much higher degree of order in the layer is reached only after annealing at 450°C as confirmed by a clear splitting of the (200)/(002) reflections.

References

- 1 http://www.amps.net/newsletters/issue27/27_poulsen.htm
- 2 A. Moser, K. Takano, D. T. Margulies, M. Albrecht, Y. Sonobe, Y. Ikeda, S. Sun, E. E. Fullerton, *J. Phys. D: Appl. Phys* 35 (2002) R157
- 3 <http://www.hitachiGST.com>
- 4 A. J. Argumedo, D. Berman, R. G. Biskeborn, G. Cherubini, R. D. Cideciyan, E. Eleftheriou, W. Haeberle, D. J. Hellman, R. Hutchins, W. Imaino, J. Jelitto, K. Judd, P.-O. Jubert, M. A. Lantz, G.M.McClelland, T. Mittelholzer, C. Narayan, S. Oelcer, P. J. Seger, *IBM J. Res. & Dev.* 52 (4/5) (2008), 513
- 5 D. Weller, A. Moser, *IEEE Trans. Magn.* 35, 4423 (1999)
- 6 A. Moser, D. Weller, *IEEE Trans. Magn.* 35, 2808 (1999)
- 7 D. Weller, A. Moser, L. Folks, M. E. Best, Wen Lee, M. F. Toney, M. Schwickert, J. Thiele, M. F. Doerner, *IEEE Trans. Magn.* 36, 10 (2000)
- 8 H. N. Bertram, H. Zhou, R. Gustafson, *IEEE Trans. Magn.* 34, (1998) 1845
- 9 http://www.seagate.com/content/pdf/whitepaper/TP-549_PerpRecording_Feb-06.pdf
- 10 Yun-Chung Wu, Liang-Wei Wang, Chih-Huang Lai, *Appl. Phys. Lett.* 91 (2007) 072502
- 11 T. Konagai, Y. Kitahara, T. Itoh, T. Kato, S. Iwata, S. Tsunashima, *J. Magn. Magn. Mat.* 310, (2007) 2662
- 12 M. L. Yan, R. Skomski, A. Kashyap, L. Gao, S. H. Liou, D. J. Sellmyer, *IEEE Trans. Magn.* 40, (2004) 2495
- 13 Shouheng Sun, C. B. Murray, D. Weller, L. Folks, A. Moser, *Science* 287, (2000) 1989
- 14 R. W.Chantrell, D. Weller, T. J. Klemmer, S. Sun, *J. Appl. Phys.* 91, (2002) 6866
- 15 K. Barmak, J. Kim, S. Shell, E. B. Svedberg, J. K. Howard, *Appl. Phys. Lett.* 80 (2002) 4268
- 16 D. C. Berry, K. Barmak, *J. Appl. Phys.* 101, (2007) 014905
- 17 K. Barmak, J. Kim, D. C. Berry, K. W. Wierman, E. B. Svedberg, J. K. Howard, *J. Appl. Phys.* 95 11 (2004) 7486.
- 18 K. R. Coffey, M. A. Parker, and K. J. Howard, *IEEE Trans. Magn.* 31 (1995), 2737
- 19 R. A. Ristau, K. Barmak, L. H. Lewis, K. R. Coffey, and J. K. Howard, *J. Appl. Phys.* 86 (1999), 4527

- 20 J.-U. Thiele, L. Folks, M. F. Toney, D. K. Weller, *J. Appl. Phys.* 84 (1998) 5686-5692
- 21 B. E. Warren, *X-Ray Diffraction*, Dover Publications Inc. New York (1990)
- 22 JCPDS crystallographic tables 29-0718
- 23 S. S. A. Raze, J. B. Staunton, F. J. Pinski, *Phys. Rev. B* 56 (1996) 8082
- 24 JCPDS crystallographic tables 43-1359
- 25 I. Galanakis, M. Alouani, H. Dreysse', *Physica B* 320 (2002) 221-225
- 26 W. Grange, I. Galanakis, M. Alouani, M. Maret, *Phys. rev. B* 62 (2000) 1157-1166
- 27 T. B. Massalski, editor in chief, *Binary Phase Diagrams*, American Society for Metals, Metals Park, Ohio, (1990)
- 28 D. C. Berry, K. Barmak, *J. Appl. Phys.* 99, (2006) 08G901
- 29 B. Rennhofer, B. Sepiol, M. Sladecsek, D. Kmiec, S. Stankov, G. Vogl, M. Kozlowski, R. Kozubski, A. Vantomme, J. Meersschaut, R. Rüffer, A. Gupta, *Phys. Rev. B* 74, (2006), 104301-104309
- 30 K. W. Wierman, C.L. Platt, J. K. Howard, *J. Magn. and Magn. Mat.* 278 (2004), 214
- 31 C. H. Lai, C. H. Yang, C. C. Chiang, T. Balaji, T. K. Tseng, *Appl. Phys. Lett.* 85 (2004) 4430-4432
- 32 T. Maeda, T. Kai, A. Kikitsu, T. Nagase, J. Akiyama, *Appl. Phys. Lett.* 80 (2002) 2147-2149
- 33 K. W. Wierman, C. L. Platt, J. K. Howard, F. E. Spada, *J. Appl. Phys.* 93 (2003) 7160
- 34 D. Ravelosona, C. Chappert, V. Mathet, H. Bernas, *Appl. Phys. Lett.* 76 (2000), 236
- 35 H. Bernas, J.P. Attane, K.-H. Heinig, D. Halley, D. Ravesolana, A. Marty, P. Auric, C. Chappert, Y. Samson, *Phys. Rev. B* 91 (2003), 77203
- 36 C. H. Lai, C. H. Yang, and C. C. Chiang, *Appl. Phys. Lett.* 83, (2003) 4550
- 37 D. Ravelosona, C. Chappert, H. Bernas, D. halley, Y. Samson, A. Marty, *J. Appl. Phys.* 91 (2002) 8082-8084
- 38 D. Ravelosona, D. Devolder, C. Chappert, H. Bernas, Y. Chen, J. P. Jamet, J. Ferre', E. Cambril, V. Mathet, *Mat. Sci. Eng. C* 15 (2001) 53-58
- 39 D. Ravelosona, C. Chappert, V. Mathet, H. Bernas, *J. Appl. Phys.* 87 (2000), 5771-5773
- 40 T. Shima T. Moriguchi, S. Mitani, and K. Takanashi, *Appl. Phys. Lett.* 80 (2) (2002), 288
- 41 Y. Endo, K. Oikawa, T. Miyazaki, O. Kitakami, Y. Shimada, *J. Appl. Phys.* 94 (2003) 7222-7226

- 42 M. L. Yan, N. Powers, and D. J. Sellmyer, *J. Appl. Phys.* 93, (2003) 8292
- 43 H. Zeng, M. L. Yan, N. Powers, and D. J. Sellmyer, *Appl. Phys. Lett.* 80 (2002) 2350
- 44 S. Okamoto, N. Kikuchi, O. Kitami, T. Miyazaki, Y. Shimada, *Phys. Rev. B* 66 (2002) 024413-1/9
- 45 Yu-Nu Hsu, S. Jeong, D. E. Laughlin, D. N. Lambeth, *J. Appl. Phys.* 89 (2001) 7068-7070
- 46 Xiao-Hong Xu, Hai-Shun Wu, Fang Wang, Xiao-Li Li, *Thin Solid Films* 473 (2004), 222-226
- 47 Xiao-Hong Xu, Hai-Shun Wu, Fang Wang, Xiao-Li Li, *Appl. Surf. Sci.* 233 (2004), 1-4
- 48 Y. F. Ding, J. S. Chen, E. Liu, *Surf. Sci. Techn.* 198 (2005) 262-265
- 49 C. J. Sun, G. M. Chow, J. P. Wang, *Appl. Phys. Lett.* 82 (2003) 1902-1904
- 50 Y.F. Ding, J.S. Chen, E. Liu, C.J. Sun, G.M. Chow, *J. Appl. Phys.* 97 (2005) 10H303
- 51 J. P. Attane', Y. Samson, A. Marty, D. Halley, C. Beigne', *Appl. Phys. Lett.* 79 (2001) 794-796
- 52 J. S. Chen, B. C. Lim, J. P. Wang, *Appl. Phys. Lett.* 81 (2002) 1848-1850
- 53 Yingfan Xu, J. S. Chen, J. P. Wang, *Appl. Phys. Lett.* 80 (2002) 3325-3327
- 54 J.S. Chen, B.C. Lima, Y.F. Ding, G.M. Chow *J. Magn. Magn. Mat.* 303 (2006) 309-317
- 55 Z. L. Zhao, J. P. Wang, J. S. Chen, *Appl. Phys. Lett.* 81 (2002) 3612-3614
- 56 J. S. Chen, B. C. Lim, J. F. Hu, Y. K. Lim, B. Liu, G. M. Chow, *Appl. Phys. Lett* 90 (2007), 042508
- 57 D. Sellmyer, R. Skomski Ed., *Advanced Magnetic Nanostructures Chapter 8* by X. F. Xu, M. L. Yan, D. J. Sellmyer (2006) Springer US
- 58 H. Zeng, Shouheng Sun, R. L. Sandstrom, C. B. Murray, *J. Magn. Magn. Mat.* 266 (2003) 227-232
- 59 N. Jaouen, D. Babonneau, D. Carbone, F. Wilhelm, A. Rogalev, T. K. Johal, G. van der Laan, *Phys. Rev. B.* 76 (2007) 104421
- 60 X.-H. Xu, H.-S. Wu, X.-L. Li, F. Wang, J.-F. Duan, *Physica B* 348 (2004), 436.
- 61 D. H. Wei, F. T. Yuan, H. W. Chang, K. L. Liu, T. S. Chin, C. C. Yu, Y. D. Yao, *Nanotechnology* 18 (2007) 335603-335608
- 62 B. H. Li, C. Feng, X. Gai, J. Teng, G. H. Yu, X. Xing, Z. Y. Liu, *Appl. Phys. Lett.* 91 (2007) 152502-152502-3
- 63 A. Tomu, I. Panagiotopoulos, D. Gournis, B. Kooi, *J. Appl. Phys.* 102 (2007) 023910

-
- 64 G. Safran, T. Suzuki, K. Ouchi, P.B. Barna, G. Radnoczi, *Thin Solid Films* 496 (2006) 580-584
- 65 M. Watanabe, T. Masumoto, D. H. Ping, K. Hono, *Appl. Phys. Lett.* 76 (2000) 3971-3973
- 66 L. W. Wang, Y. C. Wu, C. H. Lai, *J. Appl. Phys.* 105 (2009) 07A713
- 67 L. W. Wang, Y. C. Wu, M. T. Rahman, C. H. Lai, *J. Appl. Phys.* 103 (2008) 07E126
- 68 L. W. Wang, Y. C. Wu, C. H. Lai, C. R. Chang, *J. Appl. Phys.* 103 (2008) 07E140
- 69 Y. C. Wu, L. W. Wang, C. H. Lai, *Appl. Phys. Lett.* 93 (2008) 242501
- 70 Z. Zhang, T. Suzuki, K. Kang, N. Omoto, *Nanotech* 2003, 3, 274
- 71 T. Yang, G.H.Yu, B.H.Li, T. Suzuki, F.W.Zhu, *Adv. Nanomaterials and Nanodevices 2002, (IUMRS-ICEM 2002, Xi'an, China)*
- 72 C. L. Platt, K. W. Wierman, E. B. Svedberg, R. van de Veerdonk, J. K. Howard. A. G. Roy, D. E. Laughlin, *J. Appl. Phys.* 92 (2002) 6104-6109
- 73 Z.L. Zhao, J.S. Chen, J. Ding, J.B. Yi, B.H. Liu, J.P. Wang, *Appl. Phys. Lett.* 88 (2006), 052503
- 74 Y.M. Chiang, D.P. Birnie III, W. D. Kingery, in *Physics Ceramics*, WILEY, New York (1997), 357
- 75 J. S. Kim, Y. M. Koo, B. J. Lee, *J. Appl. Phys.* 99 (2006), 053906
- 76 Y. Itoh, M. Takeuchi, A. Tsukamoto, K. Nakagawa, A. Itoh, T. Katayama, *Jpn. J. Appl. Phys.* 41 (2002), L 1066
- 77 Y. Itoh, T. Aoyagi, A. Tsukamoto, K. Nakagawa, A. Itoh, T. Katayama, *Jpn. J. Appl. Phys.* 43 (2004), 8040
- 78 F. F. Chen, *Introduction to Plasma Physics and Controlled Fusion: Plasma physics*, Edition: 2, Springer, 1984
- 79 M. A. Lieberman, A. J. Lichtenberg, *Principles of plasma discharges and materials processing*, Second Edition, John Wiley & Sons 2005 NY USA
- 80 W. Möller, *Fundamentals of Plasma Physics, Resume of a lecture held at the University of Technology Dresden*, Summer 2006
- 81 <http://webbook.nist.gov/chemistry/>
- 82 I. Petrov, I. Ivanov, V. Orlinov, J.-E. Sundgren, *J. Vac. Sci. Technol. A* 11 (5), (1993) 2733
- 83 J. H. Keller, R. G. Simmons, *IBM J. Res. Dev.* 23-1 (1979) 24-32
- 84 Y. P. Raizer, *Gas Discharge Physics*, Springer, New York (1991)
- 85 <http://www.angstromsciences.com/technology/sputtering-technology>
- 86 B. Liedke, FWI – FZD private communication (2009)

- 87 W. Möller, *Fundamentals of Ion-Surface Interactions: Short resume of a lecture held at the Technical University of Dresden, 2004*
- 88 P. Sigmund, Phys. Rev. B 184 (1969) 383
- 89 Y. Yamamura, N. Matsunami, N. Itoh, Rad. Effects 71 (1983), 65
- 90 R. Behrisch, W. Eckstein, *Sputtering by Particle Bombardment*, Springer-Verlag (2007)
- 91 W. Eckstein, *Computer simulation of Ion-Solid Interactions*, Springer-Verlag (1991)
- 92 M. W. Thompson, Philosophical Magazine 18, (1968) 377
- 93 W. Eckstein, Nucl. Instr. Methods B 18 (1987) 344-348
- 94 G. Falcone, Phys. Rev. Lett. 38 (10), (1998) 6398-6401
- 95 M. Stepanova, S. K. Dew, J. Vac. Sci. Technol. A 19, (1990) 2805-2816
- 96 T. P. Drüsedau, T. Bock, T-M. John, F. Klabunde, W. Eckstein, J. Vac. Sci. Technol. 17(5), (1999) 2896-2905
- 97 W. Möller, W. Eckstein, Nucl. Instrum. Meth. B (2) (1984) 814
- 98 W. Möller, W. Eckstein, Nucl. Instrum. Methods Phys. Res. Sect. B 230 (1-3) (1984) 814-818, 37
- 99 J. A. Thornton, Thin Solid Film 54 (1978) 23-31
- 100 S. Dew, T. Smy, M. Brett, Jpn. J. Appl. Phys. 33, (1994) 1140-1145
- 101 R. S. Robinson, J. Vac. Sci. Technol. 16(2), (1979) 185-188
- 102 W. D. Westwood, J. Vac. Sci. & Technol. 15, (1978) 1-9
- 103 S. D. Ekpe, S. K. Dew, J. Vac. Sci. Technol. A 21, (2003) 476-483
- 104 R. E. Somekh, J. Vac. Sci. Technol. A 2, (1984) 1285-1291
- 105 T. P. Drüsedau, F. Klabunde, P. Veit, TH. Hempel, Phys. Status Solidi A 161, (1996) 167-184
- 106 B. A. Movchan, A. V. Demchishin, Phys. Metal. Metallogr. 28, (1969) 83-90
- 107 J. A. Thornton, J. Vac. Sci. & Technol. 11 (4), (1974) 666-670
- 108 J. A. Thornton, J. Vac. Sci. & Technol. A 4 (6), (1986) 3059-3065
- 109 J. A. Thornton, D. W. Hoffman, Thin Sol. Films, 171, (1989) 5-31
- 110 R. Messier R. A. Giri, R. A. Roy, J. Vac. Sci. & Technol. A 2 (1984) 500-503
- 111 R. Messier, J. E. Yehoda, J. Appl. Phys. 58 (10), (1985) 3739-3746
- 112 R. Messier, J. Nanophot. 2, 021995 (2008) 1-21
- 113 K. Barmak, J. Kim, S. Shell, E. B. Svedberg, J. K. Howard, Appl. Phys. Lett. 80 (2002), 4268

-
- 114 AJA International, North Scituate, MA 02060, <http://ajaint.com>
- 115 <http://www.fzd.de/ROBL>
- 116 N. Schell, J. von Borany, J. Hauser, AIP conference proceedings 879 (2007) 1813-1816
- 117 tectra GmbH, Frankfurt/M, <http://www.tectra.de>
- 118 J. Als-Nielsen, D. Mc Morrow, *Elements of Modern X-ray Physics*, John Wiley & Sons Ltd, England (2001)
- 119 A. Vailionis, *X-ray diffraction – Lecture Note*, Stanford University (2006)
- 120 J. Grenzer, *private communication*
- 121 U. Pietsch, V. Holy, T. Baumbach, *High-Resolution X-Ray Scattering, From Thin Film to Lateral Structures*, Second Edition, Springer-Verlag, USA (2004)
- 122 P. Zaumseil, Rocking Curve & Reflectivity Curve Simulation & Fitting, RC_REF_Sim_Win, Version 1.09 (2009)
- 123 L. Névot, P. Croce, Phys. Rev. Appl. 15 (1980), 761
- 124 M Schmidbauer, *X-Ray Diffuse Scattering from Self-Organized Mesoscopic Semiconductor Structures*, Springer-Verlag, Germany (2004)
- 125 H. Dosch, *Critical Phenomena at Surface and Interfaces – Evanescent X-Ray and Neutron Scattering*, Springer-Verlag, Germany (1992)
- 126 P. Scherrer, *Göttinger Nachrichten Gesell.* 2 (1918), 98
- 127 B. P. Cullity, S. R. Stock, *Elements of X-Ray Diffraction*, 3rd Ed., Prentice Hall, NJ USA (2001)
- 128 *Peakfit*™ Version 4, Jandel Scientific, 1991-1995
- 129 W. Voigt, Sitzungsber. Math. Naturwiss. Kl. Bayer. Akad. Wiss. München (1912)
- 130 G. Renaud, R. Lazzari, C. Revenant, A. Barbier, M. Noblet, O. Ulrich, F. Leroy, J. Jupille, Y. Borensztein, C.R. Henry, J.P. Deville, F. Scheurer, J. Mane-Mane, O. Fruchart, Science 2003, 300, 1416
- 131 A. Naudon D. Thiaudiere, *J. Appl. Cryst.* 30 (1997), 822-827
- 132 C. Revenant, F. Leroy, R. Lazzari, G. Renaud, and C. R. Henry Phys. Rev.B 69 (2004), 035411
- 133 G. Swislow, *SPEC X-ray diffraction software* (Certified scientific software), USA, <http://www.certif.com/spec.html>
- 134 M. Schuster, H. Goebel, J. Phys. D: Appl. Phys. 28 (1995), A270
- 135 <http://www.bruker-axs.de/uploads/media/S88-E00006.pdf>
- 136 W. Matz, N. Schell, G. Bernhard, F. Prokert, T. Reich, J. Claußner, W. Oehme, R. Schlenk, S. Dienel, H. Funke, F. Eichhorn, M. Betzl, D. Pröhl, U. Strauch, G. Hüttig,

- H. Krug, W. Neumann, V. Brendler, P. Reichel, M.A. Denecke, H. Nitsche, J. Synchrotron Radiat. 6 (1999) 1076-1085
- 137 N. Schell, W. Matz, F. Eichhorn, F. Berberich, J. Alloys Compd. 328 (2001) 105-111
- 138 HUBER X-ray Diffraction Equipment, Germany, <http://www.xhuber.com>
- 139 J. R. Tesmer, M. Nastasi, *Handbook of modern ion beam material analysis*. Pittsburgh, Pennsylvania : Materials Research Society (1995)
- 140 M. Döbeli, *Materials analysis*, Paul Scherrer Institute and ETH-Zurich, Switzerland
- 141 W. Möller, *Schnelle Ionen für die Oberflächen-Analyse Schnelle Ionen für die Oberflächen-Analyse*
- 142 M. O. Thompson, RUMP, <http://www.genplot.com/>
- 143 SEM S-4800, *User Manual*, Hitachi
- 144 J. Clarke, I. Braginski, *The SQUID Handbook, Vol. I, Fundamentals and Technology of SQUIDs and SQUID Systems*, Wiley-VCH Verlag GmbH (2004)
- 145 Quantum Design, Application note 1014-824, Rev. A-0 (2003)
- 146 D. J. Livingstone, J. Appl. Phys. 52 (1981), 2544
- 147 N. H. Luong, V. V. Hiep, D. M. Hong, N. Chau, N. D. Linh, M. Kurisu, D. T. K. Anh, G. Nakamoto, J. Magn. and Magn. Mat. 290–291 (2005) 559.
- 148 J. Ziegler, J. Biersack, SRIM version 2008.03, www.srim.org (2008)
- 149 G. Chiari, *Affina code*, Universita' di Torino (Italy), (1994)
- 150 B. Lewis J. C. Anderson, *Nucleation and Growth of Thin Films*, Academic Press London (1987)
- 151 T. Oates, A. Muecklich, Nanotechnology 16 (2005), 2606
- 152 X. Liu, A. Morisako, J. Magn. Magn. Mater. 310 (2007) e916
- 153 W. Eckstein, J. P. Biersack, Z. Phys. B 63 (1986) 471
- 154 M. P. Seah, Nucl. Instr. Methods B 229, (2005) 348
- 155 A. Guinier, *X-Ray Diffraction in Crystals, Perfect Crystals and Amorphous Bodies*, W. H. Freeman and Company (1963) USA
- 156 I. Langmuir, Phys. Review, 26 (1925) 585
- 157 I. Langmuir, Proc. of the National Academy of Sciences of the United States of America, Volume 14, Issue 8, pp. 627-637
- 158 SmartProbe User Manual, Scientific Systems Ltd., Ireland
- 159 A. Palmero E. D. van Hattum, W. M. Arnoldbik, A. M. Vredenberg, F. H. P. M. Habraken, J. Appl. Phys. 95 (2004) 7611-7618

- 160 B. Fritsche T. Chevolleau, J. Kourtev, A. Kolitsch, W. Möller *Vacuum* 69 (2003) 139-145
- 161 M.B. Hopkins, W.G. Graham, *Rev. Sci. Instrum.* 57 (9) (1986), 2210
- 162 R.M. Clements, *J. Vac. Sci. Technol.* 15 (2) (1978), 193

Acknowledgement

Too many are the persons that I would like to thank to include them in one page.

Firstly, I would like to thank Prof. Wolfhard Möller, for his suggestions regarding some difficult steps in finding agreement between plasma measurements and theory and for his critical reading of this thesis.

I would like to thank my supervisor, Dr. Johannes von Borany, for his constant support, and his precious precise advises during the all work.

A particular thank goes to Dr. Jörg Grenzer who is making all the X-ray sources working and therefore X-ray scattering experiments are possible.

I would like to thank Prof. Jürgen Fassbender for the patience in explain how magnetism should work.

I am grateful to Dr. Anatoli Rogozin for his continuous advices about how to use magnetron sputtering and how it is working.

A special thank goes to Mrs. Andrea Scholz for always finding a way to give some measurement time and for creating such a friendly atmosphere that is difficult not to miss.

I also would like to thank the ROBL team: Dr. Nicole Jeutter, The Local Contact, Dr. Carsten Baetz and Mr. Marco Hesse who was making the deposition chamber working.

Moreover I really grateful to Mr. Sylvio Probst, for the RTA and to Mrs Elfi Christalle for the SEM investigations.

My thank goes also to Dr. Rainer Groetzschel and to the whole staff at the RBS equipment.

And how to forget Mr. Rene' Weidauer able to solve the technical problems of the sputtering chamber; of course to Mr. Udo Strauch who was making the annealing experiments possible at ROBL and Mr. Jens Zscharschuch and Mr. Ingolf Winkler for the Xe.

Thanks to Mr. Georg Talut and Mr. Manuel Zschintzsch for making this friendly atmosphere in the office.

At the end of course my family, that always unconditionally supports me.

List of publications

- 1. The effect of the sputtering gas (Ar, Xe) on FePt clusters formation. Structural and magnetic properties**
V. Cantelli, J. Grenzer, J. von Borany, J. Fassbender
Journal of Applied Physics 105, 07B529 (2009)
- 2. In-situ grazing incidence scattering investigations during magnetron sputtering deposition of FePt/Ag thin films**
V. Cantelli, J. von Borany, N. Jeutter, J. Grenzer
Advanced Engineering Materials 11-6, 478 (2009)
- 3. Influence of energetic ions and neutral atoms on the L1₀ ordering of FePt films**
V. Cantelli, J. von Borany, A. Mücklich, Shengqiang Zhou, J. Grenzer
Nuclear Instruments and Methods in Physics Research B 257, 1-2, 406 (2007)
- 4. Influence of He-ion-irradiation on thin NiMn/NiFe exchange bias films**
V. Cantelli, J. von Borany, J. Grenzer, R. Kaltofen, J. Schumann, J. Fassbender
Journal of Applied Physics 99, 08C102 (2006)
- 5. Phase formation within Au and Ge nanoislands by room temperature ion irradiation**
T. Som, B. Satpati, F. Prokert, V. Cantelli, D. Kabiraj
Nanotechnology 17, 5248 (2006)
- 6. Investigation of the formation and phase transition of Ge and Co nanoparticles in a SiO₂ matrix**
V. Cantelli, J. von Borany, A. Mücklich, N. Schell.
Nuclear Instruments and Methods in Physics Research B 238, 268 (2005)
- 7. Real-time evolution of the ITO film properties and structure during annealing in vacuum**
A. Rogozin, N. Shevchenko, M. Vinnichenko, F. Prokert, V. Cantelli, A. Kolitsch, W. Möller
ESRF Highlights 2004, 28
- 8. Real-time evolution of the ITO film properties and structure during annealing in vacuum**
A. Rogozin, N. Shevchenko, M. Vinnichenko, F. Prokert, V. Cantelli, A. Kolitsch, W. Möller
Applied Physics Letters 85, 212 (2004)
- 9. XPS study of ceramic three-way catalysts**
C. Battistoni, V. Cantelli, M. Debenedetti, S. Kaciulis, G. Mattogno, A Napoli
Applied Surface Science 144-145, 390 (1999)
- 10. Metal Organic Deposition of YBCO and BSCCO platelets, films and wires**
C. Manfredotti, F. Fizzotti, E. Vittone, P. Polesello, N. Rizzi, V. Cantelli, P. Bruno, P. Volpe, M. Castiglione, P. Benzi, P. Pallavidino, G. Chiari and A. Borghi
Il Nuovo Cimento 6D, 1729 (1994)

Conference contributions

V. Cantelli, J. Grenzer, J. von Borany, J. Fassbender

Oral contribution: *Tailoring the FePt orientation on amorphous substrates by magnetron sputtering. Structural and magnetic investigations*

DPG Spring Meeting, 22-27.3.2009, Dresden, Germany

V. Cantelli, J. Grenzer, J. von Borany, J. Fassbender

Poster: *The effect of the sputtering gas (Ar, Xe) on FePt clusters formation. Structural and magnetic properties*

DPG Spring Meeting, 22-27.3.2009, Dresden, Germany

V. Cantelli, J. Grenzer, J. von Borany, J. Fassbender

Oral contribution: *The effect of the sputtering gas (Ar, Xe) on FePt clusters formation. Structural and magnetic properties*

53th Conference on Magnetism and Magnetic Materials, 10.-14.11.2008, Austin Texas, USA

V. Cantelli, J. Grenzer, J. von Borany, J. Fassbender

Oral contribution: *Tailoring the FePt orientation on amorphous substrates by magnetron sputtering, structural and magnetic investigations*

53th Conference on Magnetism and Magnetic Materials, 10.-14.11.2008, Austin Texas, USA

V. Cantelli, J. von Borany, J. Grenzer

Oral contribution: *Self-assembly FePt nanoislands: surface studies and magnetic properties*

7th Autumn School on X-ray scattering from surfaces and thin layers, 04.-06.10.2007, Smolenice, Slovakia

V. Cantelli, J. von Borany, J. Grenzer

Poster: *Fabrication of self-assembled $L1_0$ ordered FePt nanoislands by conventional DC magnetron sputtering*

International Conference on Nanoscale Magnetism - ICNM-2007, 25.-29.06.2007, Istanbul, Turkey

V. Cantelli, J. Grenzer, J. von Borany

Oral contribution: *Dual-magnetron sputtering deposition of ferromagnetic FePt layers: in-situ x-ray investigations*

Neue Entwicklungen in Röntgendiffraktometrie und -topographie, 24.04.2007, Frankfurt (Oder), Germany

V. Cantelli, J. von Borany, J. Fassbender, J. Grenzer

Poster: *Influence of energetic ions and neutral atoms on the $L1_0$ ordering of FePt films*

IBMM 2006, 15th Int. Conf. on Ion Beam Modification of Materials, 18.-22.09.2006, Taormina, Italy

V. Cantelli, J. von Borany, J. Grenzer, J. Fassbender

Oral contribution: *Influence of energetic ions on the $L1_0$ ordering of FePt films fabricated by magnetron sputtering*

DPG - spring meeting of the Division Condensed Matter, EPS - 21st General Conference of the Condensed Matter Division, 26.-31.03.2006, Dresden, Germany

V. Cantelli, J. von Borany, Beckers, M., J. Fassbender

Oral contribution: *L1₀ ordering of magnetron sputtered FePt films at temperatures below 400°C*
Magnetism and Magnetic Materials Conference, 30.10.-03.11.2005, San Jose, USA

V. Cantelli, J. von Borany, J. Grenzer, Kaltofen, R., Schumann, J., J. Fassbender
Poster: *Influence of He-ion-irradiation on thin NiMn/NiFe exchange bias films*
Magnetism and Magnetic Materials Conference, 30.10.-03.11.2005, San Jose, USA

V. Cantelli, J. von Borany, J. Grenzer
Oral contribution: *X-ray investigations on NiMn films after ion beam irradiation*
6th Autumn School on X-ray Scattering from Surfaces and Thin Layers, 18.-21.09.2005, Smolenice, Slovakia

V. Cantelli, J. von Borany, A. Mücklich, N. Schell
Poster: *Investigation of the Formation and Phase Transition of Ge and Co Nanoparticles in a SiO₂ matrix*
4th Int. Conference on Synchrotron Radiation in Materials Science (SRMS-4), August 23-25, 2004, Grenoble, France

V. Cantelli, N. Shevchenko, A. Rogozin, N. Schell, M. Vinnichenko, F. Prokert, A. Kolitsch
Poster: *In-situ investigations of the amorphous-to-crystalline transformation of ITO films by synchrotron X-ray scattering*
4th Int. Conference on Synchrotron Radiation in Materials Science (SRMS-4), August 23-25, 2004, Grenoble (France)

V. Cantelli, A. Rogozin, N. Shevchenko, M. Vinnichenko, F. Prokert, A. Kolitsch, W. Möller
Poster: *Annealing of ITO films: in situ studies of structure and resistance*
ESRF Science Days Seminar, May 26-28 2004, Aussois (France)

G. Berti, S. Citi, G. Baldi, V. Cantelli, F. De Paolis, C. Giampaolo, F. Guelfi, S. Justi, G.F. Pardina
Poster: *Results on monitoring the calibration of diffractometers using diffraction instrumental monitoring (DIM) with data of corundum from different instruments*
7th European Powder Diffraction Conference, May 20-23 2000, Barcelona (Spain)

V. Cantelli
Invited talk: *The industrial use of X-ray diffraction to optimise shot peening process for automotive gears*
Italian-French Workshop on Neutron Applications in Materials Science and Technology, January 21-22 1999 - Laboratoire Léon Brillouin (CEA-CNRS), Saclay (France)

Erklärung

Hiermit versichere ich, dass ich die vorliegende Arbeit selbstständig verfasst und keine anderen als die angegebenen Quellen und Hilfsmittel benutzt habe, dass alle Stellen der Arbeit, die wörtlich oder sinngemäß aus anderen Quellen übernommen wurden, als solche kenntlich gemacht sind und dass die Arbeit in gleicher oder ähnlicher Form noch keiner Prüfungsbehörde vorgelegt wurde.

Unterschrift

Dresden, den 22. Januar 2010